35th Anniversary
The Geological Society of Hong Kong

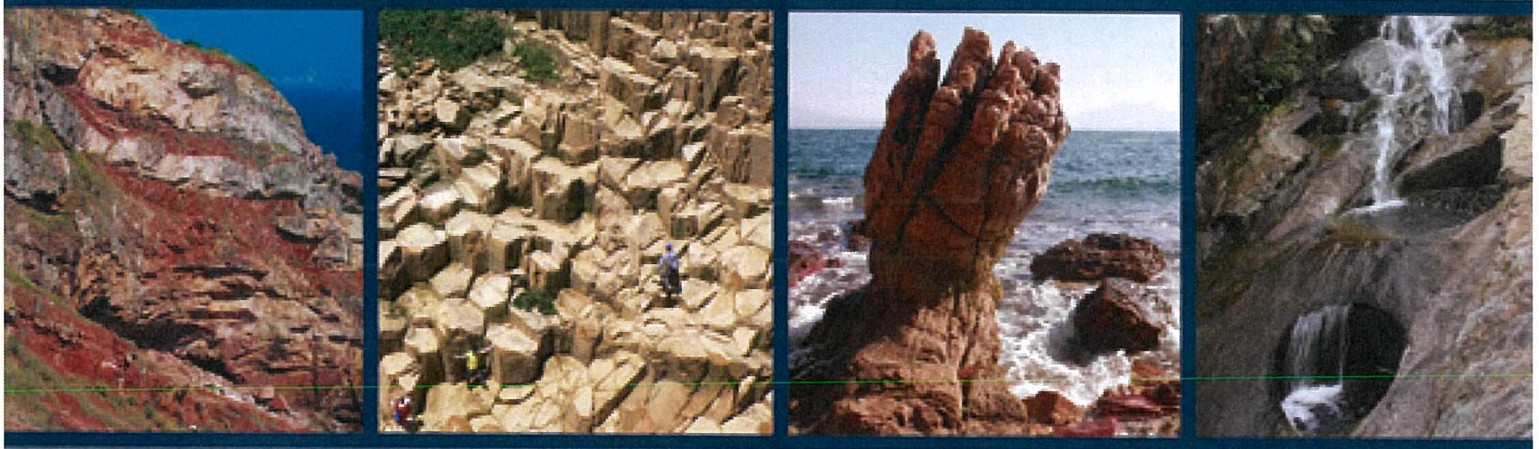

香港地質學會
35週年紀念

Conference on Recent Geological Research and Development

Bulletin No. 12, Issue No. 2, 2017

Since 1982

The Geological Society of Hong Kong
35th Anniversary
Conference, Dinner and Field Trips

Recent Geological Research and Development

17 & 18 November 2017

The City View,
23 Waterloo Road, Yau Ma Tei, Kowloon, Hong Kong

Organised by
The Geological Society of Hong Kong
(Since 1982)

Organising Committee

Chairman:
Mr. Paul Cheung

Members:
Dr. Margie Chen
Mr. K F Leung
Mr. Raymond S M Chan
Dr. Susan Xuran Zuo
Mr. W K Leung
Mr. Patrick Ho
Ms. Peggy Lam
Dr. Jean Wong
Mr. T C Lung
Mr. Johnson Li
Ms. Tracy Leung

Published by
The Geological Society of Hong Kong
(Since 1982)

Bulletin No. 12, Issue No. 2, 2017

Table of Contents

Foreword

Not long ago has the celebration for the 30th Anniversary been just finished, the Geological Society of Hong Kong has swiftly turned into its 35th Anniversary this year.

In the past few years, we have seen quite a number of advancements that the community of the earth sciences has made in Hong Kong. The Earth System Science Programme, Faculty of Science, CUHK, has been officially established in 2012, addressing the need of the study of the dynamics of earth. Some of the graduates of the Department of Earth Sciences, HKU, which is the very first department of geological sciences in the city, has recently taken up a few teaching positions in the new department of the CUHK. This truly demonstrates one of the core values of sciences in our community that knowledge needs to be passed down to the next generation for a continuous growth.

On the other hand, the sectors of geotechnical engineering and engineering geology together with civil engineering have successfully delivered a number of infrastructure projects in the territory recently. This also marked an advancement of the geology-related disciplines in our community.

The theme of this year Conference is "Recent Geological Research and Development", offering a board range of discussions of the latest advance in, for instance, geology of Hong Kong, groundwater studies, numerical approach to natural terrain hazard and its mitigation, studies of active faults by experts coming from different parts of the Greater-China region. I hope that this conference can give you an update of development of various fields of geological sciences in the region.

I very much appreciate the President of Chinese Taipei Geology Society, President of the Taiwan Association of Professional Applied Geologists, President of the Taipei Association of Professional Applied Geologists and President of the Taichung Association of Professional Applied Geologists for their greetings to our 35th Anniversary. I also extend my sincere gratitude to all authors and speakers for their valuable contribution to this conference.

I, on behalf of the Society, wish to express our warmest gratitude to all sponsors for their generosity and support to this special 35th Anniversary conference. Last but not least, I must thank the Organising Committee for their great work in making this conference and other Anniversary activities possible.

Mr. Kar Fai Leung
President
The Geological Society of Hong Kong

中華民國地質學會
10699 台北郵政 23-136 號信箱
The Geological Society located in Taipei

尊敬的梁會長，以及香港地質學會的朋友們：

欣聞香港地質學會將於 2017 年 11 月 17 日舉辦成立 35 週年大會。謹此，中華民國地質學會全體理監事，向本次大會的召開表示熱烈的祝賀！

走過 35 年，香港地質學會已為香港的地質研究以及應用做出了極大的貢獻。未來期待港台兩地的地質工作者能有更多的交流與合作，為兩地的地質學相關研究，再創造輝煌成就。

預祝大會圓滿成功！並祝所有與會嘉賓，身體健康、事業興旺！

中華民國地質學會

理事長　張中白

秘書長　林立虹　暨 全體理監事 恭賀

2017 年 08 月 31 日

慶祝香港地質學會成立35周年 賀函

致 香港地質學會暨全體會員

欣聞 貴學會成立35周年並舉辦慶祝大會，同身為地質科學專業人士的我們，同感喜悅，也備感光榮!

地質科學基礎教育的推動，與國際交流的經驗學習，都是看似平凡，卻是辛苦艱巨的工作。素聞 貴學會為推動香港的地質科學，並為專業人士和地質業餘愛好者提供一個交流平台，而於1982年成立。歷經35載，除舉辦地質會議和研討會，及定期組織本地及海外考察外，亦於近年推動地質科學基礎教育，並積極服務專業地質師與地質從業人員，與推動國際交流活動。讓同為推動地質科學基礎教育的推動，與國際交流的經驗學習，並身為 貴學會交流合作對象的我們，感到相當的敬佩與驕傲，也希望貴 學會與我會的交流合作，在此基石下，邁向更新的里程碑。

在此，本人謹代表台灣省應用地質技師公會、台北市應用地質技師公會、台中市應用地質技師公會等全體會員，敬祝大會成功，並祝 貴學會會務欣欣向榮。

臺灣省應用地質技師公會 理事長 顏一勤

台北市應用地質技師公會 理事長

台中市應用地質技師公會 理事長

Conference Programme on 17 November 2017 (Friday)

Venue: Crystal Ball Room, 2/F, The City View

No.	Time	Programme
	8:45 am	Registration
	9:00 am	Opening ceremony and welcome speech
	9:15 am	Start of Morning Session (Chaired by Prof. LS Chan)
1	9:25 am	An overview of recent research by the Hong Kong Geological Survey *Dr. Denise L K Tang*
2	9:50 am	Brittle characteristics of hard rocks under thermo-mechanical coupling and temperature effect of rockburst *Prof. Tianbin Li*
3	10:15 am	Earth Science in CUHK: Curriculum development and research in the first five years *Prof. Teng-fong Wong*
	10:40 am	Coffee Break
4	11:00 am	Investigation of a large, structurally controlled landslide in Sai Kung East Country Park *Mr. Steven J Williamson*
5	11:25 am	New evidence of activity in south segment of Chishan fault, Southern Taiwan *Mr. I Chin Yen*
6	11:50 am	Seismic precursor to instability induced by internal erosion in loose granular slopes *Prof. Wei Hu*
	12:15 pm	Lunch
	1:50 pm	Start of Afternoon Session (Chaired by Prof. TF Wong)
7	2:00 pm	Phreatic breccias in Hong Kong: field observations and inferences *Prof. L S Chan*
8	2:25 pm	The characteristics of paleovolcanoes of pyroclastic andesite of the Tuen Mun Formation in Hong Kong and the associated misunderstanding *Mr. K W Lai*
9	2:50 pm	Classifying failure modes of Hong Kong rocks under uniaxial compression loading using high speed imaging technique *Dr. Louis NY Wong*
	3:15 pm	Coffee Break
10	3:35 pm	Loess and its nature favoring geohazards *Prof. Yanrong Li*
11	4:00 pm	Submarine groundwater discharge and nutrient loadings in Tolo Harbor, Hong Kong using multiple geotracer-based models, and their implications of red tide outbreaks *Prof. Jimmy Jiao*
12	4:25 pm	New development in Statistical Landslide Hazard Analysis *Prof. C T Lee*
	5:00 pm	End of conference

AN OVERVIEW OF RECENT RESEARCH BY THE HONG KONG GEOLOGICAL SURVEY

Denise L K Tang, Roderick J Sewell, Kevin W F So, Y M Sin and S C Mok
Hong Kong Geological Survey, Geotechnical Engineering Office,
Civil Engineering and Development Department, HKSAR Government

Abstract: Over the past few years, the Hong Kong Geological Survey (HKGS) has applied some state-of-the-art research techniques to resolving a number of geological unknowns in Hong Kong. One of the more significant developments was the discovery of High Island supervolcano, which was followed by further research on the late Mesozoic large silicic magmatic systems using crystal-specific analysis. In addition, understanding of sediment provenance has been enhanced through detrital zircon U-Pb dating studies, leading to an improved interpretation of local stratigraphy, particularly in the northwest New Territories. These detrital zircon studies have also helped to characterize the crustal basement terranes which underpin Hong Kong. Improved temporal constraints on the post-magmatic crustal exhumation history of Hong Kong have been obtained from low-temperature fission-track thermochronology studies. The HKGS has continued to employ radiocarbon, optically stimulated luminescence (OSL) and cosmogenic isotope dating techniques for determining the ages of large landslide debris fans with a view to investigating possible links with neotectonic activities and palaeo-climate changes affecting Hong Kong. In conclusion, the HKGS has drawn on advanced research techniques to better understand Hong Kong's geological history, which is essential for continuous improvement of our geological maps.

INTRODUCTION

The Hong Kong Geological Survey (HKGS) is a section within the Geotechnical Engineering Office, Civil Engineering and Development Department (GEO/CEDD) of the Hong Kong SAR Government. The HKGS was established in 1982 (i.e. the same founding year as the Geological Society of Hong Kong) to undertake a detailed geological survey of Hong Kong to facilitate land use planning and infrastructural development. By the end of 1996, fifteen 1:20,000-scale solid and superficial geological maps and six memoirs (Addison, 1986; Strange and Shaw, 1986; Langford et al., 1989; 1995; Strange et al., 1990; Lai et al., 1996), covering the onshore and offshore areas of the entire territory, were published. In addition, twenty-four 1:5,000-scale geological

maps were produced during the 1990's covering strategic development areas in Yuen Long, Chek Lap Kok, Northern Lantau Island, Ma Wan, Tsing Yi, Ma On Shan and Tung Chung (Frost, 1992; Langford, 1994; Sewell and Fyfe, 1995; Sewell and James, 1995; Sewell, 1996; Sewell and Kirk, 2002). These larger scale maps were aimed at providing detailed geological information for the development areas, especially those underlain by marble and related complex ground conditions.

The geological data from both 1:20,000-scale and 1:5,000-scale mapping exercises, combined with the geochemical, geochronological and geophysical data available at that time, were synthesized and updated in two volumes (Fyfe et al., 2000; Sewell et al., 2000) with an accompanying set of 1:100,000-scale geological thematic maps. In 2003, the HKGS began updating the 1:20,000-scale geological maps in digital format, accompanying a comprehensive set of databases containing drillhole records, geochemical data, geophysical data (seismic profiles), fossil and mineral occurrences, etc. (Sewell et al., 2005). So far, three digital geological maps (Map Sheet Nos. 7, 11 and 15) have been published while updating of Map.

Apart from producing geological maps and reports, the HKGS has continued to undertake various geological studies on local magmatic rocks (Sewell et al., 2012b; Tang et al., 2017), stratigraphy (Sewell et al., 2016; 2017; So and Sewell, 2017), tectonic history (Tang et al., 2014), as well as landslides and hazard-related investigations (Sewell and Tang, 2012; Sewell et al., 2015). These studies have applied some state-of-the-art geosciences techniques to resolving some outstanding geological problems leading to improved understanding of Hong Kong's geological history and more accurate geological maps. This paper presents the findings and implications of some key studies completed by the HKGS over the past few years.

HIGH ISLAND SUPERVOLCANO AND ITS MAGMATIC SYSTEM

The discovery of the ancient High Island supervolcano (Sewell et al., 2012a) was the result of meticulous geological surveying work involving detailed mapping, geochemical and geochronological analyses, and geophysical surveys carried out by the HKGS over many years (Sewell et al., 1992; Campbell and Sewell, 1997; Darbyshire and Sewell, 1997; Davis et al., 1997; Fletcher et al., 1997; Sewell and Campbell, 1997; Campbell et al., 2007; Sewell et al., 2012b). The spectacular, columnar-jointed High Island Tuff (140.9±0.2 Ma; Davis et al., 1997), exposed in a large area of eastern Sai Kung, represents the intracaldera ignimbrite produced by a single, cataclysmic, caldera-forming

eruption. The volume of volcanic ash produced was estimated to be 1,300 km^3 (dense rock equivalent of 570 km^3) with the diameter of the ancient caldera estimated to be about 18 km (Sewell et al., 2012b). The coeval granites found in Kowloon and Hong Kong Island were considered to correspond to the roots of the volcanic system (Figure 1).

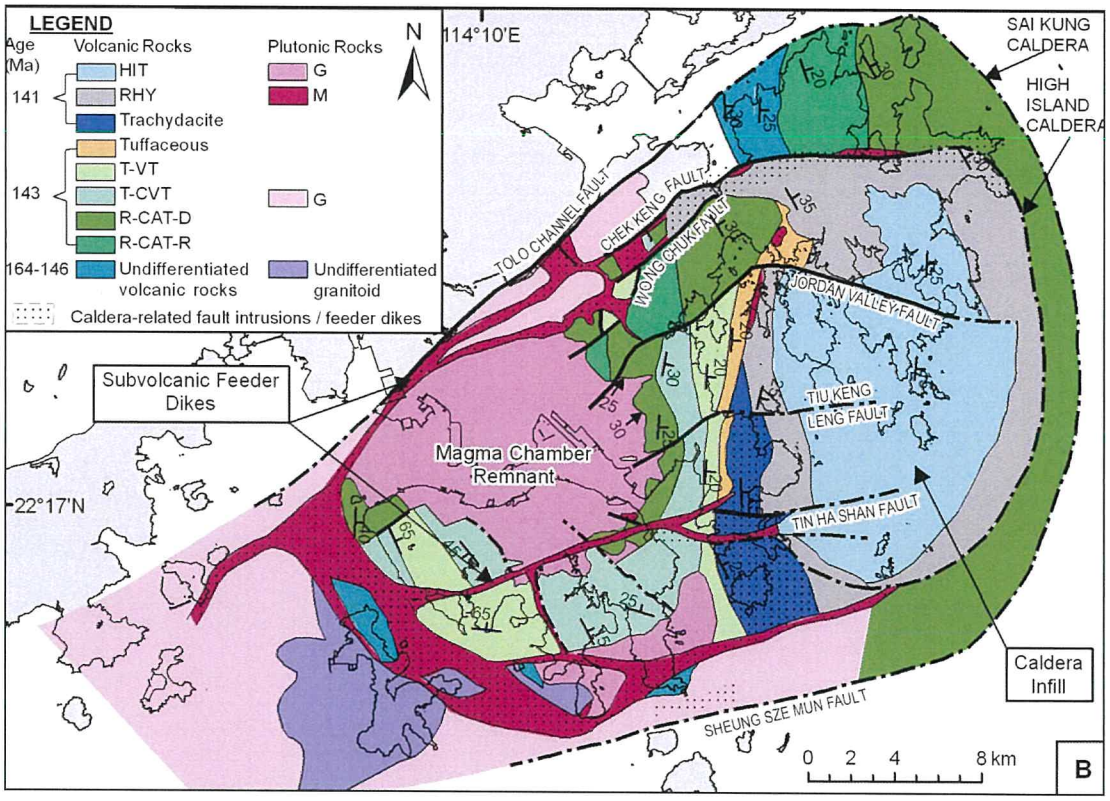

Figure 1. The late Mesozoic, titled nested High Island caldera complex in southeast Hong Kong (Sewell et al., 2012a).

The discovery laid the groundwork for detailed investigations of the magmatic history surrounding the late Mesozoic, large silicic magmatic systems in Hong Kong. To track the evolution of these systems, in-situ zircon U-Pb dating coupled with zircon trace element analysis using secondary-ion mass spectrometry (SIMS) was carried out on both volcanic rocks and sub-volcanic granites (Tang et al., 2017). The latest age data have shown that direct linkages previously proposed between some volcanic and plutonic units (e.g. High Island Tuff and Kowloon Granite) are no longer supported, and that magmatism represented by exposed plutons continued until ~137.8 Ma (Mount Butler Granite).

Based on zircon saturation temperatures and chemistries of both volcanic and plutonic units, two volcanic-plutonic groups in the High Island system have been identified (Tang

et al., 2017). One group, which comprises the Repulse Bay Volcanic Group and Shui Chuen O, Kowloon and Mount Butler granites (referred to as "cold" granites; *sensu* Miller et al., 2003), contains inherited zircons back to 164 Ma and wider ranges in Hf, Y and total trivalent elements, Th and U concentrations and Th/U, Yb/Gd and U/Yb ratios (Figure 2). The other group, which includes the Kau Sai Chau Volcanic Group and So Kwu Wan Granite and D'Aguilar Quartz Monzonite (referred to as "hot" granites; *sensu* Miller et al., 2003), does not contain inherited grains and has narrower ranges in zircon trace element concentrations and elemental ratios (Figure 2).

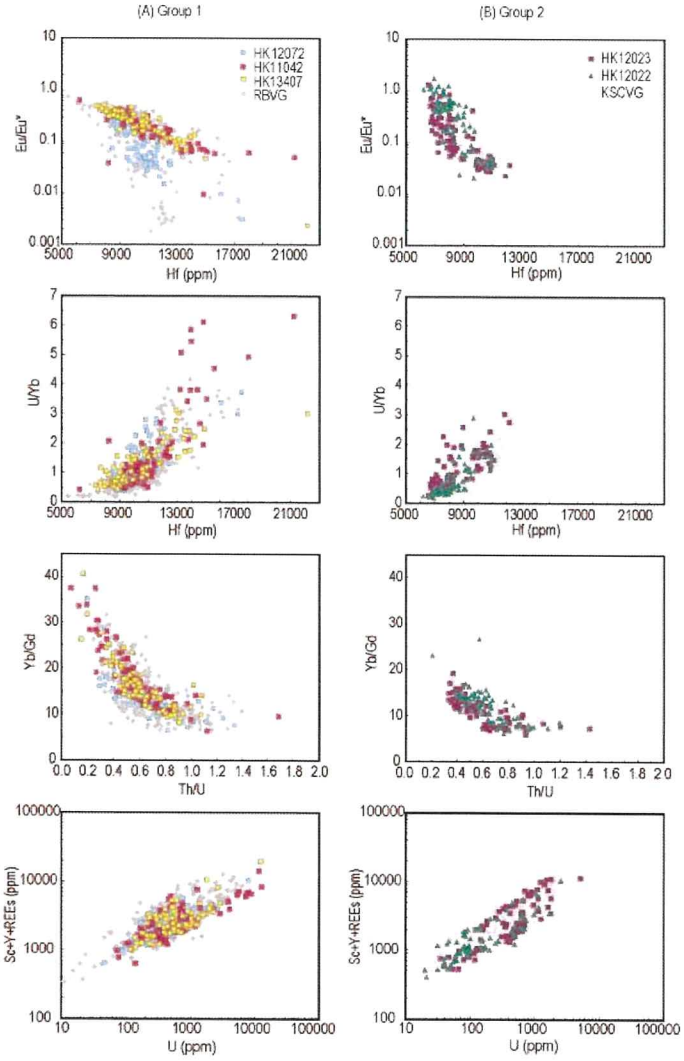

Group 1 "Cold" granites

HK12072 Shui Chuen O Granite

HK11042 Kowloon Granite

HK13407 Mount Butler Granite

Group 2 "Hot" granites

HK12023 Sok Kwu Wan Granite

HK12022 D'Aguilar Quartz Monzonite

Figure 2. Selected zircon trace element plots of intrusive units from High Island caldera complex, illustrating contrast in zircon chemistries of the two volcanic-plutonic groups (Tang et al., 2017).

Tang et al. (2017) proposed two possible evolutionary models for the High Island caldera

magmatic systems: (1) the system randomly tapped a single magmatic domain that fluctuated in temperature as a result of varying interactions of hotter melts; alternatively, (2) the volcanic and plutonic records reflect the interplay of two domains with contrasting "low" and "high" temperatures characteristics. The volcanic-plutonic records in Hong Kong have provided new perspectives and insights on the origin of silicic magmas and the links between the erupted and intrusive products (see Miller, 2017). The study has demonstrated that some plutons, such as the Kowloon and Mount Butler granites, were emplaced as independent magmatic pulses at shallow crustal levels and unrelated to volcanism; in contrast, other intrusions, such as the Sok Kwu Wan Granite and the D'Aguilar Quartz Monzonite, are closely linked (i.e. co-magmatic) to voluminous volcanic eruptions (Tang et al., 2017). The Hong Kong records have, therefore, reflected the current two end-member views of volcanic-plutonic relationships (see Lundstrom and Glazner, 2016).

SEDIMENT PROVENANCE FROM DETRITAL ZIRCON ANALYSIS

U-Pb dating and Hf isotope analysis of detrital zircons from late Palaeozoic and Mesozoic sedimentary sequences in the northeastern New Territories have provided much information on sediment sources, maximum depositional ages of individual units and the characteristics of crustal basement terranes (Sewell et al., 2016). Detrital zircons from 19 sedimentary rock samples from both side of the Tolo Channel Fault were dated using LA-ICP-MS techniques. In addition, Hf isotope analyses were carried out on six selected samples.

The detrital zircon age data were presented in probability density plots that showed the age spectra of individual samples (Figure 3). The dating results together with the Hf isotopic data were combined for evaluating the sediment provenance. The findings have shown a noticeable difference in zircon age spectra for Early to Middle Jurassic sediments from either side of the Tolo Channel Fault. Those from the north contain zircons as young as ~180 Ma with major populations at ~236 Ma, 436 Ma, 760-1200 Ma, 1860 Ma and 2500 Ma. The sediments were probably mainly sourced from exposed Proterozoic basement as well as Indonesian magmatic rocks (Sewell et al., 2016). In contrast, those samples collected from the southern side of the Tolo Channel Fault yield mostly Precambrian grains, with major populations at ~580 Ma, 790 Ma, 970 Ma, 2490 Ma and some Archean grains (~3,550 Ma). The sources of these zircons were considered to be quite distinct from the rest of Cathaysia, and reflect contributions from Jiangnan metamorphic basement and Mesoproterozoic crustal sources, along with some very

ancient crustal materials (Sewell et al., 2016). For the late Palaeozoic sediments, detrital zircon spectra are similar for samples from both side of the Tolo Channel Fault with key populations at 440 Ma, 760-1200 Ma and 2500 Ma.

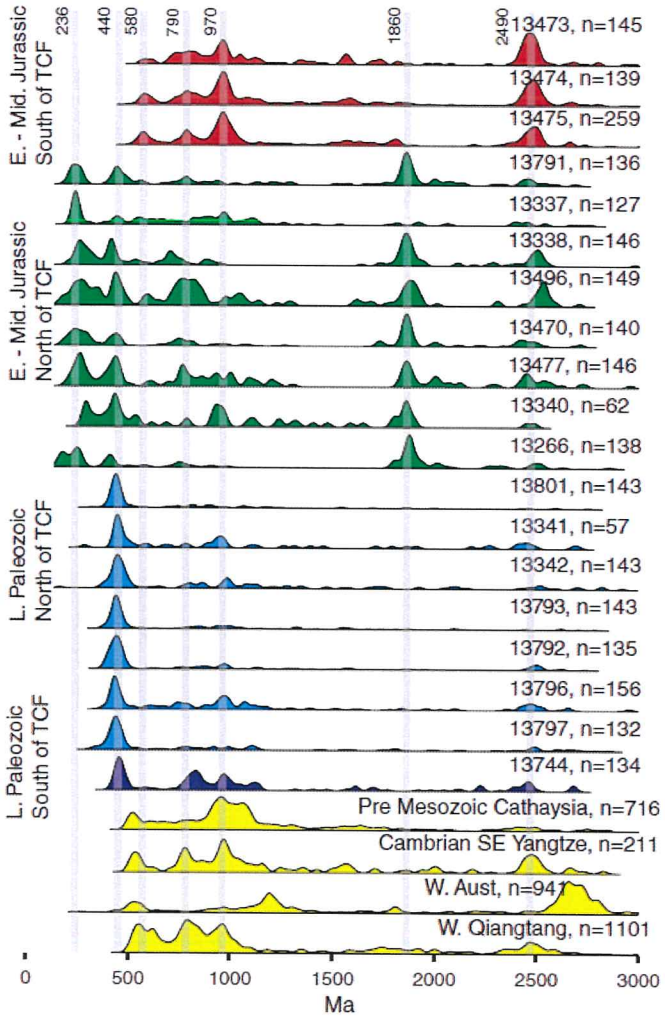

Figure 3. Probability density plots of detrital zircon U-Pb ages of the sedimentary units in the northeastern New Territories (Sewell et al., 2016).

Sewell et al. (2016) interpreted the contrast in detrital zircon ages and Hf isotope signatures of samples from either sides of the Tolo Channel Fault as the evidence of a NE-trending suture zone, along which an exotic terrane accreted to the southeast China continental margin during the Middle Jurassic. The postulated terrane collision might have triggered a re-configuration of the subduction system in southeast China, signified by the transition to an extensional tectonic regime and widespread granitic intrusions at ~160 Ma (Sewell et al., 2016).

POST-MAGMATIC EXHUMATION AND TECTONIC HISTORY

The post-magmatic evolution of Hong Kong was previously considered to be fairly uneventful, with the development of a series of Cretaceous fault-bounded basins followed by a long tectonically stable period (Lai, 1985; Sewell et al., 2000). However, some geochronological evidence (e.g. Ar-Ar dating of fault materials, Campbell and Sewell, 2005) pointed to possible periods of later tectonic and/or thermal events. To investigate the post-volcanic thermal-tectonic history, in particular the timing of burial and exhumation of the late Mesozoic rocks, low-temperature thermochronology (zircon and apatite fission-tracks, ZFT and AFT) on the Middle Jurassic to Early Cretaceous volcanic-plutonic assemblages as well as Cretaceous sediments in Hong Kong was carried out (Tang et al., 2014). In addition, U-Pb dating of detrital zircons from the Cretaceous sediments using laser ablation inductively coupled plasma mass spectrometry (LA-ICP-MS) was conducted to identify potential sediment sources and to constrain the maximum depositional ages (Tang et al., 2014).

The ZFT ages of the late Mesozoic magmatic rocks in Hong Kong range between 140 and 60 Ma, with most between 100 and 80 Ma; whereas the AFT ages range between 83 and 40 Ma, with two outliers (Figure 4). Tang et al. (2014) showed that both the ZFT and AFT systems have been reset, implying that the magmatic rocks experienced post-emplacement heating to a temperature exceeding 250°C. The thermal effect was probably due to a combined result of heating owing to burial plus an elevated geothermal gradient driven by continuing Yanshanian magmatism in the region (Tang et al., 2014).

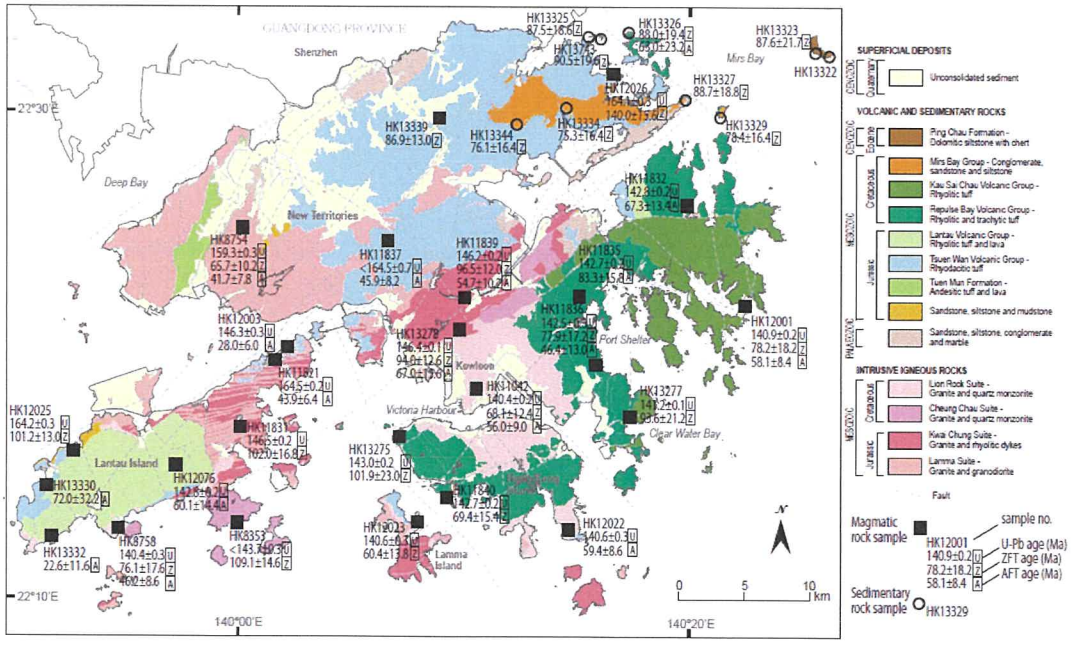

Figure 4. ZFT, AFT and detrital zircon U-Pb ages after Tang et al. (2014).

The results of the fission track analysis and U-Pb dating of detrital zircons from the Cretaceous sedimentary units have confirmed that the sediments were mostly sourced from local volcanic-plutonic assemblages. The presence of ~120 Ma detrital zircons from Pat Sin Leng Formation (1) indicates the occurrence of younger magmatic activities in Hong Kong and/or neighboring Guangdong Province; and (2) constrains the maximum age of Cretaceous basins in Hong Kong. Tang et al. (2014) proposed that from at least 120 Ma, the magmatic rocks and Cretaceous sediments in Hong Kong behaved as a single package and were heated to over 250°C, before cooling through the ZFT closure temperature by 100-80 Ma. The initial rapid cooling, linked to both geothermal adjustment and unroofing by erosion, was followed by a slow cooling (~1°C per million years) since 60 Ma owing solely to erosion-driven exhumation of 2-3 km (Tang et al., 2014).

GEOLOGICAL MODEL FOR THE NORTHWEST NEW TERRITORIES

Over the past years, considerable research on the Tuen Mun Formation has been undertaken by the HKGS with a view to resolving the on-going debate on the geological model for the unit (e.g. Lai et al., 2004; Tang, 2007; Lai and Chan 2012; Lai, 2016). As part of the 1:20,000-scale geological map updating exercise, a comprehensive review of all available data, including over 10,700 existing drillhole records, and examination of 400 rock samples and thin sections, has been carried out. Based on the extensive review of all known lithologies of the Tuen Mun Formation, So and Sewell (2017) presented a recommended classification and description scheme, which follows the nomenclature system given by the British Geological Survey (BGS) and the International Union of Geological Sciences (IUGS).

So and Sewell (2017) identified four main lithotypes, namely andesites (lava and intrusions), pyroclastic (tuff and tuff-breccia), mixed pyroclastic-epiclastic, and epiclastic rocks, in the Tuen Mun valley area. Sewell et al. (2017) conducted a lithofacies analysis and assigned these four lithotypes to three member units of the Tuen Mun Formation. They are, from the oldest to the youngest, the Tin Shui Wai, Siu Hang Tsuen and Tuen Mun Andesite members (Figure 5). To determine the maximum depositional age and provenance characteristics of the member units, U-Pb dating of the detrital zircons using LA-ICP-MS was carried out on seven samples (Sewell et al., 2017). In addition, zircon Hf isotope was analyzed on one selected sample to investigate the signature of crustal sources.

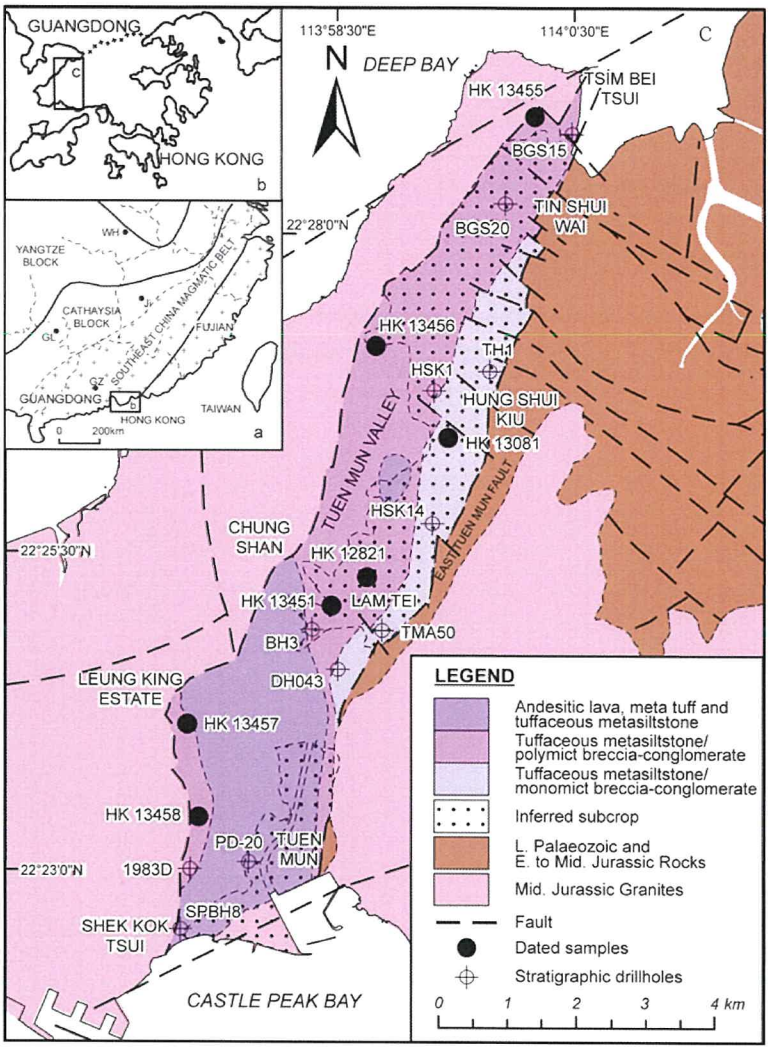

Figure 5. Solid geology map of the Tuen Mun valley, showing the location of dated samples and reference drillholes (Sewell et al., 2017).

Most of the detrital zircons obtained from the samples were large, euhedral, and zoned crystals, indicative of a volcanic provenance (Sewell et al., 2017). The results of detrital zircon dating yielded a youngest coherent age group at ~170 Ma, thereby constraining the maximum deposition age of the unit (Sewell et al., 2017). Based on the detrital zircon age signatures and Hf isotope data ($\varepsilon_{Hf}(t)$ = 0 to -11), Sewell et al. (2017) proposed that the zircon grains crystallized from a magma derived from recycled crustal sources, but having no interaction with the late Palaeozoic and Early to Middle Jurassic sediments that are now exposed nearby, or the late Mesozoic magmatic rocks in Hong Kong.

The Tuen Mun Formation has been interpreted to have accumulated in a forearc basin dominated by an emergent andesitic volcanic massif (Figure 6; Sewell et al., 2017). The

depositional setting varied from a subaerial, fluvial-dominant volcanic plain gradually to an offshore marine environment, signified by the three member units. The proximal facies is represented by the Tuen Mun Andesite Member, preserving mostly primary volcanic characteristics. The Siu Hang Tsuen and Tin Shui Wai members have been interpreted as the medial and distal facies respectively, and which have varying magmatic and fluvial inputs with diminishing terrestrial sediment sources in the distal facies (Sewell et al., 2017). Combined with the structural interpretation, the Tuen Mun Formation was probably emplaced as an allochthonous block, juxtaposed with adjacent sedimentary sequences, during the late Middle Jurassic (Sewell et al., 2017).

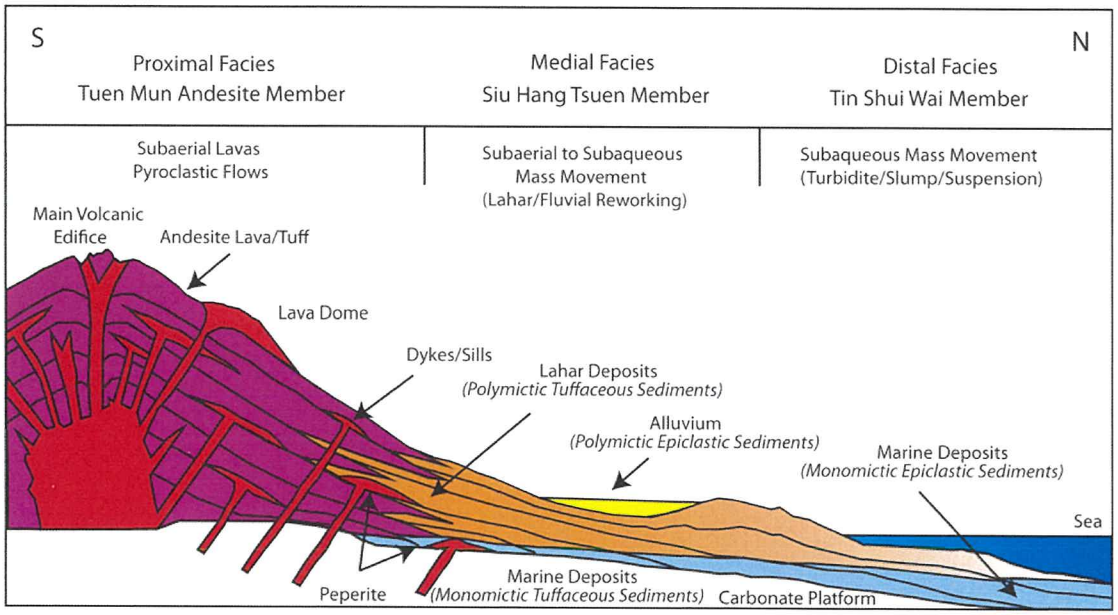

Figure 6. Proposed depositional model for the Tuen Mun Formation (Sewell et al., 2017).

LANDSLIDE HAZARDS AND LINKS TO PALAEO-CLIMATE

In 2001, the HKGS commenced an integrated pilot study to assess the accuracy and reliability of previously used and recently developed new dating techniques applicable to the dating of relict natural terrain landslides in Hong Kong (Sewell and Campbell, 2005). The findings showed that three dating techniques, i.e. optically stimulated luminescence (OSL), radiocarbon (^{14}C) and surface exposure (cosmogenic isotopes: ^{10}Be and ^{26}Al) dating, could be applied successfully to dating of ancient landslide scarps and debris lobes. In particular, it was demonstrated that surface exposure dating could be applied to large, deep-seated landslides, and rock and boulder fall failures, despite the seemingly unfavourable circumstances in Hong Kong of low latitude and low altitude (Sewell et al., 2006). The application of these dating techniques has recently been broadened to

investigate the relationship between landslide activity and palaeo-climate (Sewell et al., 2015) and evidence of a potential link between neotectonic activity and large landslides (Sewell and Tang, 2012, see discussion below).

Sewell et al. (2015) examined the stratigraphy of five large debris fans deposited along the coastal foothills of western Lantau Island, and analyzed 46 OSL and five radiocarbon ages obtained from these landslide deposits. The age data suggested that these five debris fans were accumulated during six main periods of landslide activities at: 28-20 ka, 14.5-10.5 ka, 5.8-5.0 ka; 4.37-4.23 ka, 3.56-3.32 ka and 1.35-1.05 ka. The two older landslide events were characterized by thick debris flow deposits (1.0-3.5 m); whereas the younger events (<10 ka) were represented by thinner units (0.5-1.5 m).

Sewell et al. (2015) hypothesized that cool and dry climatic periods during the last glacial period might have promoted accumulation of weathered materials, contributed to large amounts of sediments that were then mobilized as thick debris flow deposits in the two older landslide phases. In contrast, the warmer, more humid climate with high precipitations during early to middle Holocene might have led to possibly reduced sediment yields, more frequent flash floods and deposition dominated by debris floods (Sewell et al., 2015). The findings imply that there was a potential link between increased landslide activity and strengthening of the East Asian monsoon during the early to middle Holocene.

EVIDENCE FOR POTENTIAL NEOTECTONIC ACTIVITIES

The possible link between neotectonic activity (i.e. tectonic activity that has occurred during the Quaternary Period) that might have triggered enormous landslides was investigated at four sites in Hong Kong, including Ho Lei Pui, Wong Chuk Yeung, Tung Chung East, and Nam Shan and Pui O (Tang et al., 2009; Tang et al., 2010; Wong and Ding, 2010; Wong et al., 2010). For each site, detailed field mapping was followed by ground investigation and sampling of landslide scarps and debris for dating using the well-established radiocarbon, OSL and cosmogenic isotope dating techniques.

The findings of these studies were integrated with the age data of large natural terrain landslides in Hong Kong (Sewell and Campbell, 2005; Sewell et al. 2006) to reveal any apparent clustering of landslide events within distinct time frames, and thereby reflecting possible pulses of ground shaking. Sewell and Tang (2012) reported that four of the largest studied landslides (i.e. estimated debris volume $\geq$50,000 m^3), including Wong

Chuk Yeung, Tsing Yi, and Nam Shan and Pui O, yielded similar ages of around 50,000 years old. Another cluster of mostly deep-seated landslides occurred around 30,000 years ago. The two apparent clustering of widespread, large landslides at around 50,000 and 30,000 years ago possibly reflects evidence of neotectonic activities, although it is considered unlikely that the seismic sources were located locally (Sewell and Tang, 2012).

CONCLUSION

Over the past years, the HKGS has continued to engage actively in various research projects, which apply the latest techniques and geological concepts to gain new perspectives on local and regional geology. These advances are essential for continuous improvement of our geological maps, and for better understanding of our geological environment in support of hazard management, particularly related to natural terrain landslides and seismic risk.

REFERENCES

Addison, R., 1986. Geology of Sha Tin. Hong Kong Geological Survey Memoir No. 1, Geotechnical Control Office, Hong Kong.

Campbell, S.D.G., Sewell, R.J., 1997. Structural control and tectonic setting of Mesozoic volcanism in Hong Kong. Journal of the Geological Society, London, 154, 1039–1052.

Campbell, S.D.G., Sewell, R.J., 2005. 40Ar-39Ar Laser Microprobe Dating of Mafic Dykes and Fault Rocks in Hong Kong. GEO Report No. 206, Geotechnical Engineering Office, Civil Engineering and Development Department, The Government of the Hong Kong Special Administrative Region.

Campbell, S.D.G., Sewell, R.J. Davis, D.W., So, A.C.T., 2007. New U-Pb age and geochemical constraints on the stratigraphy and distribution of the Lantau Volcanic Group, Hong Kong. Journal of Asian Earth Sciences 31, 139-152.

Darbyshire, D.P.F., Sewell, R.J., 1997. Nd and Sr isotope geochemistry of plutonic rocks from Hong Kong: Implications for granite petrogenesis, regional structure and crustal evolution. Chemical Geology 143, 81–93.

Davis, D.W., Sewell, R.J., Campbell, S.D.G., 1997. U–Pb dating of Mesozoic igneous rocks from Hong Kong. Journal of the Geological Society, London 154, 1067–1076.

Fletcher, C.J.N., Campbell, S.D.G., Busby, J.P., Carruthers, R.M., Lai, K.W., 1997. Regional tectonic setting of Hong Kong: implications of new gravity models. Journal of the Geological Society, London 154, 1021–1030.

Frost, D.V., 1992. Geology of Yuen Long. Hong Kong Geological Survey Sheet Report No. 1, Geotechnical Engineering Office, Hong Kong Government.

Fyfe, J.A., Shaw, R., Campbell, S.D.G., Lai, K.W., Kirk, P.A. 2000. The Quaternary geology of Hong Kong. Geotechnical Engineering Office, The Government of the Hong Kong Special Administrative Region.

Lai, K. W., 1985. A review of the Late Cretaceous – Palaeogene fault basins around Hong Kong. In: Whiteside, P.G.D., Arthurton, R.S. (Eds.) Proceedings of the Seminar on the Marine Geology of Hong Kong and The Pearl River Mouth, Geological Society of Hong Kong, Hong Kong, 39-46.

Lai, K.W., 2016. Accurate geological data is the basis of urban development. Discussion on 'Guidelines on the Description and Classification of rocks of the Tuen Mun Formation'. In: Proceedings on the Asia–Pacific Forum on Mega Infrastructure and Urban Development Construction 2016, University of Science and Technology, The Hong Kong Institute of Engineers, Hong Kong, 1–11.

Lai, K.W., Chan, S.H.M., 2012. New evidence of palaeovolcanic plugs in the Tuen Mun area, Hong Kong: Debate on the volcanic plug or reworked pyroclastic deposits. In: Chen, M. (Eds.) Proceedings of the 30th Anniversary Conference of the Geological Society of Hong Kong, the Geological Society of Hong Kong, Hong Kong, 69-85.

Lai, K.W., Campbell, S.D.G., Shaw, R., 1996. Geology of the northeastern New Territories. Hong Kong Geological Survey Memoir No. 5, Geotechnical Engineering Office, Hong Kong.

Lai, K.W., Chan, H.H.K., Choy, C.S.M., Tsang, A.L.Y., 2004. The characteristics of marble clast-bearing volcanic rock and its influence on foundation in Hong Kong. In: Yeung, A.T. (Ed.) Proceedings of the Conference on Foundation Practice in Hong Kong, Centre for Research and Professional Development, Hong Kong, E1-E10.

Langford, R.L., 1994. Geology of Chek Lap Kok. Hong Kong Geological Survey Sheet Report No. 2, Geotechnical Engineering Office, Hong Kong Government.

Langford, R.L., James, J.W.C., Shaw, R., Campbell, S.D.G., Kirk, P.A., Sewell, R.J., 1995. Geology of Lantau District. Hong Kong Geological Survey Memoir No. 6, Geotechnical Engineering Office, Hong Kong Government.

Langford, R.L., Lai, K.W., Arthurton, R.S., Shaw, R., 1989. Geology of the Western New Territories. Hong Kong Geological Survey Memoir No. 3, Geotechnical Control Office, Hong Kong Government.

Lindstrom, C.C., Glazner, A.F. (eds.), 2016. Enigmatic relationship between silicic volcanic and plutonic rocks: silicic magmatism and the volcanic-plutonic connection. Elements 12, 91-127.

Miller, C.F., McDowell, S.M., Mapes, R.W., 2003. Hot and cold granites? Implications of zircon saturation temperatures and preservation of inheritance. Geology 31, 529-532.

Miller, C.F., 2017, Granites and rhyolites: Message from Hong Kong, courtesy of zircon. American Mineralogist 102, in press.

Sewell, R.J., 1996. Geology of Ma On Shan. Hong Kong Geological Survey Sheet Report No. 5. Geotechnical Engineering Office, Hong Kong Government.

Sewell, R.J., Barrows, T.T., Campbell, S.D.G., Fifield, L.K., 2006. Exposure Dating (^{10}Be, ^{26}Al) of Natural Terrain Landslides in Hong Kong, China. In: Siame, L.L., Bourles, D.L. and Brown, E.T. (Eds). In Situ-produced Cosmogenic Nuclides and Quantification of Geological Processes: Geological Society of America Special Paper 415, 131–146.

Sewell, R.J., Campbell, S.D.G., 1997. Geochemistry of coeval Mesozoic plutonic and volcanic suites in Hong Kong. Journal of the Geological Society, London 154, 1053–1066.

Sewell, R.J., Campbell, S.D.G., 2005. Report on the Dating of Natural Terrain Landslides in Hong Kong. GEO Report No. 170, Geotechnical Engineering Office, Civil Engineering and Development Department, The Government of the Hong Kong Special Administrative Region.

Sewell, R.J., Campbell, S.D.G., Fletcher, C.J.N., Lai, K.W., Kirk, P.A., 2000. The Pre-Quaternary Geology of Hong Kong. Geotechnical Engineering Office, Hong Kong.

Sewell, R.J., Carter, A., Rittner, M., 2016. Middle Jurassic collision of an exotic microcontinental fragment: Implications for magmatism across the Southeast China continental margin. Gondwana Research 38, 304-312.

Sewell, R.J., Darbyshire, D.P.F., Langford, R.L., Strange, P.J., 1992. Geochemistry and Rb-Sr geochronology of Mesozoic granites from Hong Kong. Transactions of the Royal Society of Edinburgh: Earth Sciences 83, 269–280.

Sewell, R.J., Davis, D.W., Campbell, S.D.G., 2012b. High precision U–Pb zircon ages from Hong Kong. Journal of Asian Earth Sciences 43, 164–175.

Sewell, R.J., Fyfe, J.A., 1995. Geology of Tsing Yi. Hong Kong Geological Survey Sheet Report No. 3, Geotechnical Engineering Office, Hong Kong Government.

Sewell, R.J., James, J.W.C., 1995. Geology of North Lantau Island and Ma Wan. Hong Kong Geological Survey Sheet Report No. 4, Geotechnical Engineering Office, Hong Kong Government.

Sewell, R.J., Kirk, P.A., 2002. Geology of Tung Chung and Northshore Lantau Island, Hong Kong Geological Survey Sheet Report No. 6, Geotechnical Engineering Office, Hong Kong Government.

Sewell, R.J., Parry, S., Millis, S., Wang, N., Rieser, U., DeWitt, R., 2015. Dating of debris flow fan complexes from Lantau Island, Hong Kong China: The potential

relationship between landslide activity and climate change. Geomorphology 248, 205-227.

Sewell, R.J., So, K.W.F., Tang, D.L.K., Carter, A., 2017. Unravelling an allochthonous, subaqueously deposited volcanic-epiclastic to subaerial andesitic lava assemblage in Hong Kong: Age, stratigraphy and provenance studies of the Middle Jurassic Tuen Mun Formation. Journal of the Geological Society, London 174, 913-928.

Sewell, R.J., Tang, D.L.K., 2012. The Potential Evidence for Neotectonic Fault Movement and Correlation with Natural Terrain Landslides in Hong Kong, GEO Report No. 307. Geotechnical Engineering Office, Civil Engineering and Development Department, The Government of the Hong Kong Special Administrative Region.

Sewell, R.J., Tang, D.L.K., Campbell, S.D.G., 2012a. Volcanic-plutonic connections in a tilted nested caldera complex in Hong Kong. Geochemistry Geophysics Geosystems, 13, 1006.

Sewell, R.J., Wong, J.C.F., Campbell, S.D.G., Ho, K.K.C., Lee, C.W., Tang, D.L.K., Shaw, R., 2005. Updating of Hong Kong Geological Survey 1:20,000-scale geological maps. In: Switzer, A.D., Duzgoren-Aydin, N.S., (Eds.) Abstracts Volume of the Conference on Recent Advances in Geological Research of Hong Kong and the Pearl River Mouth Region, Department of Earth Sciences, The University of Hong Kong.

So, K.W.F., Sewell, R.J., 2017. Guidelines on the Description and Classification of Rocks of the Tuen Mun Formation in the Tuen Mun Valley, Northwest New Territories, GEO Report No. 327. Geotechnical Engineering Office, Civil Engineering and Development Department Office, The Government of the Hong Kong Special Administrative Region.

Strange, P.J., Shaw, R., 1986. Geology of Hong Kong Island and Kowloon. Hong Kong Geological Survey Memoir No. 2, Geotechnical Control Office, Hong Kong.

Strange, P.J., Shaw, R., Addison, R., 1990. Geology of Sai Kung and Clear Water Bay. Hong Kong Geological Survey Memoir No. 4, Geotechnical Control Office, Hong Kong.

Tang, D.L.K., 2007. Geology of Tuen Mun Area, NW Hong Kong: an Updated Model. MPhil thesis, University of Hong Kong.

Tang, D.L.K., Ding, Y.Z., Lee, C.W., Wong, J.C.F., Sewell, R.J., 2009. Study of The Potential Evidence For Neotectonic Fault Movement and Correlation with Natural Terrain Landslides in Hong Kong (Part 1: Ho Lek Pui Area). GR 1/2009. Geotechnical Engineering Office, Civil Engineering and Development Department, The Government of the Hong Kong Special Administrative Region.

Tang, D.L.K., Seward, D., Wilson, C.N.J., Sewell, R.J., Carter, A., Paul, B., 2014. Thermotectonic history of SE China since the Late Mesozoic: Insights from detailed

thermochronological studies of Hong Kong. Journal of the Geological Society, London 171, 591-604.

Tang, D.L.K., Sewell, R.J., Wong, J.C.F., Ding, Y.Z., 2010. Study of The Potential Evidence For Neotectonic Fault Movement and Correlation with Natural Terrain Landslides in Hong Kong (Part 3: Tung Chung East). GR 3/2010. Geotechnical Engineering Office, Civil Engineering and Development Department, The Government of the Hong Kong Special Administrative Region.

Tang, D.L.K., Wilson, C.N.J., Sewell, R.J., Seward, D., Chan, L.S., Ireland, T.R., Wooden, J.L., 2017. Tracking the evolution of late Mesozoic arc-related magmatic systems in Hong Kong using in-situ U-Pb dating and trace element analysis in zircon. American Mineralogist 102 (in press).

Wong, J.C.F., Ding, Y.Z., 2010. Study of The Potential Evidence For Neotectonic Fault Movement and Correlation with Natural Terrain Landslides in Hong Kong (Part 2: Wong Chuk Yeung Area). GR 1/2010. Geotechnical Engineering Office, Civil Engineering and Development Department, The Government of the Hong Kong Special Administrative Region.

Wong, J.C.F, Tang, D.L.K., Sewell, R.J., Lee, C.W., 2010. Study of The Potential Evidence For Neotectonic Fault Movement and Correlation with Natural Terrain Landslides in Hong Kong (Part 4: Nam Shan and Pui O Areas). GR 4/2010. Geotechnical Engineering Office, Civil Engineering and Development Department, The Government of the Hong Kong Special Administrative Region.

ACKNOWLEDGEMENTS

This paper is published with the permission of the Director of Civil Engineering and Development and the Head of the Geotechnical Engineering Office, the Government of the Hong Kong Special Administration Region.

Brittle Characteristics Of Hard Rocks Under Thermo-Mechanical Coupling And Temperature Effect Of Rockburst

Tianbin Li
College of Environmental and Civil Engineering
State Key Laboratory of Geohazard Prevention and Geo-environment Protection
Chengdu University of Technology, China

Abstract

The thermo-mechanical (TM) coupling effect of rock mass is becoming one of the most important research topics due to the high geothermal and high geostress in deep underground engineering in Western China. Therefore, most of the researchers will focus on the brittle characteristics of hard rocks that influenced by high temperature (>30°C) and TM coupling rockburst.

In this report, the speaker mainly introduces the research advances in three parts. (1) TM brittle characteristics of hard rocks from laboratory test results. The energy index (Wet) and AE characteristics of TM coupling rocks are discussed in detail by uniaxial and tri-axial loading, tri-axial unloading and true tri-axial tests. (2) Theoretical calculation and numerical modelling of brittleness and fractures of hard rocks. An improved method for calculating brittleness index and a thermo-mechanical-damage constitutive model for hard rocks are proposed. (3) Physical modelling of temperature effect of rockburst. The developing process and mechanism of rockburst under TM coupling are reproduced and analysed in large scale physical modelling.

EARTH SCIENCE IN CUHK: CURRICULUM DEVELOPMENT AND RESEARCH IN THE FIRST FIVE YEARS

Teng-fong Wong, Lin Liu, Pui Yuk Tam and Hongfeng Yang
Earth System Science Programme, Faculty of Science
The Chinese University of Hong Kong

Abstract: Five years have elapsed since the first cohort of undergraduate students was admitted into the Earth System Science Programme in the Chinese University of Hong Kong in 2012. From scratch a curriculum that is truly interdisciplinary and quite unique in the region has been developed, with strong emphasis on quantitative skills and critical thinking, as well as a healthy balance of fieldwork, experiment and computation. In parallel a graduate division in Earth & Atmospheric Sciences was initiated in 2014. Specific to geoscience, research interests of faculty members cover geodesy, cryosphere geophysics, rock physics, seismology, and tectonophysics. Here we summarize the progress that has been made in development of the undergraduate and postgraduate curricula, as well as the research enterprise

INTRODUCTION

Founded in 1963, The Chinese University of Hong Kong (CUHK) has blossomed to be a comprehensive research university with a global vision and a mission to combine tradition with modernity. For half a century, the curriculum and research of the University have expanded to cover a diversity of disciplines, but for various historical reasons, geosciences is a discipline that had not been incorporated until the founding of the Earth System Science Programme in its Faculty of Science. The first cohort of undergraduate students was admitted into this interdisciplinary programme in August, 2012. Five years have elapsed, and here we review the progress that has been made in development of the undergraduate and postgraduate curricula, as well as research enterprise.

EARTH SYSTEM SCIENCE

Half a century is but a blink of an eye on geological time scale. Nevertheless, in the past five decades scientific advances on two fronts have fundamentally changed our perception of the planet we live in. The first advance is the formulation of the theory of plate tectonics (Oreskes, 2001). Before the 1960s when CUHK was founded, there was no generally accepted global theory to explain many of the intriguing features and processes of the earth. The accumulation and synthesis of data from paleomagnetism, marine geology and seismology then triggered a shift in the paradigm, and by the early 1970s, virtually all geoscientists have accepted the theory of plate tectonics as a unified framework for explaining the dynamics of major global features (continents and oceans,

mountains and valleys) as well as natural hazards (earthquakes, volcanic eruptions, tsunami).

The second advance is the emergence of a consensus among scientists regarding global change and how it is linked to anthropogenic inputs. It was only in 1958 that instrumentation was first deployed for the accurate monitoring of atmospheric carbon dioxide level (Keeling, 1998). The global data continuously accumulated over half a century have established indisputably that atmospheric carbon dioxide levels are increasing rapidly. Supplemented by related paleoclimate data, the observations have collectively demonstrated that indeed the concentrations of several greenhouse gases, not only carbon dioxide, have likely been increasing since the advent of the Industrial Revolution (IPCC, 2013).

To tackle the complex scientific questions related to global change, natural hazards and the earth's habitability, it is critically important to have a fundamental understanding of the dynamics of the earth as a coupled system, which includes the atmosphere, biosphere, geosphere, hydrosphere and cryosphere, as well as human impacts. This would hinge on scientific research that integrates traditional disciplines such as geology, meteorology and oceanography. Accordingly an interdisciplinary curriculum should also be developed to educate and prepare a new generation of students in this framework. Indeed it is in this spirit that the CUHK Earth System Science Programme was founded. This has also guided our development of curriculum and research in the past five years.

CURRICULUM DEVELOPMENT

We have established an undergraduate programme that is truly interdisciplinary and unique in the region, with curriculum that covers key aspects of Earth System Science. Overall our teachers are caring and have excellent communication skills. Their research approaches have a balanced mix of fieldwork, experiment and computation, which are integrated into our curriculum. We continuously revamp our curriculum to reflect the broadening interdisciplinary spectrum of Earth System Science. While we emphasize that students should have the breadth of knowledge, we also require them to probe more deeply into focused areas of their choices in their senior years. We place strong emphasis on the importance of quantitative skills and critical thinking.

Contrary to the conventional wisdom that such an approach may intimate and turn away prospective students, we have had success in recruiting high-quality students by a two-pronged approach. Whereas students who have targeted academic interests may opt for our specialized JUPAS admission scheme "*Earth System Science: Atmospheric Science/ Geophysics*", others whose interests are not as defined may first opt for the "*Science/ Broad-based Admission Scheme*" and later on declare Earth System Science as the major. Enrollment has continued to climb, and the cohort of majors (that were admitted in 2016) includes 22 and 18 students admitted through the former and latter schemes, respectively.

From scratch we initiated a postgraduate division on "*Earth & Atmospheric Sciences*" in 2014. In three years the number of research postgraduate students has reached 26. In the past two years, we organized summer workshops that brought in prospective graduate students, so they could be acquainted with our faculty and research and we could interview and identify some of the best students. These efforts have paid off, in that both quality and number of the applicant pool continue to improve. In the past two years, we

have recruited one Hong Kong PhD fellow each year. Both were identified when they attended our summer workshops.

RESEARCH IN EARTH SCIENCE

We have recruited a team of outstanding faculty, and they have established well-equipped facilities (related to atmospheric chemistry, atmospheric dynamics, near-surface geophysics, rock physics and seismology), some unique in the region. They have been undertaking cutting-edge research in key areas of Earth and Atmospheric Sciences. Specific to geoscience, our research interests cover cryosphere geophysics, geodesy, rock physics, seismology and tectonophysics. A healthy balance of field, experimental and computational efforts was achieved in our research enterprise, which has led to synergistic research advances from comprehensive field observations, systematic laboratory investigations, and numerical modelling on multiple scales. We have had a good track record of obtaining competitive research grants in the relatively short period of four years since inception of the programme.

The breadth and depth of our research enterprise are manifested by some of the research projects in Earth Science that have recently been funded by the Hong Kong Research Grants Council:

* *Investigation of characteristics and mechanism of earthquakes associated with the Hutubi gas reservoir.*
* *Mass Balance of Greenland Outlet Glaciers: Non-secular Variations From Space Geodetic Measurements.*
* *Radar remote sensing investigations on thermokarst dynamics on the Qinghai-Tibet Plateau.*
* *Kinematics and dynamics of active rock glaciers in western China.*
* *Dynamic controls on megathrust slip: Details from the Nicoya 2012 earthquake.*
* *Source characteristics of induced earthquakes associated with shale gas production in Weiyuan, Sichuan.*
* *Investigation of shallow seismogenesis on the southern Mariana megathrust.*
* *Experimental and digital rock physics in relation to hydraulic and electrical transport properties of porous sandstone.*
* *Effective stress laws for fluid flow and deformation of limestone as a dual porosity medium.*
* *Towards a multiscale understanding of compaction localization in highly porous sandstone based on a hierarchical multiscale modelling approach.*

Postgraduate students and postdoctoral associates are expected to actively participate in the broad range of research projects. We also require our undergraduate majors to undertake final year projects with integral research components. Each year the student with the most outstanding project is recognized by the Hong Kong Geological Society Best Undergraduate Research Prize, with funds generously contributed by Professor Lung Sang Chan.

The first two recipients of this research prize are:

* May Chim Man Mei (*Two distinct types of granulites in the Northern Hengshan Complex of the North China craton: Structures, P-T conditions and tectonic implications*; project directed by Drs. Jason Zhang Jian and Tammy Tam Pui Yuk, 2016).
* Rachel Lo Wing Sum (*Petrological study of Tang Chau - An implication of*

paleoenvironment of Tolo Channel; project directed by Drs. Tammy Tam Pui Yuk and Denise Tang Lai Kwan, 2017).

DISCUSSION

Earth System Science tackles and strives to provide scientific solutions to critical issues of local, national and global concerns in the 21st century, such as global change, natural hazards and the earth's habitability. There is a need to enhance and strengthen both the teaching and research efforts in this interdisciplinary area in the region. Establishment of the Earth System Science Programme in CUHK is an attempt to fill in this gap, and as reviewed herein, the development in the past five years has exceeded our initial expectation.

Earth System Science is very broad and interdisciplinary. There are still a number of key subdisciplines not being pursued by scientists in the region, and there is a paucity of qualified teachers. To initiate an academic unit from scratch, there is the temptation to overextend the scope and set the goals too high, which may lead to the instability to sustain either the teaching or the research efforts. Although we seem not vulnerable to such a threat, the present challenge is to consolidate, improve and reinvent our current teaching and research enterprises. The foundation has been laid in the past five years, and it is our belief that we are on track to sustained growth in future years, such that we will continue our mission to fulfill the immense needs for education and research in Earth System Science in the region.

REFERENCES

IPCC (2013), Climate Change 2013: *The Physical Science Basis. Contribution of Working Group I to the Fifth Assessment Report of the Intergovernmental Panel on Climate Change*. 1535 pp., Cambridge University Press, Cambridge.

Keeling, C. D. (1998), Rewards and penalties of monitoring the Earth, *Annu. Rev. Energy Environ.*, 23, 25-82.

Oreskes, N. (Ed.) (2001), *Plate Tectonics, An insider's history of the modern theory of the Earth*, 424 pp., Westview Press, Boulder, CO.

ACKNOWLEDGMENT

We thank the Organizing Committee of the Geological Society of Hong Kong - 35th Anniversary Conference 2017 for the invitation to present this review.

Investigation Of A Large, Structurally Controlled Landslide In Sai Kung East Country Park

Steven J Williamson
Technical Director of AECOM Asia Co. Ltd.

Abstract

An intense rainstorm on 21 May 2016 resulted in a cluster of 34 natural terrain landslides in the Sai Kung East Country Park Area, one of which was almost an order of magnitude larger than all the others with a source volume of about 2,100m^3. The landslide occurred above Sai Kung Sai Wan Road, a country park road and popular hiking trail, and the debris severely damaged the road resulting in closure for more than three months. The nature of the landslide was unusual in that it was a structurally controlled rock slide, with a basal failure surface formed from a persistent, planar sheeting joint within columnar jointed Tuff. The landslide had a maximum depth of about 12m, while the other landslides that occurred in the country park during the same rainstorm involved only shallow failures within soil regolith.

An investigation of the landslide was undertaken to determine the probable mechanism and causes of the failure, and to assess the potential risk of further large-scale failure of the remaining hillside. This presentation outlines the methodology, challenges and findings of the investigation.

New Evidence Of Activity In South Segment Of Chishan Fault, Southern Taiwan

I Chin Yen
Taiwan Association of Professional Applied Geologists
and
Chairman of the Yen I Chin Geological Office

Abstract

Chishan Fault, an active reverse fault, which is extending about 30km long in south western Taiwan. The fault trace can be segmented into two parts based on its exposure. The north segment of Chishan Fault is exposed and located in the south western Foothills of Chung Yang Shan, and the south segment is covered by Holocene deposits in Kaohsiung Plain. A 5m DTM (Digital Terrain Model) was used to discern possible fault scarps for the design of drilling sites along the south segment of Chishan Fault. Cross sections were drawn based on borehole data and C14 dating were carried out on samples taken from representative geological strata in various boreholes. We conclude that the latest event occurred after 18,000 years ago. Based on the projection of cross sections, we also conclude that the projected fault trace runs south eastwards along the west side of Teshe Hill and terminates in the area of Niaosaong.

Seismic Precursor To Instability Induced By Internal Erosion In Loose Granular Slopes

Wei Hu 胡偉

State Key Laboratory of Geohazard Prevention and Geo-environment Protection,
Chengdu University of Technology, China

Abstract

Fluidized landslides are one of the most dangerous types of mass movements as they can run over long distances at high velocity. A flow-like landslide can occur in both artificially designed and natural slopes, resulting in extensive property damage and significant loss of lives. Although various studies have examined the initiation mechanism of this type of landslide, our understanding of the phenomenon of instability which can occur in loose granular slopes deserves further attention. Specific influential factors such as the changes in the soil microstructure due to water infiltration and seepage forces still need to be further examined. In this study, the initiation of a fluidized landslide is investigated through flume tests. The tested material was collected from a coseismic landslide deposit in the 2008 Wenchuan earthquake area. These loose granular deposits can fail due to intense rainfall and exhibit flow-like movement, potentially evolving in destructive debris flows. Two flume apparatuses have been used, which were equipped with multiple sensors to evaluate the pore pressures and the internal displacements. A high-sensitivity seismic accelerometer was installed at the bottom of the flume to record the vibrations produced by the movement of the soil particles during the tests. The soil mass was progressively wetted either by a uniform inflow from the ground surface at the top of the slope, to simulate the infiltration of run-off water arriving from upslope, or by a gradual rise of the water level at the upper boundary of the slope, to simulate a gradual rise of the groundwater table. Internal erosion of the finer soil fraction driven by the seepage forces is thought to have played a significant role in the slope collapse. Possible changes in the particle arrangement were recorded by the accelerometers in the form of an increasing high-frequency vibration signal before any significant rise of pore pressure and any significant displacement of the slope could be observed. Although further parametric investigation is still necessary, and tests at real scale should be devised, the observed behaviour suggests that seismic monitoring of oose granular deposits can be a promising method for detecting an incipient slope collapse.

Phreatic Breccias in Hong Kong: Field Observations and Inferences

Lung Sang Chan
HKU School of Continuing and Professional Education and
Department of Earth Sciences, The University of Hong Kong, Hong Kong
chanls@hku.hk

Paleogene age hydrothermal episodes in the Hong Kong region are found to be associated with breccia pipes and silicification of host rocks. Such phreatic bodies have been observed at Ping Chau in Mirs Bay, Double Island, Crescent Island, and Luk Keng in Double Haven, Yim Tin Tsi Island in Sai Kung, and northern Lantau Island. Field observations of these phreatic features and thermodynamic consideration enable us to put constraints on the age, temperature and depth of the occurrence of the events.

The authigenic acmite minerals in the sedimentary sequence in Ping Chau, Mirs Bay are found to replace zeolite and earlier minerals in the Paleogene-age mudstone and biogenic sedimentary sequence. Relict bedding and stromatolitic structures observed in the silicified siltstone layer at Lung Lok Shui on the island are evidence for hydrothermal alteration (Fig. 1). The acmite also argues for a hydrothermal origin, since the synthesis of acmite requires a minimum temperature of about 300°C, which is much greater than the estimated temperature attainable from burial.

Fig. 1 Relict stromatolite structures in silicified siltstone, Ping Chau

At Double Island in Double Haven, folded sediments of Late Cretaceous age were silicified within a phreatic breccia pipe. The pipe resembles an inverted cone in geometry, with a silica-rich core zone and brecciated fragments on the margin. The core zone was about 50 m in width. Silica veins, folded layers, stockworks and pockets of breccia fragments are commonly present at the contact with the host rocks (Fig. 2). The structure, cutting across older volcanic and sedimentary formations, probably represents a phreatic

breccia pipe. A dike-like body exposed on the south shore of nearby Crescent Island shows similar silica stockworks and folded structures on the margin of the body. A 2-m wide semi-circular structure of highly silicified rock in Luk Keng probably represents another breccia pipe.

Fig. 2 Folded and silicified rock in Double Island

Another possible breccia pipe is present near the pier of Yim Tin Tsai Island in Sai Kung. The structure, about 10 m both in width and length, is represented by a highly silicified core zone with completely silicified rhyolite fragments in the host rock, and an outer zone of slightly greenish, silicified rhyolite and tuff (Fig. 3).

Fig. 3 Field sketch of phreatic breccia in Yim Tin Tsai, Sai Kung

On Lantau Island, fractures exhibiting radiating patterns are observed in a 3-m thick quartz dike (Fig 4). The fractures are found to nucleate from central points, suggesting a causal association with explosive events. Such explosions were probably caused by the sudden vaporization of superheated ground water. The process resembles the mechanism of boiling liquid expanding vapour explosion (BLEVE) leading to gas tank explosions. If so, the phase relation of water allows us to estimate the depth of the fracturing at about 300m beneath the surface.

Fig. 4 Radiating fracture patterns in quartz dike, northern Lantau Island

The observations presented here may have implications on the occurrence of breccia elsewhere. The breccia pipes in Arizona, USA are found to be associated with uranium ores at depth. While the breccia pipes observed locally are mostly siliceous in composition, they may plausibly possess a metalliferous zone at a greater depth.

Recently, the expansion breccia in a Jurassic limestone in the Northern Apennines, Italy has been attributed to phase conversion associated with CO_2 in the shallow subsurface. The observations in Hong Kong therefore bear some implications on the formation of the breccia in Italy and other parts of the world.

THE CHARACTERISTICS OF PALAEOVOLCANOES OF TUEN MUN FORMATION IN HONG KONG AND THE ASSOCIATED MISUNDERSTANDING

K.W.Lai[1], **M.Y.H.Li**[2],
[1] Former Hong Kong Geological Survey, Geotechnical Engineering Office, Civil Engineering Development Department
[2] Department of Earth Sciences, the University of Hong Kong

Abstract: There are widespread Mesozoic terrestrial volcanic rocks in Southeast China, which belong to the circum-Pacific continental margin tectonic area. Since the 1970s the understanding of Hong Kong geology has a significant development. Considerable field mapping data with numerous chemical analysis and thin section identification results on rock types indicated that the Tuen Mun valley is in a volcanic fault basin bounded by NE trending faults extending from Tuen Mun to Lo Wu (Figures 1 & 2). The volcanic activities of the Tuen Mun Formation first occurred in the Middle Jurassic Age. More than twenty fault-controlled volcanic plugs have been found in the basin. Most of the volcanic plugs are buried beneath the Quaternary superficial deposits varying from several metres to more than 20 m in depth along the east Tuen Mun Fault. Good exposures of volcanic plugs mainly occur along the western foothills of the Tuen Mun valley. All of them belong to terrestrial eruptions. The present Hong Kong Geological Survey published a set of guidelines (So & Sewell, 2017) on the description and classification of rock types of the region as a standard for geologists practicing in Hong Kong. The geological basis of the guidelines was presented in Sewell *et al.* (2017). Although the purpose and intention of these publications are sound, the critical problem is that their rock classification has not applied the geochemical analysis to determine the composition for all fine-grained volcanic rocks. The issue could have affected geotechnical engineering design and assessment considerably. Therefore, these errors should be avoided and improved.

INTRODUCTION

Sewell *et al.* (Sewell *et al.* 2017; So & Sewell 2017) have carried out considerable research and provided important contributions on the age dating, classification and interpretation of volcanic rocks of the Tuen Mun Formation. The critical problems of their rock classification does not follow the interpretation of the International Union of Geological Sciences (IUGS) Subcommission's recommendations. In particular, we consider rock classification with the aid of geochemical analysis for all fine-grained volcanic rocks is essential, and this is not adopted in So & Sewell's guidelines (2017). In addition, the lithofacies and the mode of occurrence have not been studied in detail to avoid confusion in recognition. It has been observed that plenty of recent drillhole logs in the Tuen Mun area are questionable as a result of the ambiguity of the guidelines. Some drill cores that have been identified as 'tuffites' or 'epiclastic rocks' which lack evidences. Any misidentification in lithologies may affect the application in geotechnical engineering in the Tuen Mun to Tin Shui Wai areas. Some geologists and engineers have presented alternative views on classifying rocks of the Tuen Mum Formation (see Chan and Kwong 2009; Chan *et al.* 2005; Lai, 2013 & 2016; Li *et al.* 2014). The aforementioned guidelines have not thoroughly considered other

practitioners' views.

GEOLOGICAL SETTING

The Tuen Mun Formation lies in a fault–bounded basin that extends northeastwards from Castle Peak Bay to Deep Bay. The fault basin is bounded by the NE trending Tsing Shan fault and Tuen Mun fault. Both faults belong to the deep-seated Linhuashan Fault which extends to East Guangdong and Fujian Province (Figures 1, 2 & 4). A marble-clast bearing andesite outcrop has been found at Shawanxu (沙灣墟) near the northern end of Shenzhen Water Reservoir (Lai, 2016).

The stratigraphic sequences related to the Tuen Mun Formation from oldest to youngest are as follows:

1. Devonian Bluff Head Formation consists of quartzitic sandstone with subordinate siltstone and quartz-pebbly conglomerate, representing fluvial and deltaic depositional conditions.
2. Carboniferous Yuen Long Formation consists of limestone and dolomitic limestone of marine deposits; but at a later stage it changes to the Lok Ma Chau Formation of terrestrial clastic deposits.
3. Permian formations of sandstone, mudstone with thinly bedded limestone.
4. Early Jurassic Tolo Channel Formation comprises interbedded black mudstone and siltstone with the presence of marine fossil 'ammonites' in transgressive strata. In the Early to Middle Jurassic Age, terrestrial sediments were deposited at time of crustal uplift in South China.
5. The total thickness of the above-mentioned strata is approximately 1800 m.

No rocks older than the lower Palaeozoic are exposed in Hong Kong. About 1 to 3 km to the north, Proterozoic gneiss and schist of Dagan Shan Formation and Ordovician granite occur in Shenzhen, isotopically dated at 485 to 1600 Ma. The granitic clasts found at Por Lo Shan in Hong Kong may be related to these older rocks (Figure 2)...

THE CHARACTERISTICS OF LITHOFACIES

Based on the eruption environment, relative position from source and the type of volcanic activity, the significant volcanic facies in Tuen Mun valley are illustrated as follows:

Volcanic Plug Facies (Figures 5, 12-15)

It is divided into crater eruption and fissure intrusion. The volcanoes are multiple erupted forming cycling stratigraphic deposits which are composed of explosive breccia and lava dykes. Surrounding the plug is widespread the fallout tuff or tuff breccia deposit and effusive lava flow.

Explosive Facies (Figures 6-8 and 19)

The explosive facies found in Tuen Mun Valley consists of pyroclastic materials and lava dykes produced directly in the volcanic plug as a result of violent explosion. The explosive breccias are of distinctive characteristics, including fragmentation and alteration, for recognition of the plug in the field. The fragmentation was likely resulted from thickly bedded rocks undergoing intensive crushing into very fine-grained materials. The alteration was likely caused by volatile, gas and hydrothermal solution of magma in contact with wallrocks, where reaction rims may result. The

fragments include juvenile lava congealed in early stage and the lithic clasts from the wallrocks, such as Devonian quartzite and sandstone, Carboniferous marble and dolomitic marble, Permian limestone and siltstone. The clasts are usually angular and cemented by lava; some clasts are of shuttle shape and parallel to the vertical plug wall. However, some are rounded due to in-vent abrasion during eruption process in some circumstances. At the contact between the lava and the pure marble, it appears to have formed the skarn minerals such as garnet and diopside. Where there is contact between lava and dolomitic marble, it formed tremolite and wollastonite. The reaction rim may not be clear because the minerals are white or pale grey colour.

The primary magma is probably basaltic, and it becomes more silica rich by means of fractionation and contamination with crustal rocks, such as sandstone, quartzite and granitoid, en route to the surface. These processes may have formed the andesite, dacite or rhyolitic tuff.

Effusion Facies
The effusion facies is mainly associated with the lava flows during quiescent eruption near the plug to a broader area far from the source. The lava is mainly fine-grained basaltic andesite. The thick sequence of andesite formed in an ancient valley. The borehole record of S13 (Figure 11) at the Tuen Mun Sea Water Service Reservoir shows that the total thickness of the massive andesite is more than 107 m.

Pyroclastic Flow Facies (Figures 4 and 5)
Pyroclastic flows are volcanically produced hot, gaseous, particulate density currents (Fisher & Schmincke 1984). The high temperature mixture of materials ejects explosively from a crater or fissures and travels swiftly down the slopes. The deposits occur at the west flank of South Por Lo Shan Plug and at a larger rock outcrop adjacent to a fault near Ling To Monastery. They contain subrounded blocks and spindle shaped lithic clasts, which are aligned parallel to the gently inclined layer. The deposits reveal five eruptive cycles with interbedded tuff breccia, tuff and lava. As the deposits are further away from the source of pyroclastic flow, the layers become thinner ranging from 0.2 m to 1 m in thickness.

Fallout Facies
The pyroclastic fragments fallen from eruption cloud or ballistic transportation formed cyclic deposits of interbedded crystal ash tuff and lava (Figure 10). The layers closest to the crater are thickly bedded of up to 4 m with a gentle dip angle. The pyroclastic materials reveal a heterogeneous and poorly sorted nature.

Eruptive-Sedimentary Facies
Tuffaceous sandstone is only found in localized areas such as a ridge near Yick Yuen Tsuen.

Sedimentary Facies
A sandstone outcrop (Sample TM166, Table 1) occurs at a ridge near an isolated outcrop of granite (1357E 2874N) 30 m long and 15 m wide dipping 244° to 265° at angle 60°. A 0.6-m thick lenticular shaped conglomerate is found in an intercalated bed within the pyroclastic layer near Por Lo Shan.

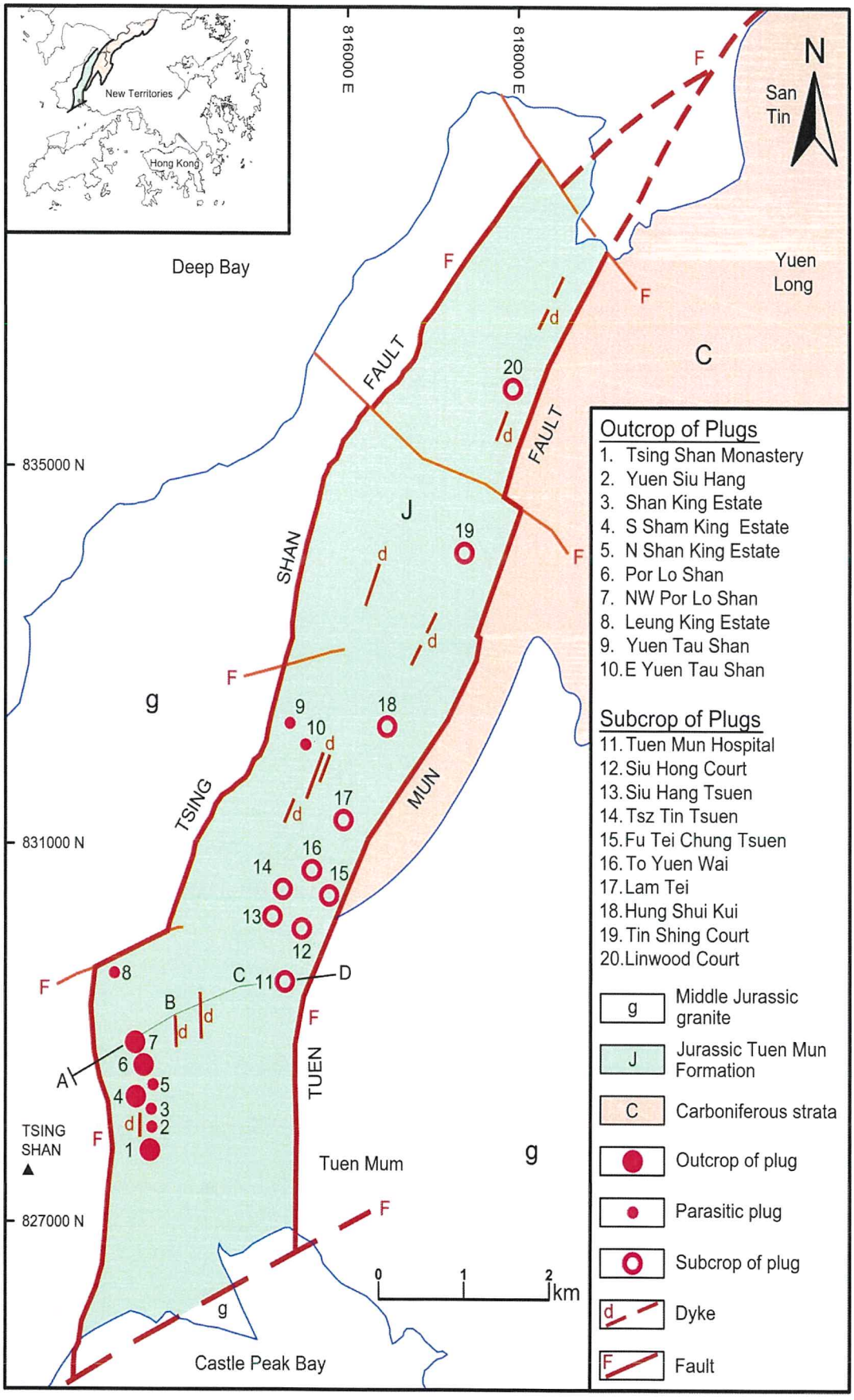

Figure 1 Geological Map of Palaeovolcanoes of Tuen Mun Formation, Hong

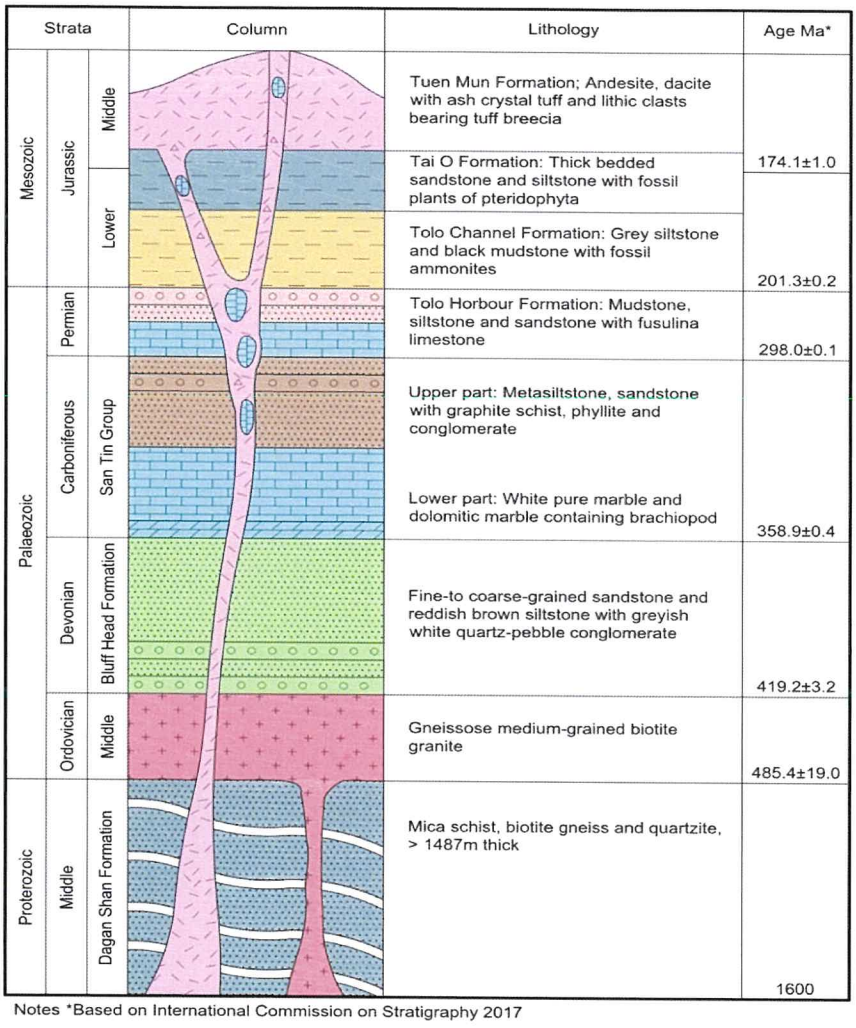

Figure 2. Pre-Middle Jurassic Stratigraphy of Hong Kong and the Vicinity

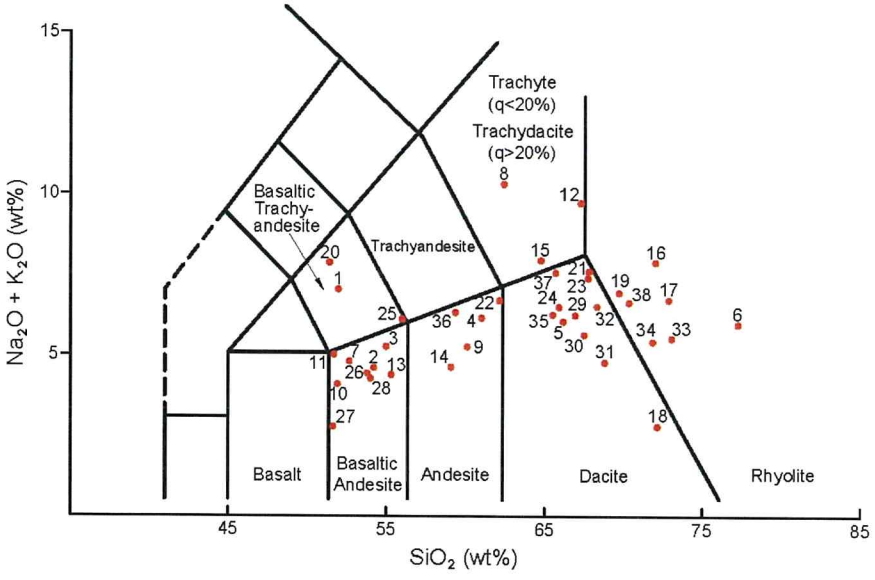

Figure 3. Total Alkali vs SiO_2 Plot for Analytical Results. The sample numbers are shown in Table 1

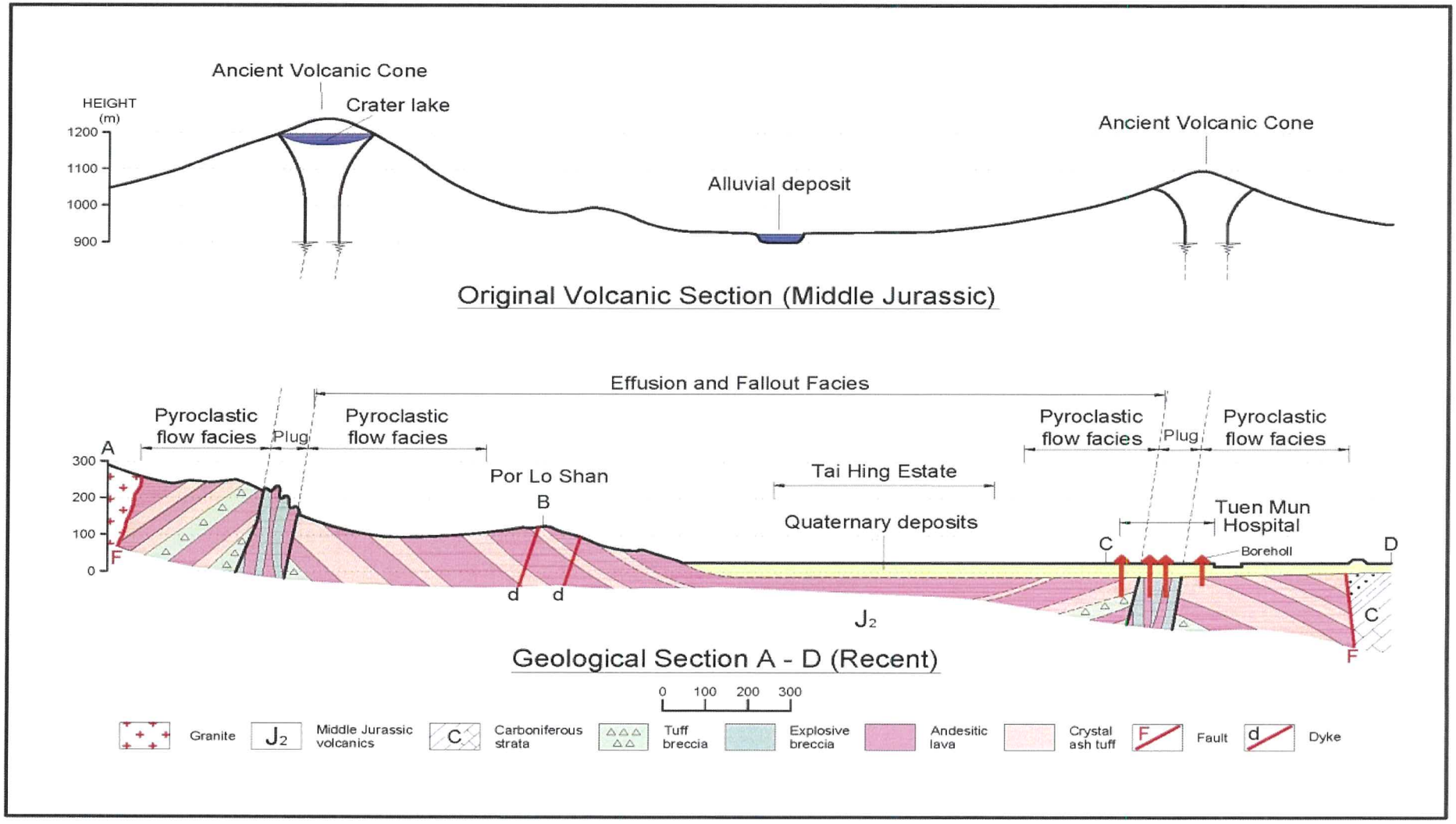

Figure 4. Middle Jurassic and Recent Geological Section A-D

Table 1. Whole Rock Major Element Concentration of the Tuen Mun Formation Rocks (Wt%)

No	Sample Number	Location	Coordinate		Rock Name	SiO2	TiO2	Al2O3	Fe2O3	MnO	MgO	CaO	Na2O	K2O	P2O5	LOI	Total
			E	N													
1	TM-1	TSM BH3 2.8m	1386	2809	Basaltic trachyandesite	52.360	0.745	17.621	7.315	0.078	3.224	9.971	3.420	3.531	0.509	1.100	99.873
2	TM-9	Por Lo Shan			Basaltic andesite	55.010	0.915	17.219	8.721	0.138	3.742	6.933	2.897	1.770	0.217	1.787	99.349
3	TM-16	Por Lo Shan			Basaltic andesite	55.830	1.006	17.352	9.198	0.139	4.171	6.272	2.686	2.396	0.217	0.686	99.955
4	TM-57	Shan King Parasitic Plug			Andesite	61.708	0.833	18.303	6.775	0.085	2.030	0.865	0.939	4.893	0.117	2.433	98.981
5	TM-58	Shan King Parasitic Plug			Dacite	67.036	0.457	17.083	3.568	0.050	1.626	0.939	1.197	4.949	0.091	2.257	99.253
6	TM-59	Shan King Parasitic Plug	1366	2865	Rhyolitic tuff	77.357	0.135	12.200	1.658	0.031	0.378	1.017	2.327	3.727	0.009	0.867	99.705
7	TM-61	Shan King Parasitic Plug	1366	2863	Basaltic andesite	53.283	1.047	17.838	10.582	0.147	3.602	6.654	2.662	2.152	0.247	1.765	99.979
8	TM62	Shan King Parasitic Plug			Trachydacite	63.159	0.161	18.230	2.155	0.045	3.742	0.933	2.316	7.955	0.041	1.037	99.774
9	TM-64	South Por Lo Shan	1366	2850	Andesite	60.777	0.673	17.587	6.501	0.089	2.951	5.009	2.960	2.179	0.266	0.799	99.792
10	TM-65	Tuen Mun Sea Water SR	1425	2889	Basaltic andesite	52.309	1.104	18.355	9.312	0.167	4.431	7.791	2.502	1.616	0.262	1.796	99.645
11	TM-65b	Tuen Mun Sea Water SR	1425	2889	Basaltic andesite	52.279	1.096	18.710	9.722	0.144	2.978	8.153	2.441	2.571	0.223	1.396	99.713
12	TM-71	West Shan King Estate	1366	2850	Trachydacite dyke	68.965	0.205	15.879	2.176	0.037	2.324	1.215	2.841	6.664	0.018	0.532	100.855
13	TM-73	Shan King Parasitic Plug	1368	2865	Basaltic andesite	56.290	0.760	19.190	8.920	0.170	3.950	1.110	0.420	3.960	0.100	4.830	99.690
14	TM-73b	Shan King Parasitic Plug	1368	2885	Andesite	59.810	0.810	18.540	7.030	0.160	3.150	1.560	0.510	3.790	0.160	4.510	100.880
15	TM-74	Shan King Parasitic Plug	1367	2863	Trachydacite	65.785	0.541	16.223	4.288	0.077	0.827	3.432	3.310	4.395	0.186	0.886	99.950
16	TM-77	East Por Lo Shan	1371	2862	Rhyolitic tuff	72.800	0.310	13.790	1.940	0.050	0.700	1.740	3.120	4.540	0.090	0.750	99.810
17	TM-83	TSW, Tin Tan St BH3 23m			Rhyoletic Tuff	73.933	0.553	12.140	3.130	0.031	0.765	2.252	3.534	2.586	0.106	0.410	99.441
18	TM-86	TSW104/BH83 113m			Dacite	72.959	0.616	10.424	6.881	0.060	2.929	0.544	0.101	2.476	0.082	2.402	99.473
19	TM-103	TSM ABH7 13.6m	1384	2808	Rhyoletic Tuff	70.750	0.300	13.100	1.910	0.050	0.880	3.230	1.530	5.240	0.080	2.650	99.710
20	TM-104	TSM BH3 2.5m	1386	2809	Basiltic trachyandesite	52.000	0.830	18.610	7.580	0.050	3.350	7.760	4.080	3.760	0.480	1.000	99.480
21	TM-106	TSM ABH7 14m	1384	2808	Dacite	69.260	0.300	13.770	1.920	0.050	0.880	3.420	1.730	5.400	0.080	2.940	99.730
22	TM-115	S Por Lo Shan	1365	2880	Andesite	62.896	0.739	18.267	5.748	0.055	1.515	0.142	0.431	6.162	0.087	2.742	98.783
23	TM-119	S Por Lo Shan	1368	2880	Dacite	69.197	0.502	11.392	3.998	0.168	1.313	4.500	3.062	3.954	0.119	0.771	98.974
24	TM-121	NE Shan King E. parasitic plug	1367	2865	Dacite	66.896	0.606	15.236	5.204	0.099	1.227	2.719	3.188	2.968	0.131	1.161	99.434
25	TM-124	W TSM TP2	1372	2772	Andesite	56.885	0.822	20.879	7.893	0.087	2.428	0.357	0.205	5.645	0.114	3.815	99.130
26	HK856	Tuen Mun Sea Water SR	1427	2889	Basaltic andesite	54.390	1.010	17.190	8.500	0.150	3.870	7.260	2.360	2.050	0.210	0.670	99.330
27	HK10247	Tuen Mun Water SR	1400	2880	Basaltic andesite	52.020	0.890	17.550	9.060	0.290	3.560	11.620	0.960	1.730	0.270	2.060	100.010
28	HK10379	Shan King Estate	1388	2858	Basaltic andesite	53.990	0.950	18.320	8.950	0.150	3.930	7.940	2.280	2.060	0.240	1.460	100.270
29	TM-135	TMA TM35 33.1m	1570	3069	Dacite	67.810	0.670	14.340	4.300	0.200	0.990	3.550	2.820	3.110	0.190	1.610	100.780
30	TM-136	TMA TM36 32.8m	1570	3072	Dacite	68.230	0.590	14.510	3.820	0.150	0.800	3.960	3.300	2.100	0.160	1.280	99.590
31	TM-137	TMA TM73 60.4m	1553	3066	Dacite	69.930	0.620	12.640	3.660	0.150	1.440	4.270	2.910	1.900	0.100	2.050	99.750
32	TM-138	TMA TM73 53.1m	1553	3066	Dacite	69.360	0.650	13.140	3.700	0.120	1.760	2.800	4.260	2.010	0.100	1.050	99.020
33	TM-144	TMA TMG40 43m			Rhyolitic	72.800	0.440	10.370	2.910	0.120	1.980	3.780	2.510	2.900	0.080	1.630	99.630
34	TM-145	TMA TMG46 32m			Rhyolitic	71.620	0.360	10.420	3.020	0.050	1.670	3.660	2.400	2.900	0.080	3.080	99.360
35	TM-10	Ling Tao Monastery	1607	3351	Dacite	65.950	10.580	6.040	0.170	0.780	1.010	9.470	2.340	3.800	0.110	0.730	100.980
36	TM-183	TSW Town Lot No 5 35m			Andesite	59.050	20.110	7.200	0.080	0.860	2.310	0.380	0.800	5.390	0.160	3.280	99.620
37	TM-185	TSW 103/C4 67.6m	1838	3606	Dacite	65.270	15.100	4.650	0.060	0.620	1.320	3.000	3.570	4.080	0.100	1.380	99.150
38	TM-186	TSW 103/C4 67.8m	1838	3606	Rhyolite	70.250	13.380	2.680	0.050	0.700	1.570	3.560	3.100	3.270	0.110	0.910	99.580
39	TM-168	Tsing Shan Au	1360	2888	Sandstone	85.390	0.290	7.650	1.390	0.020	0.330	0.020	0.060	2.690	0.010	1.610	99.500

Sample tested by : No.1-12 Hong Kong University, No.13-25 & 29-39 Guangzhou Institute of Geochemistry, No.26-28 Nottingham University
Notes : TSW--Tin Shui Wai, TSM--Tsing Shan Monastery, SR--Service Reservoir, TMA--Tuen Mun Area 54 Site 2 Tsz Tin Tsuen

PALAEOVOLCANIC PLUGS

Until now, twenty palaeovolcanic plugs have been found in the Tuen Mun valley. At least ten outcrops are exposed in the western flank of the valley and ten subcrops are covered by superficial deposits in the eastern plain area. Three excellent outcrops of typical plugs and two subcrops of buried plugs are introduced as follows:

Tsing Shan Monastery Plug (E1383 N2810; Figures 1, 5 to 10)
Tsing Shan Monastery and the adjacent pylons have been refurbished and maintained from 2008 to 2010. Fifteen boreholes have been sunk for ground investigation. After studying the drillhole data in detail and re-mapping the area, it is found that the monastery is situated above a palaeovolcanic plug which is a 'rain drop' shaped structure 130 m long and 50 m wide. Seven boreholes confirmed that the sub-vertical plug is composed of multiple injection dykes of explosive breccias and lavas. Four rock samples have been tested by chemical analysis of which two samples (TM1 and TM104) taken from drillhole BH3 (Figure 5) are lava dyke and were tested in two different laboratories. The results are both basaltic trachyandesite (Figure 3 & Table 1). The other two samples (TM106 and TM103) were taken from different depths of Drillhole ABH7, the results are dacite and rhyolite respectively. The basaltic trachyandesite, dacite and rhyolite were probably related at depth to a more basaltic primary magma which became more silica rich by fractionation and contamination with crustal rocks such as sandstone quartzite and granitoid en route to the surface. The mineralogy of the andesite comprises mainly of plagioclase and hornblende with minor biotite, augite, quartz and sphene as well as secondary minerals of epidote, chlorite and sericite. Most of the lavas have an aphanitic texture with phenocrysts of prismatic plagioclase, up to 6 mm long, in a matrix of basaltic trachyandesite. The explosive breccia dykes comprise lithic clasts of sandstone, siltstone and marble from wallrock and juvenile andesite fragments congealed at an early stage. They are subangular to subrounded in shape, 10 mm to 300 mm in size and cemented by the lavas. Contact metamorphism took place between the lava and marble clasts forming reaction rims that contain garnet, diopsite, tremolite and wollastonite. The lava flow direction inside the plug is parallel to the sub-vertical wallrock.

Around the plug is a fine ash crystal tuff, which is widespread in the southeastern part with a thickness of more than 10 m. Outside the tuff, the lavas of the effusion facies occurring on the ground surface are andesite as confirmed by the geochemical analysis. Six drillholes adjacent to the pylons 4CPA19 and 4CPA20 reveal that the rocks are interbedding andesite lava, ash tuff and tuff breccia, forming the flanks of the stratovolcano. The thickness of andesite varies from 0.5 m to 5.5 m whereas the tuff or tuff breccia varies from 4.9 m to 10.8 m.

Shan King Estate Plug (E1359 N2861; Figures 1, 3, 12 and 13, Table 1)
This plug is located at 600 m to the west of Shan King Estate. It is elliptical in shape and cylindrical in cross-section, up to 80 m long and 50 m wide forming a 50 m high upstanding outcrop. It is composed of multiple lavas and explosive breccias dykes. The explosive breccia represents violent eruption phases whereas the lava flows indicate quiescent eruption phases. The lithic clasts are cemented by an andesite matrix marked by reaction rims along the contacts of the two lithologies. The vertical eruptive lava flow is parallel to the plug. Very fine fumarole pipes, indicating typical volcanic activity features of gas explosive eruption, occur at the base of the plug and extend to the top (Figure 12). Seven lava dyke samples (Table 1 of this paper; Tables

2a & 2b in Lai 2016) from different parts of the plug were tested by chemical analysis, revealing a short spectrum of composition from dacite (five samples; TM56, TM 66, TM71, TM76 and TM122) to rhyolite (two; TM53 and TM123). The tuff breccia of pyroclastic flow deposits exposed at the southeast of the plug contains lithic fragments that are subangular to subround or spindle shaped. These lithic fragments' long axes are parallel to the gently inclined bedding. The vertical cracks produced an irregular columnar or tabular jointing.

The Shan King Estate Plug is associated with two parasitic plugs. The large one occurs 40 m southeast of the main plug (E1366 N2864). It is circular in shape, 35 m in diameter and 20 m in height. The lithic clasts are greyish white subrounded to rounded, crystal tuff varying from 20 mm to 200 mm in size, occasionally up to 800 mm. Eight samples (Table 1) were collected for chemical analysis. The results show that four samples (TM57, TM61 TM73 and TM73B) are andesite or basaltic andesite, another four (TM58, TM62, TM74 and TM121) are dacite and one (TM59) is ash crystal tuff congealed at an early stage. (Table 1). The tuff clasts are cemented by lavas forming explosive breccias. A special feature is that the parasitic plug exhibits concentric circular joint pattern with the explosive breccias occurring in the core of the plug (red dashed line in Figure 13).

South Por Lo Shan Plug (E1368 N2881; Figures 1, 3, 14 and 15, Table 1)
The plug is situated 550 m to the southwest of Por Lo Shan. It is sub-elliptical in shape, 85 m long, 50 m wide and approximately 55 m high. This plug consists of explosive breccia and lava dykes from multiple eruptions. The chemical analysis reveals a spectrum of composition from andesite (four samples; TM9, TM16, TM64 and TM115) through dacite (TM119) to rhyolitic lapilli crystal tuff (TM77). The lithic clasts are composed of Devonian quartzite and sandstone, Carboniferous limestone and lava fragments. When in contact with the matrix (magma), the margins of the limestone lithic clasts are chemically altered, forming reaction rims composed of skarn minerals such as garnet, tremolite, diopside, epidote or chlorite. The lava flow appears to have vertically erupted along the plug forming an upstanding outcrop in the mountain. The ash crystal tuff (TM77) is widespread on the eastern part, whereas the interbedded andesite (TM115) and tuff breccia of pyroclastic flow facies occur on the western part of the plug.

Tsz Tin Tsuen Plug (Tuen Mun Area 54 Site 2; E1570 N3072; Figures 1, 16 and 18)
The plug is elliptical in shape, 320 m long and 200 m wide, and buried beneath superficial deposits varying from 1.5 m to 10 m in thickness. This plug consists of explosive breccias and lava dykes from multiple eruptions. Most drillhole logs, core samples and photographs in the area have been examined in detail and explosive breccias have been identified in 30 drillholes. The eruption of the large plug was probably associated with a gas-rich magma which triggered violent explosion. Most of the rocks have been crushed to very fine-grained materials. The contact between marble clasts and lava is associated with skarnization producing garnet, epidote and chlorite minerals. The chemical analysis reveals a spectrum of composition from dacite (four samples; TM135–TM138, Figure 3 and Table 1) to rhyolitic tuff (two; TM144 and TM145). All lithic clasts are cemented by dacite or andesite.

Tin Shui Wai Plug (E1840 N3575; Figures 1, 3 and 17, Table 1)
This plug is buried beneath superficial deposits of 16 m to 18 m in thickness. It is

elliptical in shape, 150 m long and 110 m wide, and consists of explosive breccia and lava dykes. The lithic clast is composed of marble, sandstone and siltstone. Most drillhole logs and core photographs have been examined in detail and explosive breccias have been identified in 36 drillholes. The plug was associated with violent explosion for multiple times. Most lithic clasts have been crushed to bits. The contact between the marble clasts and the lava display reaction rims. The rock samples were collected from the vicinity of Tin Shui Wai for chemical analysis. The result shows that they are andesite (TM183), dacite (TM86 and TM185) and rhyolitic tuff (TM83 and TM186). All lithic clasts are cemented by the andesite or dacite lavas. Drill cores outside the plug are mainly lavas of effusion facies and tuffs of fallout deposits.

DISCUSSION

The GEO guidelines (So & Sewell 2017) and Sewell *et al.* (2017) have been a result of considerable research efforts, providing important contributions to Hong Kong geology on the age dating, classification and interpretation of volcanic rocks of The Tuen Mun Formation. We support their correct points but find that some areas need further deliberation. These areas include:

1. We suggest that the classification of fine-grained, aphanitic volcanic rocks of Tuen Mun Formation with the aid of chemical composition is essential. We also believe that the analysis of the lithofacies and the mode of occurrence in support of the GEO guidelines should have been done in more detail. So & Sewell (2017) contended that whole rock geochemistry cannot be reliably applied to the classification of most lithic- or clasts-bearing lithologies in the Tuen Mun Formation because these lithologies have been subjected to different types of metamorphism, which hinders the identification of original rock composition and textures. In fact, not all of the Tuen Mun Formation rocks have been metamorphosed. There are still some unmetamorphosed rocks within the Formation which can provide valuable samples for geochemical analysis. We have compared three unmetamorphosed rock samples, TM65, TM65b and HK856, taken from the same location, and analysed in different laboratories. The chemical results are essentially identical, Basaltic Andesite. This indicates that chemical analysis is a viable and indeed valuable method to study the Tuen Mun Formation. The GEO guidelines lack chemical data to support its rock classification and nomenclature system.

   In order to accurately recognize the volcanic rocks of the Tuen Mun Formation, a total of 62 rock samples were selected for geochemical analysis, and another 11 chemical data were collected from Geotechnical Engineering Office as shown in Tables 2a and 2b in Lai (2016) and Table 1 of this paper. We noted some of what have been identified as 'sedimentary' rocks following the GEO guidelines are instead volcanic in nature, and may cause confusion to some engineers. For instance, the 'tuffaceous conglomerate' (Figures 4.3, A17 and A18 of So & Sewell 2017) from Por Lo Shan, Shan King Estate and Tsz Tin Tsuen (Tuen Mun Area 54 site 2) should be explosive breccia and lava dyke of plug facies under our interpretation, and the 'sedimentary marble breccias/conglomerate' from Hung Shui Kiu to Tin Shui Wai areas (Figures A26 & A34 to A37 of So & Sewell 2017) should be explosive breccias or vent breccias.

2. Sewell *et al.* (2017) stated that the rock type of Tin Shui Wai Member is monomictic tuffaceous-epiclastic rocks, which represent an offshore submarine environment. The type Drillhole 29625/TH1 (Figure 19) has recovered the 'sedimentary marble breccia/conglomerate' with the vertical thickness in the borehole exceeding 75 m. However, these rocks have not been checked and identified by microscope and chemical analysis. Furthermore, we have re-examined these drillhole logs and photographs in detail. The grain size of the marble clasts varies from less than 0.1 mm to 60 mm. Most of them are fine-grained, with an angular, tearing and melted erosion texture. The proportion of marble clasts in the length of rock core is 60%. All marble clasts are cemented by volcanic lavas and are associated with explosive eruption in the volcanoes. The cementing materials of Core sample TH1 have been compared with similar rocks of Drillholes TM86, TM137 and TM183 in the same area (Figure 19). They are andesite or dacite as shown in Table 1. The marble is mainly derived from the Carboniferous or Permian carbonate rocks, which formed in a marine environment. The marble or limestone clasts not only occur in volcanic rocks of the Tuen Mun Formation but also occur in the volcanic rocks of the Tai Mo Shan Formation and the Shing Mun Formation. These rocks are produced by terrestrial explosive eruption in Middle Jurassic time. It is impossible for them to be formed in an offshore submarine environment.

3. Sewell *et al.* (2017) stated the Siu Hang Tsuen Member consists of polymictic tuffaceous-epiclastic rocks, which represent a fluvial-dominated volcanic plain environment. The type Drillhole BH3 and adjacent Drillholes BH1, BH2, and BH4 have been examined. Those rock cores consist of explosive marble clast-bearing breccias with lava flow. The contact between the marble and the lava display reaction rims composing of skarn minerals such as garnet and epidotes. These rocks are instead derived from a volcanic plug under our interpretation. The drillholes surrounding the plug mainly contain andesitic dacite or tuff which are not reworked by fluvial deposits.

4. Sewell *et al.* (2017) went on to propose a depositional model that the Tuen Mun Formation represents a complex volcanic arc-related basin featuring a sequence dominated by an emergent andesitic volcanic massif in the south, transitioning northward into a fluvial-dominated volcanic plain, and then to an offshore submarine environment. It, however, lacks evidence to support its volcanic arc-related basin model. According to the geophysical data from the Ministry of Geology & Mineral Resources of People's Republic of China, the Tuen Mun Formation is situated within the South China continental crust with a thickness of 26.5 km, at which the depth of the Moho discontinuity lies. As such, we are not convinced that an oceanic crust or arc-related environment existed (Guangdong Bureau of Geology and Mineral Resources 1988; Jin & Sun 1997). No geophysical data were provided in Sewell *et al.* (2017) to support the existence of a volcanic arc-related basin in South China.

   Based on comprehensive analysis of the data of stratigraphy, lithofacies and volcanic structure, we are more clung to the geological model in which the Tuen Mun Formation represents a fault bounded volcanic basin, with andesitic magmas erupted from craters and fissures, forming more than 20 palaeovolcanic plugs and

a series of dykes, sills and stocks within the basin.

CONCLUSIONS AND SUGGESTION

The geochemical analysis, thin section identification and considerable research results indicated that alternative interpretations and thus description and classification of rocks of the Tuen Mun Formation exist. We believe there is always room to improve GEO's guidelines for the Formation (So & Sewell 2017), and that using the present guidelines without a clear understanding of the Formation's geology would lead to unnecessary and serious problems in geotechnical engineering and geological works.

It is suggested that the Geotechnical Engineering Office should set up a working group to review the guidelines on the description and classification of rocks of the Tuen Mun Formation and correct the aforementioned geological errors, if any. Publication of a new set of guidelines would be needed.

ACKNOWLEDGEMENTS

The authors would like to offer sincere thanks to Professor M.F. Zhou of the University of Hong Kong for the chemical analysis, also to Dr R J Sewell for providing chemical data of GEO. The authors would appreciate the major assistance provided by H.M.S Chan, also to Colin Yeung, Eric Cheung and Carrie Lai for their invaluable assistance to prepare this paper.

REFERENCES

Chan, S.H.M. & Kwong, A.K.L. 2009. Enhanced and systematic classification system for rock types in Tuen Mun and Tin Shui Wai Area, Hong Kong. In *Proceedings of ISRM sponsored international symposium on rock mechanics, rock characterization, modelling and engineering design methods,* 1036–1042.

Fisher, R.V. and Schmincke, H-U. 1984. *Pyroclastic rocks*. Berlin.

Geotechnical Engineering Office 2007. *Hong Kong Geology Guide Book*. Geotechnical Engineering Office, Civil Engineering and Development Department, Hong Kong.

Guangdong Bureau of Geology and Mineral Resources 1988. *Regional geology of Guangdong Province*. Geological Publishing House, Beijing.

Jin, W.S. & Sun, D.Z. (Eds) 1997. *The deeper part of the crustal texture and its evolution of South China*. Geological Publishing House, Beijing.

Lai, K.W. & Chan, H.M.S. 2012. New evidences of palaeovolcanic plugs in Tuen Mun area, Hong Kong-Debate on the volcanic plug or reworked pyroclastic deposits. *Proceeding of Geological Society of Hong Kong-30th Anniversary Conference,* 69–85.

Lai, K.W. 2013. The characteristics and misjudgement of cavernous marble and their influence on foundation design in Hong Kong. *Proceeding of HKIE Geotechnical Division 33rd Annual Seminar,* 217–224.

Lai, K.W. 2016. Accurate geological data is the basis of urban development-Discussion on "Guideline on the description and classification of rocks of the Tuen Mun Formation". In *Proceedings on the Asia-Pacific Forum on mega infrastructure and urban development construction*, HKUST.

Le Maitre, R.W. (ed) Streckeisen, A., Zanettin, B., Le Bas, M.J., Bonin, B., Bateman,

P., Bellieni, G., Dudek, A., Efremova, S., Keller, J., Lamere, J., Sabine, P.A., Schmid, R., Sorensen, H. & Woolley, A.R. 2002. *Igneous rocks: A classification and glossary of terms.* 2nd Edition, Cambridge.

Li, Y.H.M. Zhou, M.F. Lai, K.W. Chan, L.S. & Chen, W.T. 2014. Geochemical and geochronological constraints on Late Jurassic volcanic rocks at Tuen Mun, Hong Kong, with implications for the Palaeo-Pacific subduction. *International Geology Review*, 1–22.

Li, Z. Wang, B. Wang, F. Wang, S. & Fei, W. 1984. *The Classification, Nomenclature and Identification of Volcanic Rocks*. Bulletin of the Institute of Geology, Chinese Academy of Geological Sciences. No. 8. (in Chinese)

Novikov, L.A. & Slabodskay, R.M. 2010. Mechanism of formation of diatreme. *International Geology Review*, 21, 1131–1132.

Schmid, R. 1981. Descriptive nomenclature and classification of pyroclastic deposits and fragment recommendations of the IUGS Subcommission on the systematic of igneous rocks. *Geology.* **9**, 41–43.

Sewell, R. J. Campbell, S.D.G. Fletcher, C. J. N. Lai, K. W. & Kirk, P. A. 2000. *The Pre-Quaternary Geology of Hong Kong.* Geotechnical Engineering Office, Civil Engineering Department.

Sewell, R.J. 2015. Guidelines on the description of rocks of the Tuen Mun Formation. *One day Seminar on Ground Investigation and Ground Characterization for Civil Engineering Projects*. Association of Geotechnical and Geoenviromental Specialists (HK). http://www.ags-hk.org/notes/20/_Guidelines_on_the_Description_and Classification_of_Rocks_of_the_Tuen Mun Formation_Sewell. pdf

So, K.W.F. & Sewell, R. J. 2017. *Guidelines on the description and classification of rocks of the Tuen Mun Formation in the Tuen Mun Valley, Northwestern New Territories*. GEO Report No. 327.

Sewell, R.J., So, K.W., Tang, D.L.K. & Carter, A. 2017. Unravelling an allochthonous subaqueously deposited volcanic-epiclastic to subaerial andesitic lava assemblage in Hong Kong: age, stratigraphy and provenance studies of the Middle Jurassic Tuen Mun Formation. *Journal of the Geological Society, London,* 174, 913–928

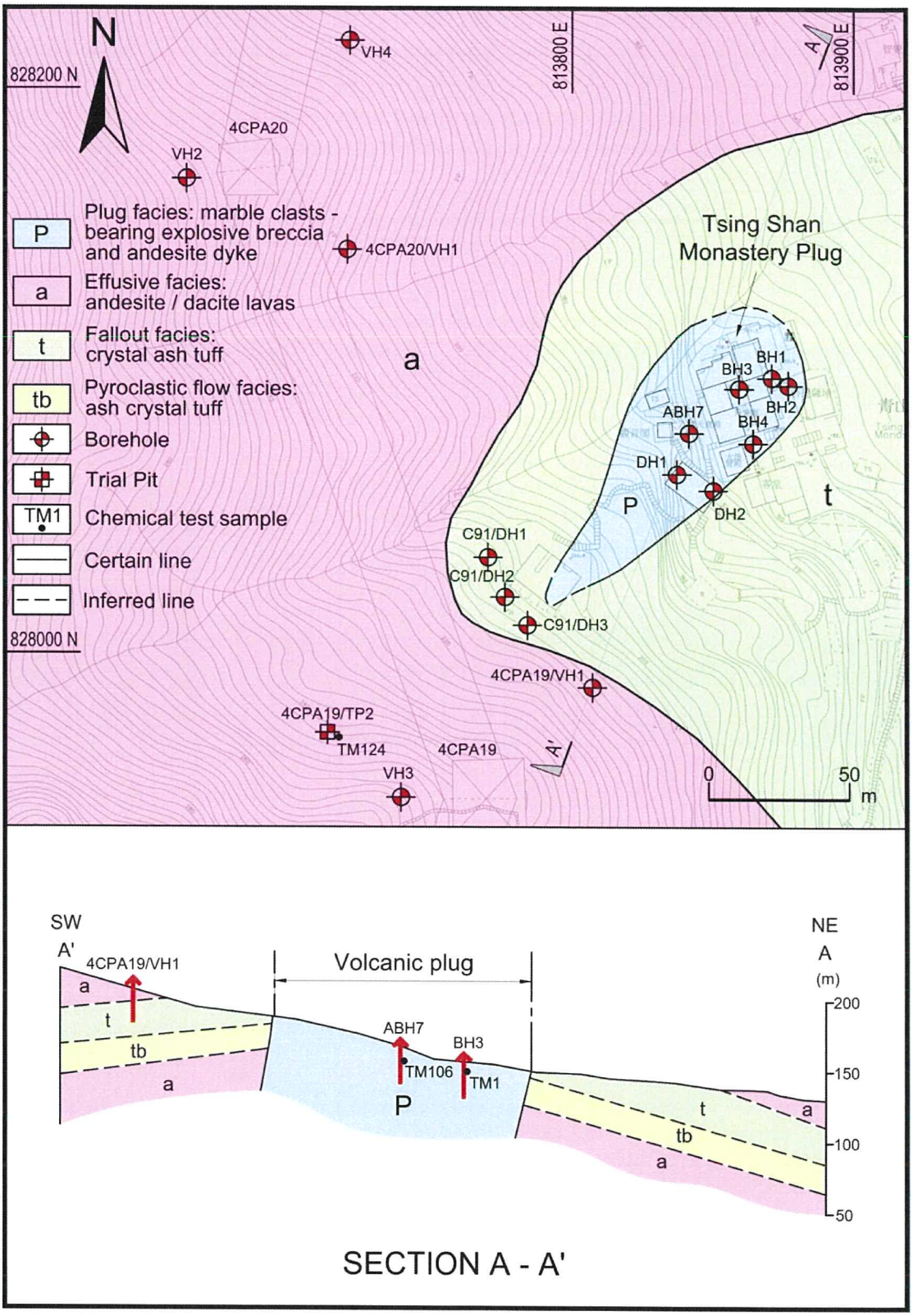

Figure 5. Geological Map and Section of Tsing Shan Monastery Plug. It is composed of explosive breccias and andesite dykes. The plug is associated with multiple eruption forming a stratovolcano

Figure 6. Dark Green Andesite Dyke Intrudes Explosive Breccia in the Outcrop of Tsing Shan Monastery Plug. The clasts consist of marble, sandstone and lava fragments, which are cemented by andesite

Figure 7. Drillhole BH3 shows Tsing Shan Monastery Plug. The dark green basaltic trachyandesite (chemical sample TM1 & TM104) intrudes the explosive breccia forming reaction rims. Lithic clasts consist of marble, sandstone and lava fragments, cemented by andesite

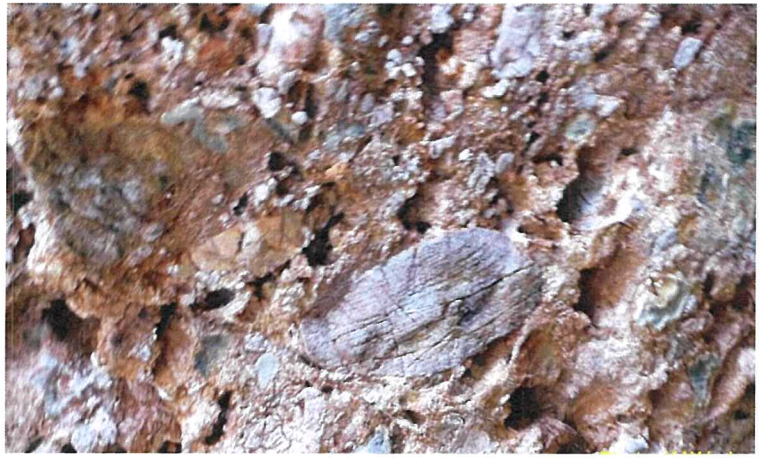

Figure 8. Explosive Breccia in the Tsing Shan Monastery Plug. All clasts are cemented by andesite/dacite

Figure 9. Reaction Rim Occurs Between the Marble Clast and Basaltic Andesite Producing Garnet and Epidote

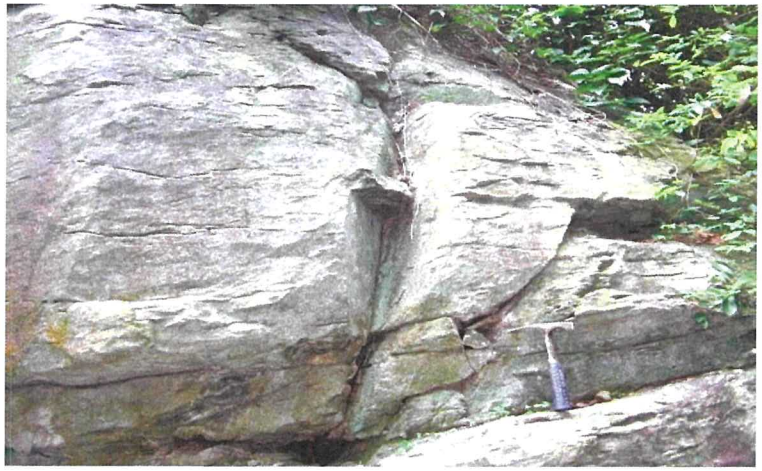

Figure 10. Ash Crystal Tuff of Fallout Deposits with Gentle Dipping Surrounding the Tsing Shan

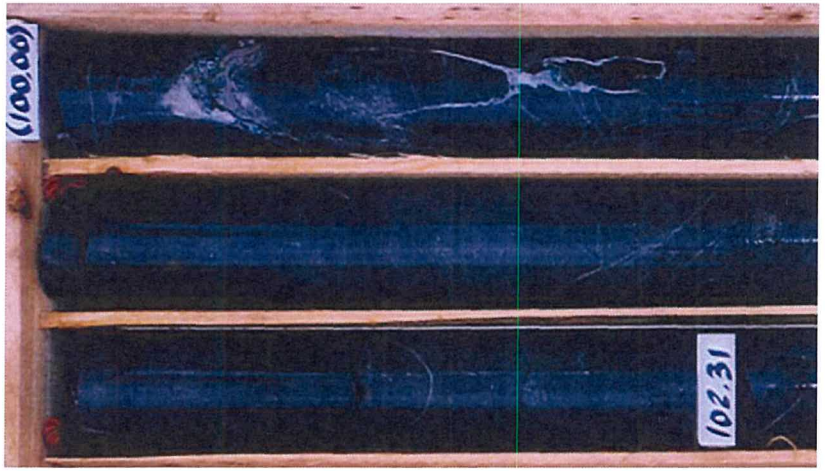

Figure 11. The Rock Sample is Andesite of Effusion Facies at Tuen Mun Seawater Service Reservoir (Drillhole S13)

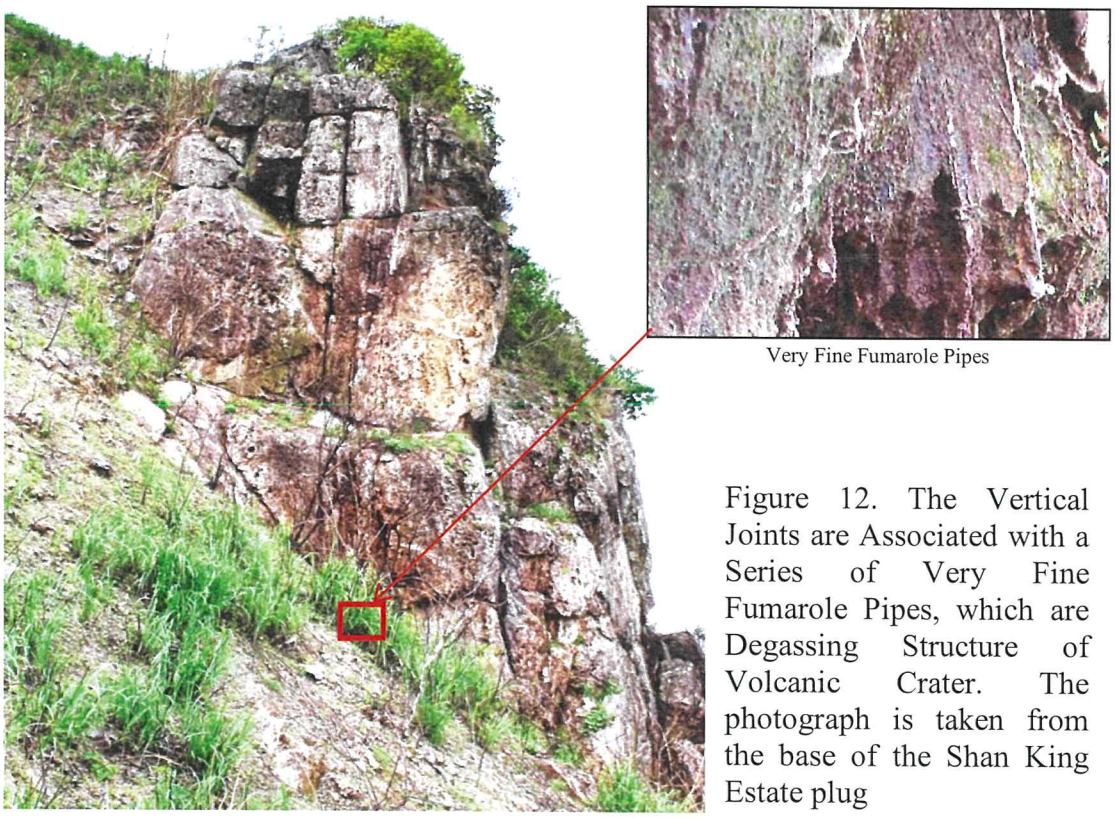

Figure 12. The Vertical Joints are Associated with a Series of Very Fine Fumarole Pipes, which are Degassing Structure of Volcanic Crater. The photograph is taken from the base of the Shan King Estate plug

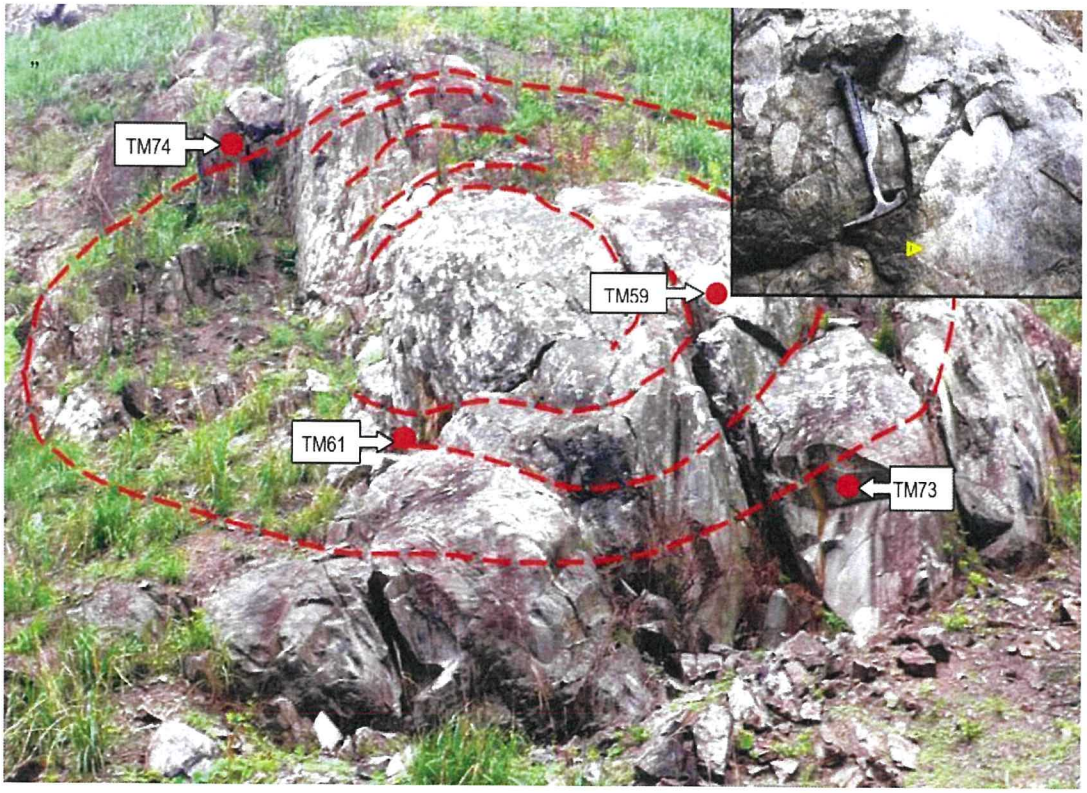

Figure 13. Photograph in the upper right corner is extracted from the Fig. A17 of GEO Report No. 327, in which the rock is named as Tuffaceous conglomerate. Chemical analysis confirmed the rock shown is tuff clasts-bearing andesite. It forms a parasitic plug with concentric circular joint pattern (red line). The results showed TM61 and TM73 are andesite, TM74 is dacite and TM59 is crystal tuff. Fig. 13 and Fig. A17 are at the same location (8143600 N828640)

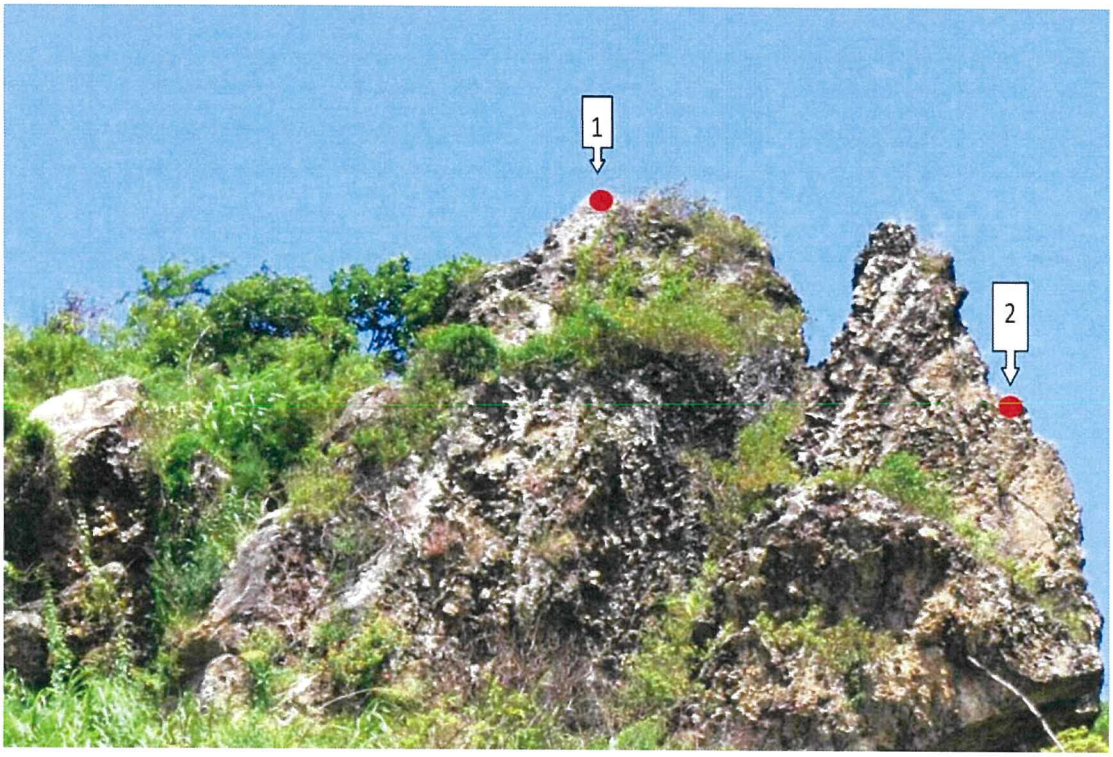

Figure 14. Volcanic Plug of South Por Lo Shan Consists of Multiple Eruptive Andesite/Dacite Dykes and Explosive Breccias

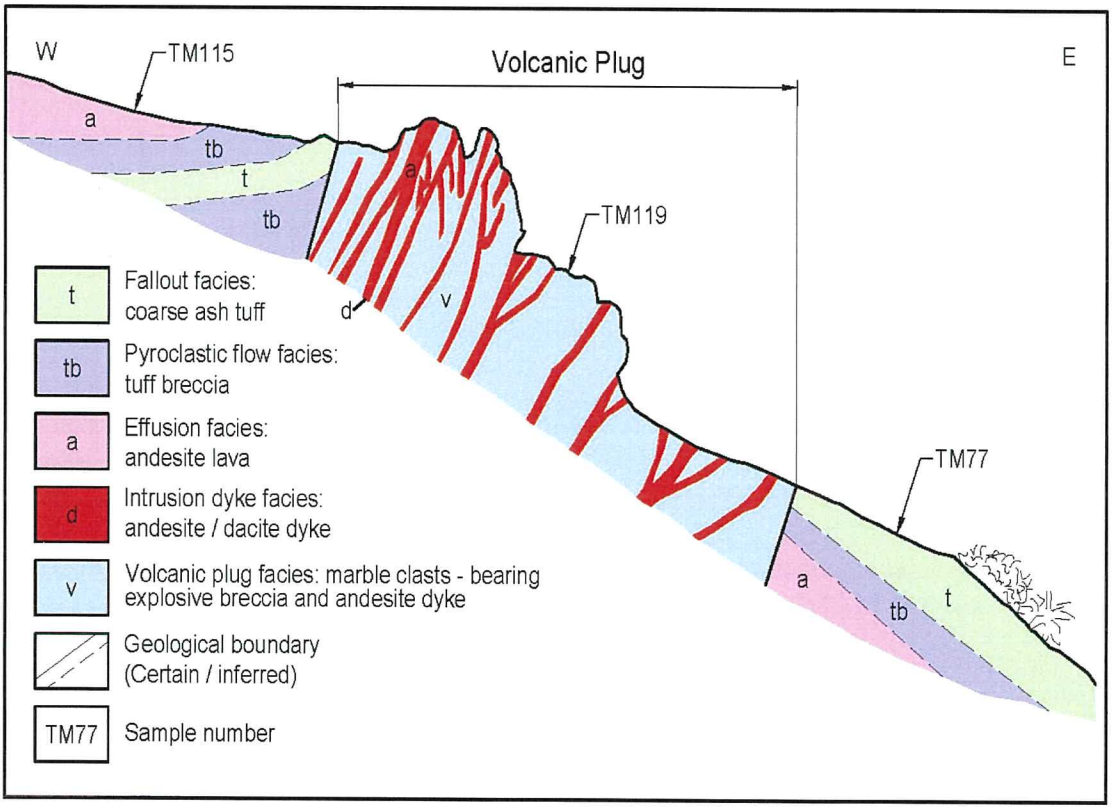

Figure 15. Cross-Section of Volcanic Plug of South Por Lo Shan. The plug consists of multiple eruptive andesite/dacite dykes and explosive breccias

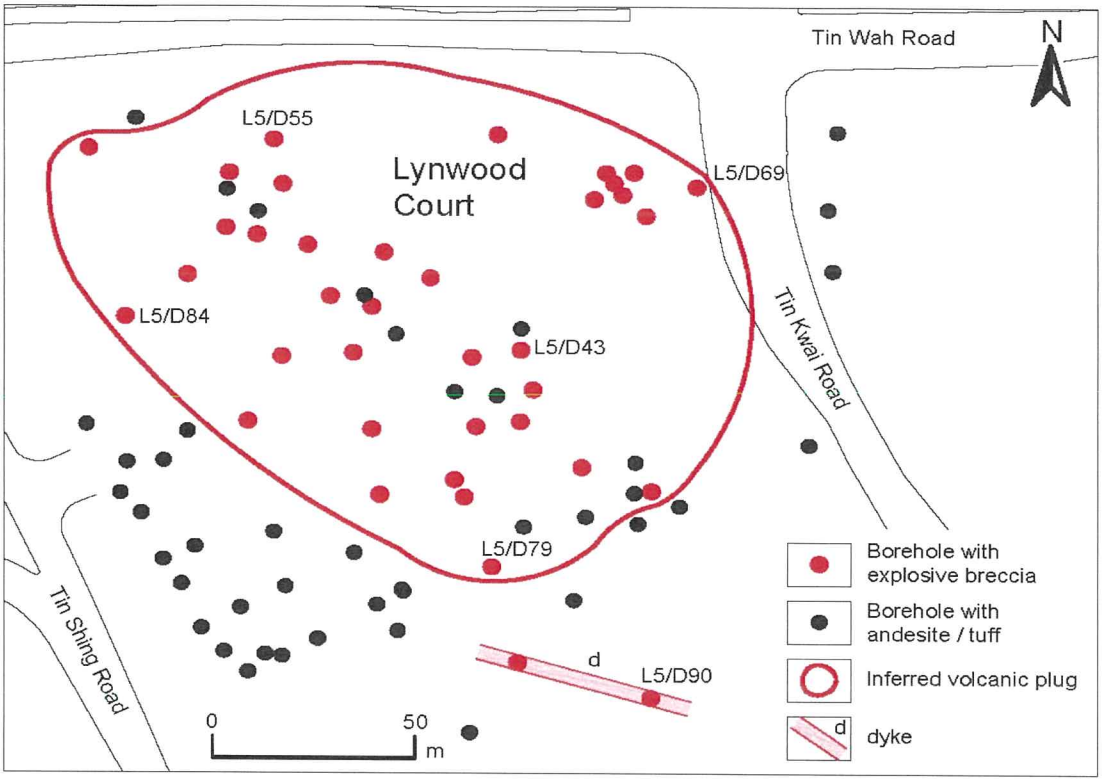

Figure 16. Inferred Volcanic Plug Plotted by Drillholes with Explosive Breccias (red) at Tin Shui Wai Area

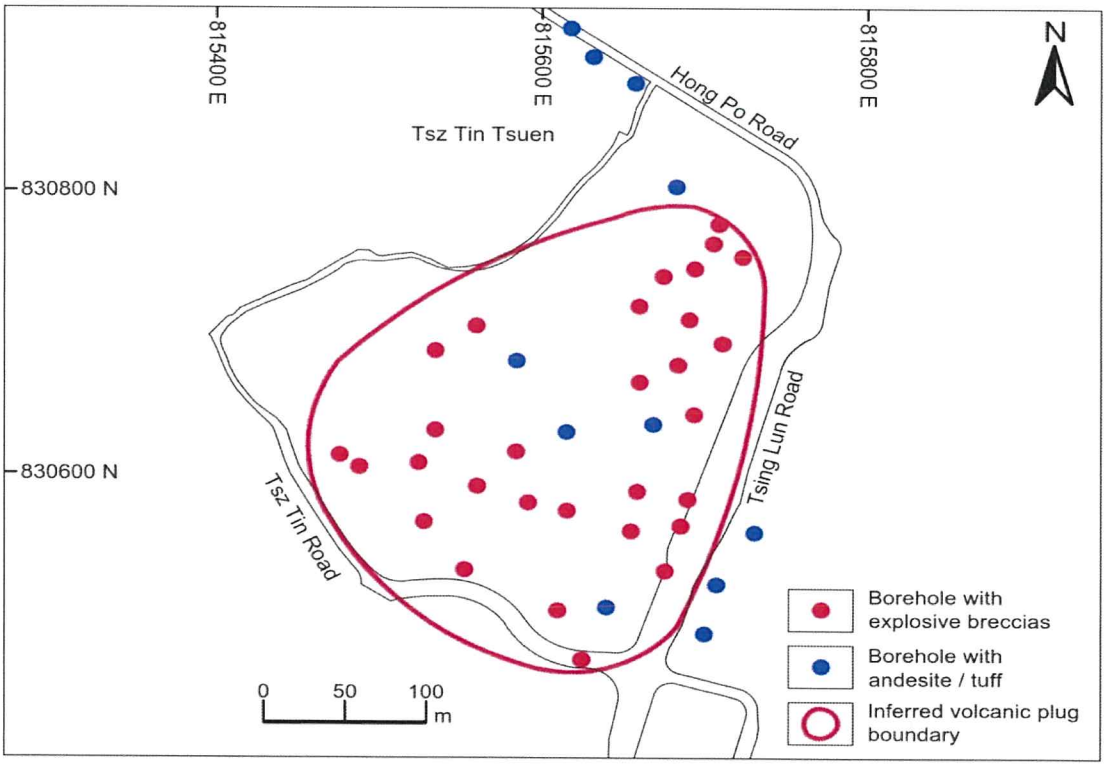

Figure 17. Inferred Volcanic Plug Plotted by Drillholes with Explosive Breccias (red), Surrounded by Drillholes with Andesite/Dacite or Tuff (black) at Tsz Tin Tsuen Area

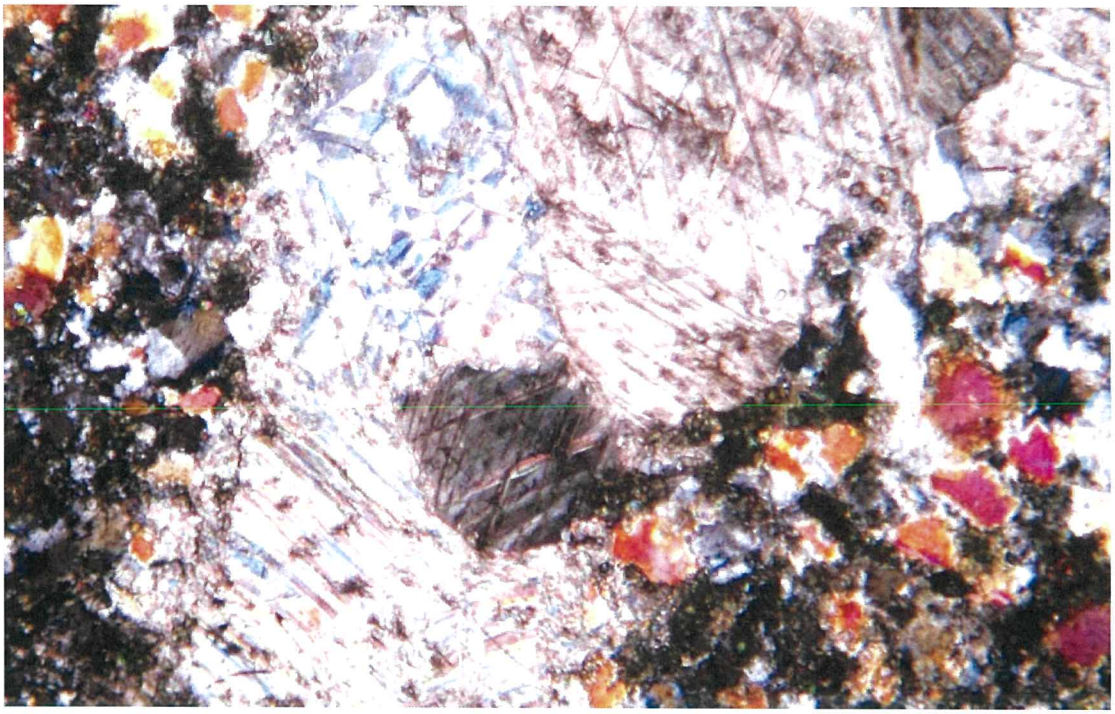

Figure 18. Photomicrograph of Explosive Breccia. The calcite is crushed to bits by intense explosion of volcanic activity, and cemented by plagioclase and hornblende. Chemical test result showed the cement material is dacite (TM136)

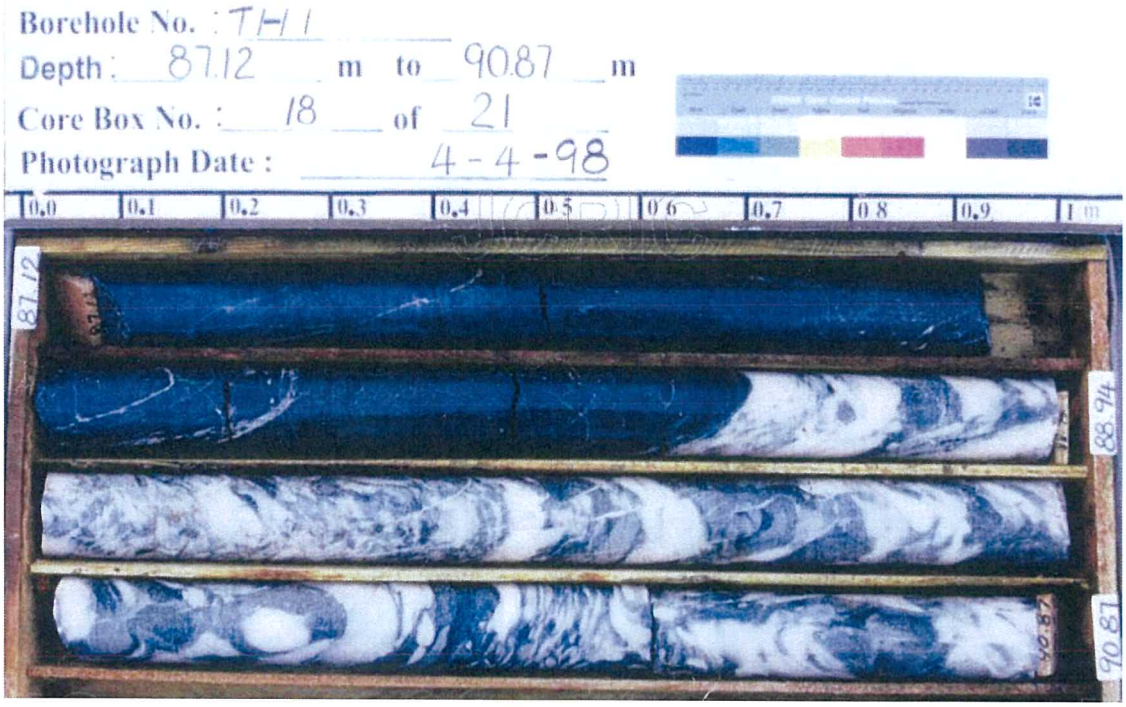

Figure 19. Drillhole TH1 Showing Evidence of Explosive Breccia & Andesite. Compared with chemical analysis data of the same area, the drill cores from 87.1 to 88.6 m are probably andesite, from 88.6 to 90.8 m probably marble clasts-bearing explosive breccias, which are crushed by intense explosion of volcanic activity. (Drillhole No. 29625/TH1)

Classifying Failure Modes Of Hong Kong Rocks Under Uniaxial Compression Loading Using High Speed Imaging Technique

Wong Ngai Yuen Louis[1], Guo Tianyang Steve[2], Yip Tin Man Lydia[3]
[1] Associate Professor, Director of MSc in Applied Geosciences and PgD in Earth Sciences
[2] PhD student
[3] formerly FYP student
Department of Earth Sciences, the University of Hong Kong

Abstract: Uniaxial compression test is one of the most popular laboratory tests carried out in Hong Kong to determine the mechanical properties of rocks. Apart from the strength and deformation modulus values, the failure modes are also normally recorded. In this study, twenty local cylindrical granite and tuff specimens are tested under uniaxial compression. With the aid of a high-speed camera, it becomes possible for us to observe the cracking process in detail, which provide important clues on the relationship between failure mode and uniaxial compressive strength of the test specimens. The ranges of the UCS for the tested 11 granite specimens and 9 tuff specimens are 27.02-225.22 MPa (mean = 136.32 MPa) and 85.06 - 247.63 MPa (mean = 154.54 MPa) respectively. Regarding the cracking process, the development of zig-zag cracks is common in granite, while the development of a dominant inclined shear crack is common in tuff. The failure mode of granite is mainly axial splitting, while the failure modes of tuff include shearing along a single plane, along a wedge, and dendritic shearing. Multiple fracturing mode occurs in both granite and tuff.

1 INTRODUCTION

Studies on rock mechanical properties are of paramount importance for rock engineering practices, including foundation support, slope and underground construction stability. Uniaxial compressive strength (UCS) test is one of the most popular techniques to quantitatively study the mechanical properties of rocks such as uniaxial compression strength, deformation modulus as well as failure modes. In the UCS test, a cylindrical rock specimen should be prepared and loaded to failure on a uniaxial compression test machine. The maximum load recorded by the machine is often regarded as the failure load, which would further be used to calculate the UCS. However, the UCS varies even for specimens with the same lithology. The influencing factors on UCS of rocks include specimen geometry, mineralogy, crystal anisotropy, micro-parameters such as grain size, grain shape, and most importantly micro-cracks (Waversik and Faurhurst, 1969; Brady, 1970; Hudson, et al., 1972; Hudson and Harrison, 1997; Szwedzicki and Shamu, 1999; Gupta and Rao, 2000; Wong et al., 2006; Basu et al., 2009; Basu et al., 2013).

It has long been recognized by many scholars that rock failure is caused by the initiation, propagation and coalescence of pre-existing micro-cracks in rock. During the UCS test, the

arrangement of crystal lattice in the rock specimen will be disturbed (Davis et al. 1942). New cracks initiate at the tips of pre-existing micro-cracks once the critical stress is reached (Szwedzicki, 2007). In rock mechanics, cracks are normally classified into two types, namely tensile crack and shear crack. The tensile cracks generally develop in an orientation parallel to the maximum principal stress, while the shear cracks develop in an inclined orientation to the maximum principal stress (Wong and Einstein, 2009a). Some scholars have investigated the crack types and coalescence patterns using rock specimens containing pre-existing flaws. It is found that tensile cracks, shear cracks, or a mix of tensile and shear cracks first initiate at the two tips of pre-existing flaws (Reyes, et al., 1991; Tang and Kou, 1998; Bobet and Einstein, 1998; Szwedzicki, 2007, Wong and Einstein, 2009a). The initiated cracks firstly propagate stably for a while, then unstably after reaching a critical length. In the meanwhile, a number of secondary cracks initiate at the periphery of the primary cracks (Zhang and Zhao, 2013). During this process, some of them may meet each other, which is called crack coalescence. Collinear rocks link directly together, and non-collinear cracks can connect as an X-shaped band. (Reyes, et al., 1991; Chen, et al., 1995; Tang and Kou, 1998). Finally, the rocks fail when the crack coalescence is highly developed. It can be seen that crack initiation, propagation and coalescence will determine the failure modes of rock specimens under uniaxial compression. Therefore, studying the failure modes of rock specimens in UCS tests will enhance our understanding of rock failure mechanism as well as the variance of UCS.

The microstructures of natural rock are so complex that no mathematical or numerical model can fully interpret the failure mechanism. Bieniawski (1984) stated that the physical modeling is the optimal approach to study failure modes of rock specimens under uniaxial compression. In recent years, the failure modes of rock specimens in UCS tests are still actively researched (Hudyma et al., 2004; Szwedzicki, 2007; Basu et al. 2009, 2013). See Table 1. Hudyma et al. (2004) investigated the failure modes of cylindrical and cubic plaster models as well as tuff specimens under uniaxial compression. In this research, the failure modes of cylindrical plaster specimens can be categorized into four varieties, namely spalling, axial splitting, shear failure and web failure. Szwedzicki (2007) stated that five distinct failure modes can be identified in hard and brittle cylindrical rock in UCS test: simple extension, multiple extension, multiple fracturing, multiple shear, and simple shear (Fig. 1). Basu et al. (2009) studied failure modes of granitic specimens from southeastern Brazil under uniaxial compression. For specimens with different weathering grades, three failure modes were observed including axial splitting, single shear plane failure and failure along two shear planes. Afterwards, Basu et al. (2013) further conducted UCS tests on three rock types, granite, schist, and sandstone from India to explore the relationship between failure modes and UCS. More specific failure modes are summarized, namely axial splitting, shearing along a single plane, double shear, multiple fracturing, along foliation and Y-shaped failure (Fig. 2).

Table 1 A review of failure modes observed in previous studies

Authors	Rock or rock-like material type	Failure modes
Hudyma et al., (2004)	Plaster specimen	Spalling, axial splitting, shear failure and web failure
Szwedzicki (2007)	Hard and brittle rock	Simple extension, multiple extension, multiple fracturing, multiple shear, and simple shear

Basu et al. (2009)	Granite	Axial splitting, single shear plane failure and failure along two shear planes
Basu et al. (2013)	Granite, schist, and sandstone	Axial splitting, shearing along a single plane, double shear, multiple fracturing, along foliation and Y-shaped failure

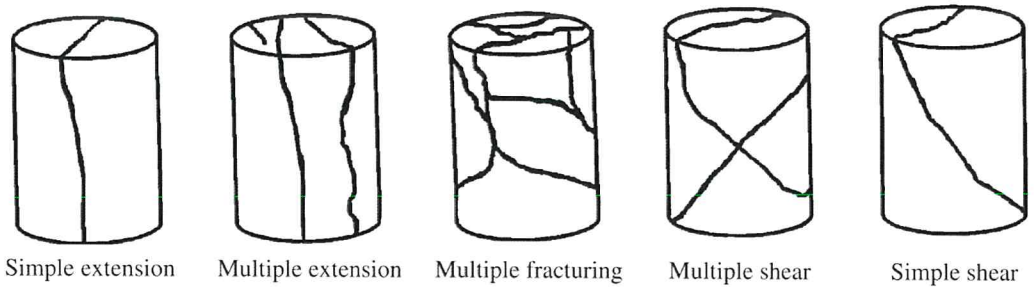

Fig.1 Schematic diagrams of failure modes in hard and brittle rock (Szwedzicki 2007)

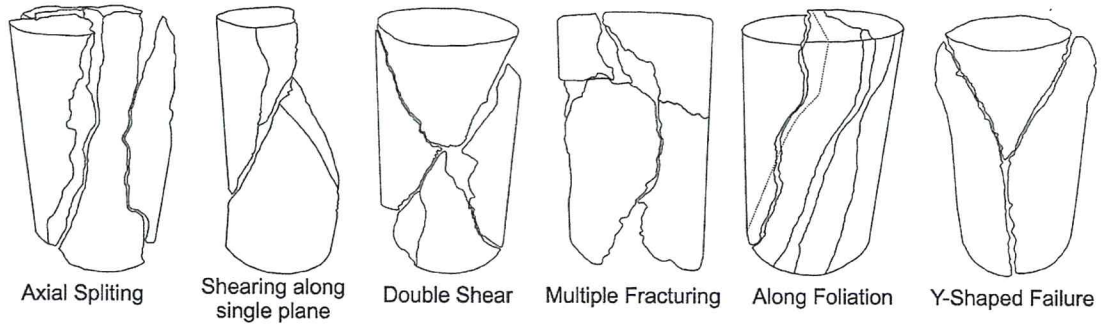

Fig.2 Schematic representation of different failure modes under uniaxial compression (Basu et al. 2013)

In view of previous studies, rocks are so different in microstructures that distinct failure modes are observed, even when specimens of identical lithology are tested. Szwedziki (2007) and Basu et al. (2013) pointed out that a large range of UCS and various failure modes result from microstructural differences particularly in the form of microcracks. Therefore, the cracking processes of tested specimens need to be analyzed in detail to explain the relationship between failure modes and uniaxial compressive strength in UCS test. In this study, cracking processes and failure modes of granite and tuff specimens are identified with the help of a high-speed camera. The relationships between failure modes and UCS for the two rock types are also studied.

2 SPECIMEN PREPARATION AND TESTING APPARATUS

2.1 Specimen preparation

Granite and tuff rock samples cored from Hong Kong are fabricated into standard cylindrical specimens in accordance with the ASTM standard (ASTM D4543-08, 2008). It should be noted that two ends of the specimens shall be cut parallel to each other and at right angles to the longitudinal axis, which can reduce the end effects. A rock specimen polishing machine is used to grind the ends. The dimensions of the specimens are listed in Table 2. The length-to-diameter ratio of each specimen ranges from 2.45 to 2.17, which meets the required range of 2.0 to 2.5 in ASTM standard (ASTM D7012-14, 2014).

Table 2 Dimensions of prepared specimens

No.	Specimen no.	Lithology	Length(L)/mm	Diameter(D)/mm	L/D
1	2016090801	Granite	194.04	83.44	2.33
2	2016090802	Granite	182.29	83.18	2.19
3	2016090803	Granite	190.03	83.36	2.28
4	2016090805	Granite	196.10	83.38	2.35
5	2016092901	Tuff	187.95	79.48	2.36
6	2016092902	Tuff	194.82	79.49	2.45
7	2016092903	Tuff	189.83	79.38	2.39
8	2016092904	Tuff	190.46	79.59	2.39
9	2016092905	Tuff	186.49	79.72	2.34
10	2016111001	Granite	188.86	82.85	2.28
11	2016111002	Granite	189.71	83.06	2.28
12	2016111003	Granite	188.08	83.5	2.25
13	2016122901	Granite	182.45	83.41	2.19
14	2017033001	Granite	194.48	83.19	2.34
15	2017033002	Tuff	198.93	83.58	2.38
16	2017033004	Tuff	189.83	79.38	2.39
17	2017050401	Tuff	177.28	79.5	2.23
18	2017050402	Tuff	181.39	83.58	2.17
19	20170704	Granite	181.16	83.33	2.17
20	20170721	Granite	187.27	83.22	2.25

2.2 Testing system

Experiments are conducted on a hydraulic servo-controlled MTS815 testing system with the loading capacity of 2000kN. A spherically seated and a plain rigid steel platen are used to transmit the axial load to the ends of the specimen. The specimens are continuously loaded until failure at a loading rate of 0.03mm/s. Meanwhile, the deformation and the load applied on the specimen are automatically logged every 0.01 s. A recording system which consists of a high-speed camera (Phantom V711), a camcorder (Sony HDR-PJ675) and two LED lights, is used to capture videos of the initial cracking to final failure processes.

2.3 High-speed camera

In UCS tests on brittle rocks, failure of the specimens is often too fast to be captured by an ordinary camera, therefore, a Phantom V711 high-speed camera is used to record the failure moment. Two LED lights are placed on two sides to provide sufficient illumination. Because of limited storage memory (32 Gb), the resolution of the high-speed footage will decrease with the increase of frame rate. In order to balance these two factors, the resolution and frame rate have to be constantly adjusted to ensure a high-quality footage of failure process for the specimens. The detailed operational procedures of the high-speed camera are provided in an earlier reference (Wong and Einstein, 2009b).

3 RESULTS

3.1 Mechanical properties and failure modes

In the present study, a total of 20 UCS tests have been conducted. The mechanical parameters and failure modes of each specimen are obtained and listed in Table 3. In the tests, the maximum load recorded by the system is considered as failure load, which can be used to determine the UCS of the specimens. The Young's modulus is defined as the average modulus determined from the slope of the linear part of the stress-strain curve. The failure strain is calculated through the displacement corresponding to the failure load. The ASTM standard suggests that the selected stress rate or strain rate shall produce failure of a cohort test specimen in compression, in a test time between 2 and 15 min (ASTM D7012-14, 2014). The failure times listed here are all within this time range, which satisfy the loading rate requirement.

Table 3 The mechanical properties and failure modes of specimens in UCS tests

Specimen No.	Lithology	UCS /MPa	Young's modulus /GPa	Failure strain /%	Failure time /s	Failure mode
2016090801	Granite	117.67	17.5	0.88	563.5	Axial splitting
2016090802	Granite	85.95	19.5	0.58	346.3	Axial splitting
2016090803	Granite	138.43	19.3	0.93	582.9	Axial splitting
2016090805	Granite	27.02	11.5	0.31	202.5	Axial splitting
2016092901	Tuff	123.09	24.3	0.95	585.8	Shearing along a wedge
2016092902	Tuff	125.18	24.3	0.66	421.1	Shearing along a single plane
2016092903	Tuff	110.8	23.6	0.58	365.4	Shearing along a single plane
2016092904	Tuff	165.01	22.8	0.84	528.2	Multiple fracturing
2016092905	Tuff	85.06	23.2	0.49	298.2	Dendritic shearing
2016111001	Granite	187.23	26.6	0.81	512.1	Multiple fracturing
2016111002	Granite	62.14	22.3	0.39	233.1	Shearing along a single plane
2016111003	Granite	169.02	26.6	0.81	496.8	Axial splitting
2016122901	Granite	225.22	25.6	1.03	625.7	Dendritic shearing
2017033001	Granite	111.95	19.5	0.70	446.7	Multiple fracturing
2017033002	Tuff	179.36	26.2	0.79	519.9	Axial splitting
2017033004	Tuff	247.63	28.9	1.08	678.7	Axial splitting
2017050401	Tuff	165.99	23.3	0.84	482.7	Axial splitting
2017050402	Tuff	165.95	24.1	0.77	467.3	Multiple fracturing
20170704	Granite	190.48	26.5	0.89	535.0	Axial splitting
20170721	Granite	184.46	24.7	0.82	507.54	Multiple fracturing

According to the results, the ranges of the UCS for the 11 tested granite specimens and 9 tuff specimens are found to be from 27.02 to 225.22 MPa and 85.06 to 247.63 MPa, respectively. The average UCS of the tested granite and tuff specimens are 136.32 MPa and 154.54 MPa, respectively. The UCS values of the tested specimens cover relatively wide range for both rock types. The ranges of Young's modulus of the tested granite and tuff specimen are

from 11.5 to 26.6 GPa and from 22.8 to 28.9 GPa, respectively. The average Young's modulus of the tested granite and tuff specimens are 21.8 GPa and 24.5 GPa, respectively.

In previous studies (Hudyma et al., 2004; Szwedzicki, 2007; Basu et al., 2009; Basu et al., 2013), failure modes of rock specimens are generally determined by examining the failed specimens after the completion of UCS tests. However, with the aid of a high-speed camera, the failure modes of the tested rock specimens can be easily identified through high-speed footages. The failure modes observed in all the tested specimens are classified into five categories (i.e., axial splitting, shearing along a wedge, shearing along a single plane, dendritic shearing, multiple fracturing). Apart from some common failure modes, several new failure modes such as shearing along a wedge, dendritic shearing are uniquely found in this study. The representative diagrams of the five failure modes are presented in Fig.3 .

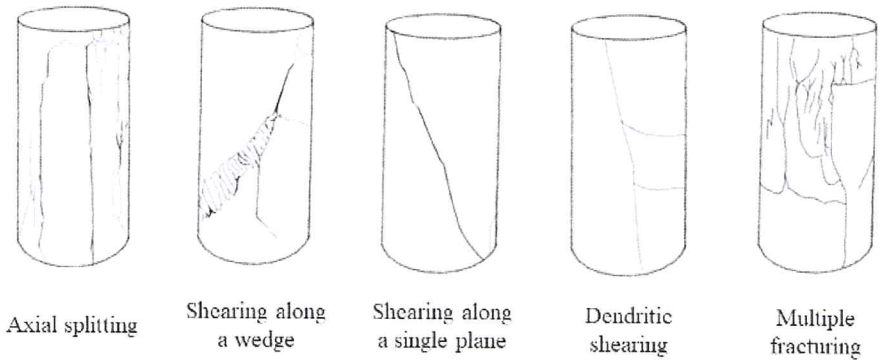

Fig.3 Representative diagrams of failure modes observed in the present UCS tests

The relationships between UCS and failure modes are also examined in this study (Fig. 4). Three failure modes including axial splitting, multiple fracturing and shearing along a single plane occur in both granite and tuff specimens.

As shown in Fig.4 (a), axial splitting is the most common mode of failure of the granite specimens. The UCS values of the granite specimens failed in axial splitting mode cover a wide range from 27.02 to 190.48 MPa, which indicate that axial splitting mode can happen in granite specimens with different strength. The UCS of granite specimens failed in multiple fracturing mode are generally higher than those failed in shearing along a single plane mode, which agree well with the experimental observations in Basu et al. (2013).

As seen in Fig. 4(b), the failure modes of the tuff specimens include axial splitting, shearing along a single plane, along a wedge, and dendritic shearing. There are no dominant failure modes for the tuff specimens. The UCS of tuff specimens failed in shearing modes (shearing along a single plane, along a wedge and dendritic shearing) are generally lower than those failed in other modes such as axial splitting and multiple fracturing.

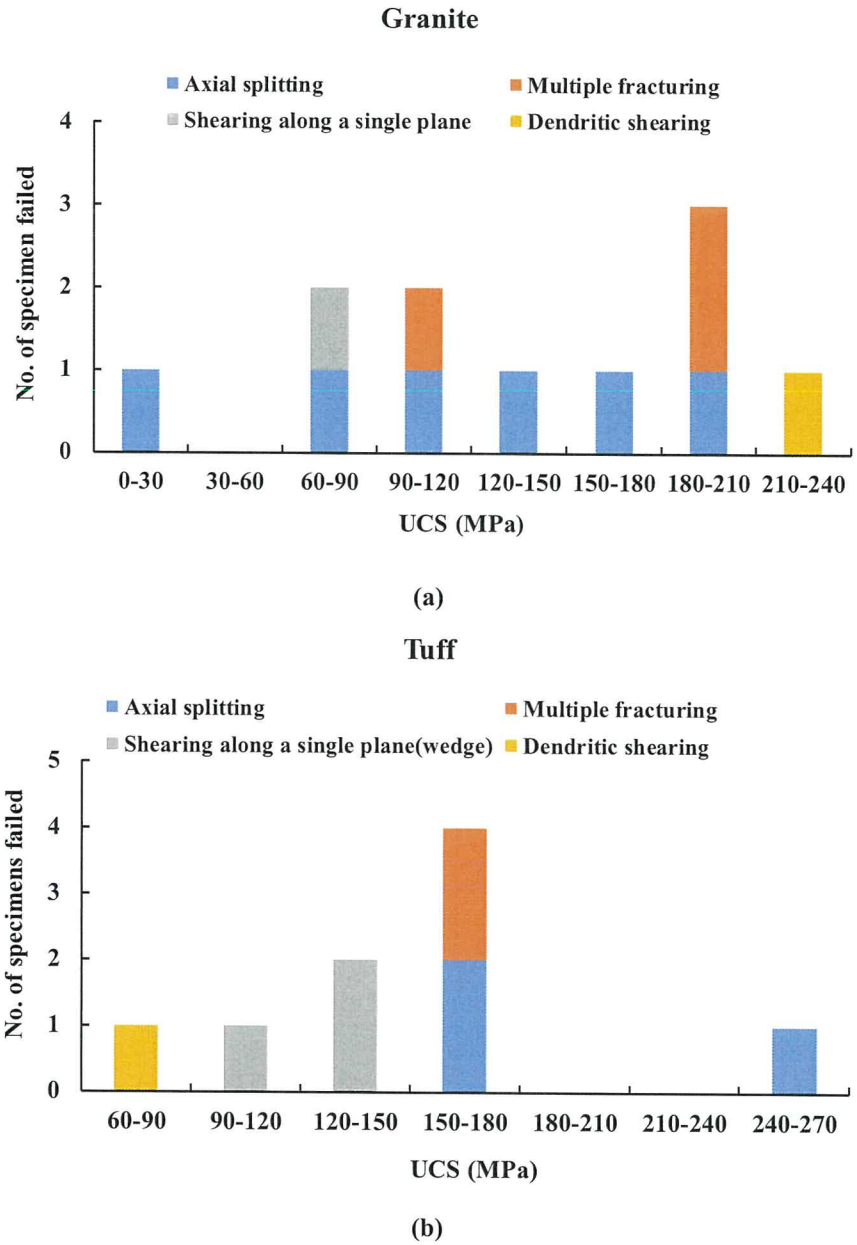

Fig.4 Bar charts showing numbers of specimens failed in different ranges of UCS in relation to failure modes in **a** granite, **b** tuff

3.2 Cracking processes

Detailed analyses on cracking processes will contribute to a better understanding of various failure modes. Each failure mode is illustrated by a representative specimen below. All the photos are captured from the high-speed footages. For each specimen, the moment when the first photo is taken is counted as time zero. For specimens with abrupt failure, the first photo is chosen to be the first crack initiation. For specimens with progressive failure, the entire failure duration could exceed the maximum time (3.16 s) the high-speed camera is able to record. In this case, the first photo is the first frame of the high-speed footage. The time lapses of the subsequent photos are calculated based on the frame rate and frame numbers.

Axial splitting

The lithology of specimen numbered 2016090801 is slightly chloritized coarse-grained granite. There are not any pre-existing observable flaws on the surface. The UCS of the granite specimen is 117.67 MPa.

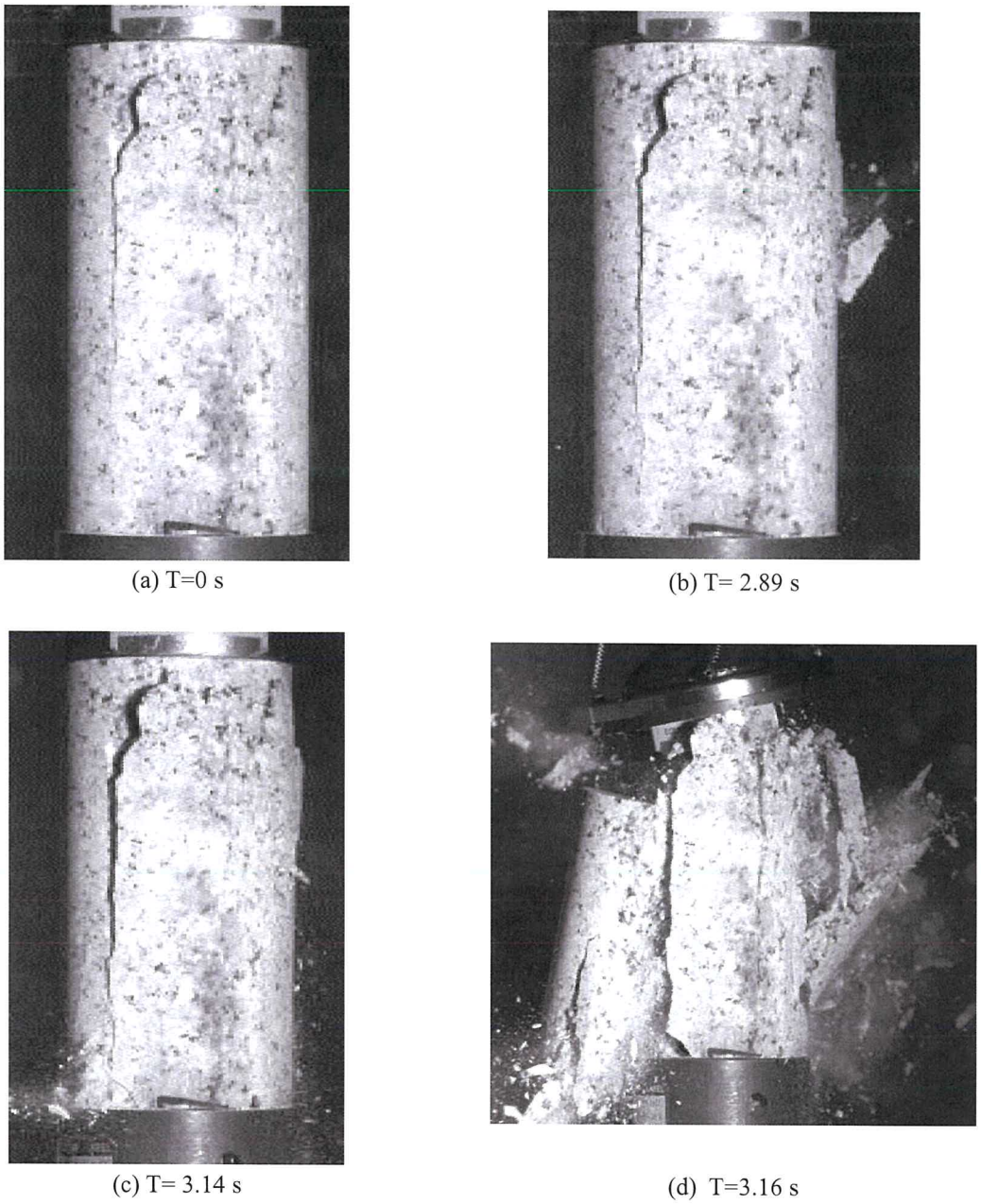

(a) T=0 s (b) T= 2.89 s

(c) T= 3.14 s (d) T=3.16 s

Fig. 5 The cracking processes of granite specimen 2016090801. Frame rate=2000 fps (frames per second). Resolution= 1280×800

The failure mode of specimen 2016090801 is axial splitting. It can be observed from Fig. 5 (a) that one major vertical tensile crack, several minor tensile cracks and one sub-horizontal crack firstly appear on the specimen. Most of the cracks are vertical, which are 0-5° to the maximum principal stress. Afterwards, some rock pieces continue spalling off from the upper right of the specimen. As loading goes on, more cracks initiate at the bottom left corner, which are mostly tensile in nature (Fig. 5 (b)). Finally, the specimen is fragmented into multiple parts

by the fully developed cracks, which are characterized as vertical cracks connecting the two ends of the specimen. Since the first crack initiated before the time when the first frame of the high-speed footage is recorded, it takes more than 3.16 s progressing from crack initiation to final failure for the specimen.

Shearing along a wedge

The lithology of specimen numbered 2016092901 is moderately decomposed, coarse ash crystal tuff. The UCS of the tuff specimen is 123.09 MPa.

The failure mode of specimen 2016092901 is shearing along a wedge. For this specimen, beddings aligned at an inclined angle of about 30 ° from vertical. The beddings provide weakness planes for cracks to preferentially develop. During the loading process, an inclined crack firstly initiates on the right side of the specimen (Fig. 6 (a)). When it further propagates towards the center, two tensile cracks which are perpendicular to the existing crack start to develop. Some rock pieces spall from the initial cracking location (Fig. 6 (b)). Afterwards, many sub-parallel slightly inclined tensile cracks form at the lower left of the specimen. They initiate from the middle to the lower left, which are connected by secondary cracks initiated at the periphery of the primary tensile cracks (Fig. 6 (c)). Finally, a group of Y-shaped conjugate cracks along a shear band are formed (Fig. 6 (d)). The cracking process is so fast that it only takes 0.019 s progressing from crack initiation to final failure for the specimen.

After failure, a bulge in the Y-shaped cracks is found on the left edge. This is possibly due to the interconnection of the small cracks which disturb the coherence of the structure. Thus, it destroys the rock structure from inside to outside, leading to the failure of the rock specimen along a single shear band.

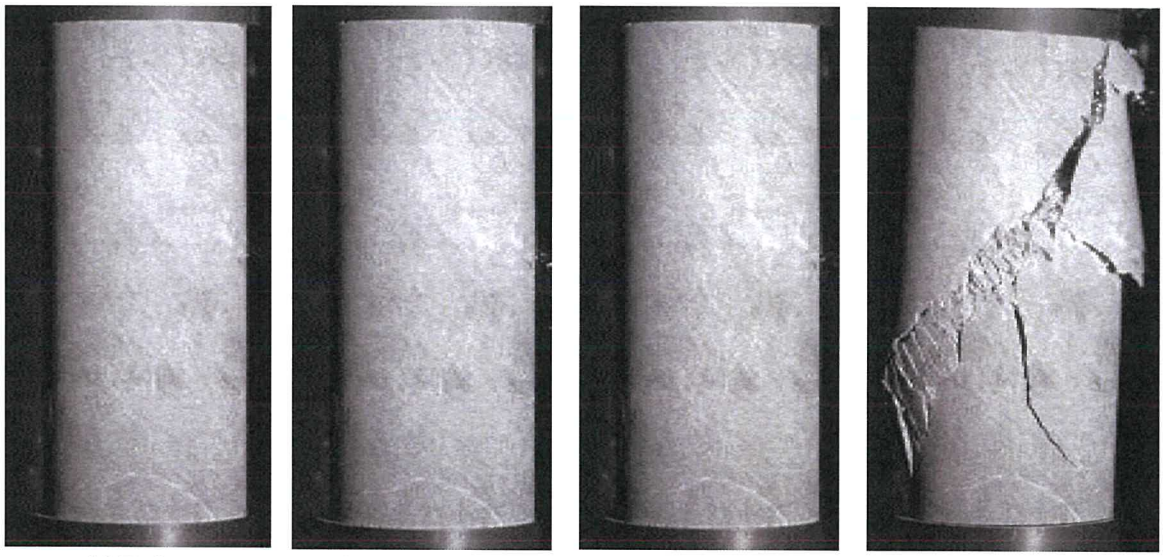

(a) T=0 s (b) T= 0.0024 s (c) T= 0.017 s (d) T=0.019 s

Fig.6 The cracking process of tuff specimen 2016092901. Frame rate=8000 fps. Resolution= 800×600.

Shear along a single plane

The lithology of specimen numbered 2016092902 is moderately decomposed, coarse ash crystal tuff. There are some pre-existing flaws observed on the specimen surface. The UCS of

the tuff specimen is 125.18 MPa.

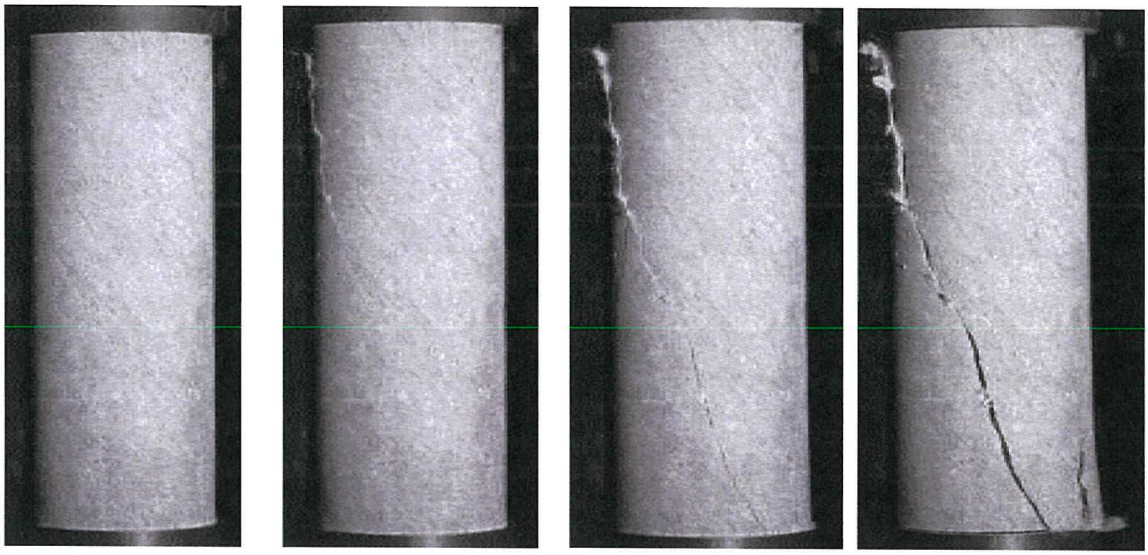

(a) T=0 s (b) T= 0.000077 s (c) T= 0.00023 s (d) T=0.00054 s

Fig. 7 The cracking processes of tuff specimen 2016092902. Frame rate=13000 fps. Resolution= 800×600.

For this specimen, rock failure is dominantly induced by a macroscopic shear crack. The failure mode can be therefore classified as shearing along a single plane. At the beginning of the cracking process, a large crack, which orientates generally parallel with the lineation of the rock specimen, initiates at the top left corner. As the lineation is orientated at an inclined angle about 40°, the shear crack is also moderately inclined. Afterwards, the crack extends very quickly all the way through the rock specimen towards the bottom right corner, leading to the final failure of the specimen. At last, another sub-vertical crack at the bottom right corner creates a separate piece of rock fragment, which later spalls off during rock failure. The entire cracking process occurs abruptly. It only takes 0.00054 s in total progressing from crack initiation to final failure for the specimen.

Dendritic shearing

The lithology of specimen numbered 2016092905 is moderately decomposed, coarse ash crystal tuff with distribution of striped white quartz veins. The UCS of the tuff specimen is 85.06 MPa.

The failure mode of specimen 2016092905 is dendritic shearing. Fig. 8 (a) shows that a steeply inclined crack firstly initiates from the bottom left of the specimen. Afterwards, two sub-horizontal cracks form an X-shaped pattern on the upper part of the rock. In the meanwhile, three inclined cracks initiate on the lower part of the rock (Fig. 8 (b)). Based on the image of the rock specimen before testing, the location of the pre-existing flaws coincides with that of the X-shaped crack pattern. Near the right end of the X-shaped pattern, a small opening of a vertical tensile crack is observed. The tensile crack then extends downwards and splits the lower rock specimen into two parts (Fig. 8 (c)). It takes 0.074 s progressing from crack initiation to final failure for the specimen. Since the high-speed camera can only capture the front face of the specimen, the other primary vertical crack initiated from the back is not visible

in the photos.

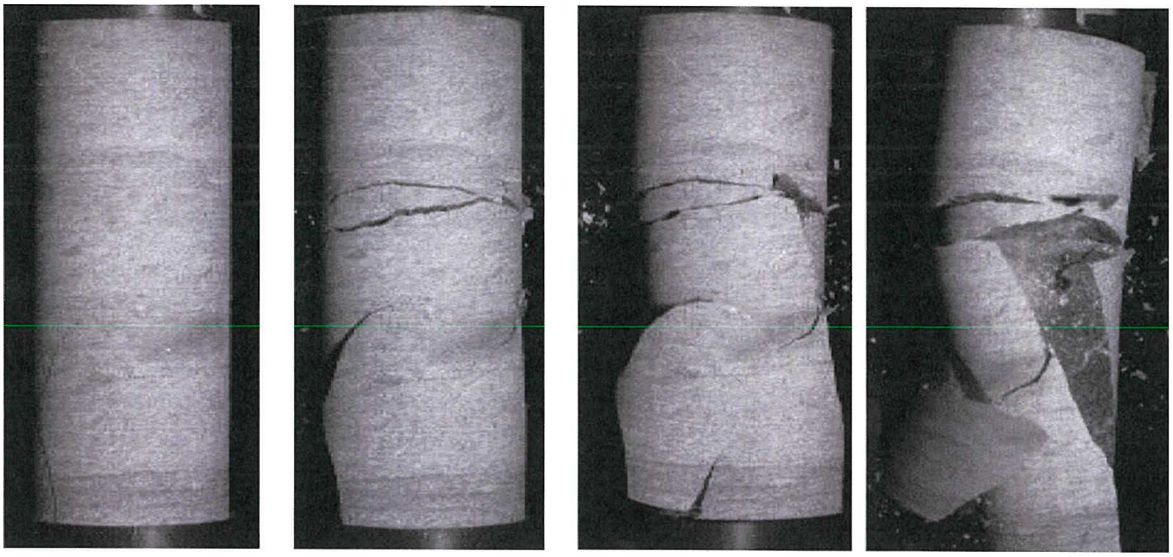

(a) T=0 s (b) T= 0.0047 s (c) T= 0.025 s (d) T=0.074 s

Fig. 8 The cracking processes of tuff specimen 2016092905. Frame rate=33000 fps. Resolution= 512×384.

Multiple fracturing

The lithology of specimen numbered 2016111001 is slightly decomposed, medium-grained granite. The UCS of the granite specimen is 117.67 MPa.

(a) T=0 s (b) T= 0.037 s

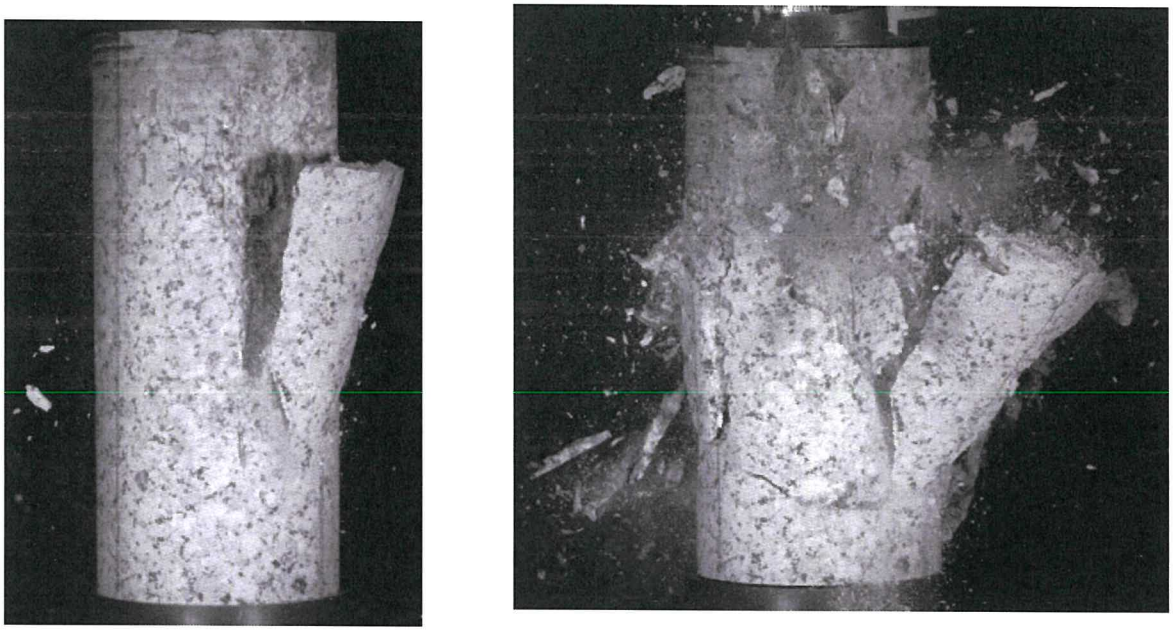

(c) T= 0.82 s (d) T=0.91 s

Fig. 9 The cracking processes of granite specimen 2016111001. Frame rate=33000 fps. Resolution= 512×384.

The failure mode of specimen 2016111001 belongs to multiple fracturing. A sub-horizontal crack firstly initiates at the top right corner of the specimen (Fig. 9 (a)). Basically, it is a shear crack, but some zig-zag flaws appear in its middle. Some rock pieces spall off from the zig-zag flaws. As more cracks initiate, rock bulges on the upper right side. Subsequently, a localized spalling occurs in the top half of the specimen with white powder ejecting around (Fig. 9 (b)). The loading continues as the specimen can sustain further increasing axial stress until another spalling event happens (Fig. 9 (c)). After the two spalling events, the specimen soon fails in the multiple fracturing mode at a relatively high stress (117.67 MPa) (Fig. 9 (d)). It takes 0.91 s progressing from crack initiation to final failure for the specimen.

In this section, cracking processes of five representative specimens corresponding to five different failure modes observed in this study have been analyzed in detail. It can be concluded that the shearing modes including shearing along a wedge, along a single plane and dendritic shearing are associated with some pre-existing flaws, veins or bedding in the specimens. These micro-structures provide weakness planes for cracks to develop. It can also explain why the UCS values of tuff specimens failed in shearing modes are generally lower than those failed in other modes. In addition, the duration of cracking process from crack initiation to failure is much shorter for the specimens failed in shear modes as compared with those failed in other modes.

4 CONCLUSIONS

Failure modes and cracking processes of 11 granite specimens and 9 tuff specimens under uniaxial compression are examined in the present study. On the basis of the high-speed camera observation and analyses of the failure modes associated with the uniaxial compressive strengths, following conclusions are drawn:

- Five failure modes including axial splitting, shearing along a wedge, shearing along a single plane, dendritic shearing, multiple fracturing, are observed in the tested specimens.
- The ranges of the UCS for the tested granite and tuff specimens are from 27.02 to 225.22 MPa and from 85.06 to 247.63 MPa respectively. The average UCS of the tested granite and tuff specimens are 136.32 MPa and 154.54 MPa, respectively.
- Axial splitting is the most common mode of failure of the granite specimens. While there are no dominant failure modes for the tuff specimens.
- The shearing modes including shearing along a wedge, along a single plane and dendritic shearing are often associated with some pre-existing flaws, veins or bedding in the specimen, which provide weakness planes for cracks to develop
- The duration of cracking process from crack initiation to final failure is much shorter for the specimens failed in shear modes as compared with those failed in other modes.

5 REFERENCES

ASTM D4543-08. (2008) Standard Practices for Preparing Rock Core as Cylindrical Test Specimens and Verifying Conformance to Dimensional and Shape Tolerances. ASTM International, West Conshohocken, PA.

ASTM D7012-14. (2014) Standard Test Methods for Compressive Strength and Elastic Moduli of Intact Rock Core Specimens under Varying States of Stress and Temperatures. ASTM International, West Conshohocken, PA.

Brady, B.T. (1970) A mechanical equation of state for brittle rock Part.1 The pre-failure behavior of brittle rock. International Journal Rock Mechanics Mineral Science 7: 385-421

Basu A., Celestino T. B., Bortolucci A.A. (2009) Evaluation of rock mechanical behaviors under uniaxial compression with reference to assessed weathering grades. Rock Mechanics and Rock Engineering 42:73-93

Basu, A., Mishra, D.A., Roychowdhury, K. (2013) Rock failure modes under uniaxial compression, Brazilian, and point load tests. Bulletin of Engineering Geology and the Environment, 72(3-4): 457-475

Bobet, A., Einstein, H. H. (1998) Fracture coalescence in rock-type materials under uniaxial and biaxial compression. International Journal of Rock Mechanics and Mining Sciences, 35(7): 863-888

Bieniawski, Z.T. (1984) Rock mechanics design in mining and tunneling

Chen, G., Kemeny, J.M., Harpalani, S. (1995) Fracture propagation and coalescence in marble plates with pre-cut notches under compression. In: Symp. on Fractured and Jointed Rock Mass, Lake Tahoe, CA: 435-429

Davis, H.G., Reynolds S.J., Soo J., Kluth C. (1942) Structural geology of rocks and regions, 3rd edn.

Gupta, A.S., Rao, S.K,. (2000) Weathering effects on the strength and deformational behavior of crystalline rocks under uniaxial compression state. Engineering Geology, 56(3): 257-274

Hudson, J.A., Crouch, S.L., and Fairhurst C. (1972) Soft, stiff and servo-controlled testing machines: A review with reference to rock failure. Engineering geology 6: 155-189

Hudson, J.A., Harrison, J.P. (1997) Engineering rock mechanics. Pergamon, Oxford

Hudyma, N., Avar, B.B., Karakouzian, M. (2004) Compressive strength and failure modes of lithophysae-rich Topopah Spring Tuff specimens and analog models containing cavities. Engineering Geology, 73(1): 179-190

Reyes, O. and Einstein, H.H. (1991) Failure Mechanism of Fractured Rock -A Fracture Coalescence Model, Proceedings of the 7th International Congress of Rock Mechanics 1, Aachen, Germany: 333-340

Szwedzicki, T., Shamu, W. (1999) The effect of material discontinuities on strength of rock samples. In: Proc., Australasian Institute of Mining and Metallurgy 304 (1): 23-28

Szwedzicki, T. (2007) A hypothesis on modes of failure of rock samples tested in uniaxial compression. Rock Mechanics and Rock Engineering. 40(1): 97-104

Tang, C.A., Kou, S.Q. (1998) Crack propagation and coalescence in brittle materials under compression. Engineering Fracture Mechanics 61: 311-324

Waversik, W.R., Faurhurst, C. (1969) A study of brittle rock fracture in laboratory compression experiments. International Journal of Rock Mechanics and Mining Sciences. 7: 561-575. Porgamou Press 1970

Wong, T.F., Wong, R.H.C., Chau, K.T, Tang, C.A. (2006) Microcrack statistics, Weibull distribution and micromechanical modeling of compressive failure in rock. Mechanics of Materials 38: 664-681

Wong, L.N.Y., Einstein, H.H. (2009) Crack coalescence in molded gypsum and Carrara marble: part 2-microscopic observations and interpretation. Rock Mechanics and Rock Engineering 42: 513-545

Wong, L.N.Y., Einstein, H.H. (2009) Using high speed video imaging in the study of cracking processes in rock. Geotech Test J 32(2):164–180

Zhang, Q.B., Zhao, J. (2013) Determination of mechanical properties and full-field strain measurements of rock material under dynamic loads. International Journal of Rock Mechanics and Mining Sciences 60: 423-439

6 ACKNOWLEDGMENTS

The authors acknowledge the support from the HKU Start-up Fund, Seed Funding Program for Basic Research for New Staff at the University of Hong Kong, and the General Research Fund 2017/18 (#17303917) of the Research Grants Council (Hong Kong). The second author acknowledges the Postgraduate Scholarship from the University of Hong Kong. The Public Works Central Laboratory (PWCL) of the Civil Engineering Development Department (CEDD) is acknowledged for allowing us to conduct the tests on the MTS815 testing system. Contributions from PWCL support staff are gratefully acknowledged.

Loess and Its Nature Favouring Geohazards

Yanrong Li
Department of Earth Sciences and Engineering
Taiyuan University of Technology, China.
Collaborative Innovation Center for Geohazard Process and Prevention

Abstract

Loess is a porous, weakly cemented and unsaturated Quaternary sediment deposited by the wind in arid and semi-arid regions. It is widely and thickly distributed in China, making the Loess Plateau the largest bulk accumulation of loess on Earth. However, the fragile geoenvironment in the loess areas of China causes frequent and various geohazards. This study presents a whole view of loess via reviewing the history of loess study, spatial distribution in the world and landform classification. The loess failures are interpreted based on the reconstruction of macropore structure of loess by using computed tomography technology. It is revealed that loess is a geological material with a dense and complex network of pores and pipes. The pores showed good connectivity in the vertical direction and formed vertically aligned pipes but displayed weak connectivity in the horizontal directions. The pipes in the vertical direction were thick, long, and straight compared with those in the horizontal directions. This special structure results from loessification process which makes loess an anisotropic structure with vertically aligned weak units and vertically aligned strong structures. This anisotropy acts as a fundamental working together with precipitation, stress relaxation and vegetation to facilitate loess failures.

Submarine Groundwater Discharge and Nutrient Loadings in Tolo Harbor; Hong Kong Using Multiple Geotracer-Based Models, And Their Implications Of Red Tide Outbreaks

Xin Luo and Jiu Jimmy Jiao
Earth Sciences Department, The University of Hong Kong

Abstract: Multiple tracers, including radium quartet, ^{222}Rn and silica are used to quantify submarine groundwater discharge (SGD) into Tolo Harbor, Hong Kong in 2005 and 2011. Five geotracer models based on the end member model of ^{228}Ra and salinity and mass balance models of ^{226}Ra, ^{228}Ra, ^{222}Rn, and silica were established and all the models lead to an estimate of the SGD rate of the same order of magnitude. Groundwater borne nutrients are 1-2 orders of magnitude larger than other nutrient sources and the interannual variation of nutrient concentration in the embayment is more influenced by the SGD derived loadings. Climatologically driven SGD variability alters the SGD derived DIP loadings in this phosphate limited environment and may be the causative factor of interannual variability of red tide outbreaks from 2000-2013. Finally, a conceptual model is proposed to characterize the response of red tide outbreaks to climatological factors linked by SGD. The findings from this study shed light on the prediction of red tide outbreaks and coastal management of Tolo Harbor and similar coastal embayments elsewhere.

1. INTRODUCTION

During the past decades, submarine groundwater discharge (SGD) has gained considerable concerns from marine chemists and hydrogeologists since the SGD has proved to be a significant component of global water budget and plays a vital role in water transport and chemical fluxes at the coastal zones (Burnett et al. 2003, Charette et al. 2001, Moore 1996, 1999, 2010, Slomp and Van Cappellen 2004). The SGD is comprehensively defined as any and all flow of water on continental margins from the seabed to the coastal ocean, regardless of fluid composition or driving force (Burnett et al. 2003). Numerous studies have proved that SGD can induce the loadings of nutrients (Hwang et al. 2005, Lee et al. 2012, Luo et al. 2014), heavy metals and rare earth elements (Ganguli et al. 2012, Johannesson et al. 2011, Kim and Kim 2011), dissolved inorganic carbon (DIC) and dissolved organic carbon (DOC) (Cyronak et al. 2013, Kim et al. 2011, Liu 2011), heat (Santos et al. 2011) etc. Large SGD derived chemicals loadings, especially loadings of nutrients, significantly affect coastal ecosystems such as corals, mangroves and are attributable to the red tide occurrence (Blanco et al. 2011, Gleeson et al. 2013, Gobler and Sanudo-Wilhelmy 2001, Hu et al. 2006, Lee and Kim 2007, Lee et al. 2010, Su et al. 2013b).

Radium quartet, naturally occurring from uranium - thorium series, are highly concentrated in coastal groundwater due to high desorption rate and mobility in saline environment (Krishnaswami et al. 1982, Luo et al. 2000), which makes them ideal tracers to examine groundwater discharge in various environments such as the subterranean estuaries, continental shelves and lakes (Charette 2007, Moore 2003, Raanan et al. 2009, Swarzenski et al. 2007). Moreover, radium quartet are used to quantify the water mixing within embayments, continental shelves as well as open sea (Hancock et al. 2006, Moore 2000, Moore et al. 2006). Short-lived radium isotopes, ^{223}Ra ($t_{1/2}$ = 11 d) and ^{224}Ra ($t_{1/2}$ = 3.65 d), are proved to be

effective in estimating mixing rate and diffusivity near shore and in embayments (Hancock et al. 2006, Liu 2011, Luo et al. 2014, Wang et al. 2015b). Long-lived radium isotopes, ^{226}Ra ($t_{1/2}$ = 1605 yrs) and ^{228}Ra ($t_{1/2}$ = 5.7 yrs), are more frequently used in quantifying the SGD and the water mixing rates in the large scale systems such as continental shelves and open seas (Kawakami and Kusakabe 2008, Kim et al. 2005, Moore et al. 2008, Su et al. 2013a, Wang et al. 2015a). Besides radium quartet, ^{222}Rn, as a soluble and mobile gas, is also prevailingly used to quantify the SGD (Burnett and Dulaiova 2006, Cable et al. 1996, Tse and Jiao 2008) because ^{222}Rn is highly concentrated in groundwater due to continuous alpha recoil supply from its parent ^{226}Ra in the bedrock and aquifer matrix and its conservative behavior (Ku et al. 1992, Luo et al. 2000).

The catchment of Tolo Harbor, with an area of 160 km^2, is bounded by series of mountain blocks. The annual precipitation is 2030 mm. There are six main rivers and streams, namely Lan Tsuen (LT) River, Shan Liu (SL) Stream, Shing Mum (SM) River, Tai Po (TP) River, Tai Po Kau (TPK) Stream and Tung Tze (TT) Stream (Fig. 1a) around the harbor. The total annual runoff is 4.5 x 10^7 m^3 (Luo et al. 2014). The bedrock within the catchment is mainly formed by middle Jurassic – lower Craterous volcanic rocks. The main faults are trended from southwest to northeast (Fig. 1a). Ruxton (1957) indicates that the superficial materials, including the mantle of the weathering rock, colluviums and alluviums and beach sand, form a shallow unconfined aquifer with a depth around 20 m. Jiao et al. (2006) suggest that there would be a relatively deep confined aquifer beneath the seabed which consists of mud and sandy mud with a clay content of 10-30 % (Shaw 1992).

Tolo harbor, a semi-closed embayment, is located at the northeast of New Territories, Hong Kong. It extends 20 km from southwest to northeast and is connected to Mirs Bay via Tolo Channel with an entrance width less than 1.5 km (Choi and Lee 2004). It has an area of 52 km^2, a coastal line of 82 km and an average depth of 12 m (Lee et al. 2012, Luo et al. 2014). In the past 30 years, the population along the harbor has increased from 70,000 to 1 million after 2000. A large amount of nutrients are loaded into the harbor from the sources including anthropogenic sewages, atmospheric deposit, sediment release and groundwater discharge (Hu et al. 2001, Lee et al. 2012, Lee and Arega 1999, Wai et al. 2010, Wai et al. 2005). Semi-closed topography and long water residence time prevent the nutrients to be effectively removed (Choi and Lee 2004, Luo et al. 2014). Preliminary SGD studies within this district have been conducted since 2005, which reveals that the SGD can derive a large amount of nutrients into the embayment and enhance the primary productivities (Lee et al. 2012, Luo et al. 2014, Tse and Jiao 2008). High frequency of red tides has been reported since 1980s within the harbor (Hodgkiss and Ho 1997, Xu et al. 2004). The increase of N : P ratio in the harbor water is assumed to be the main controlling factor that leads to red tide outbreaks (Hodgkiss and Ho 1997).

On the basis of data of radium quartet, ^{222}Rn and nutrients in the two sampling years of 2005 and 2011, attempts are made to quantify the SGD with five geotracer-based models: three-end-member model, ^{226}Ra mass balance models, ^{228}Ra mass balance models, ^{222}Rn mass balance models and silica budget model in this study. The SGD derived nutrients are then estimated. With a wide range of climatological, geochemical data and red tide record from 2000- 2013 within the catchment, attempts are also made to explore the relation of the red tide occurrences to climatologically driven SGD variability.

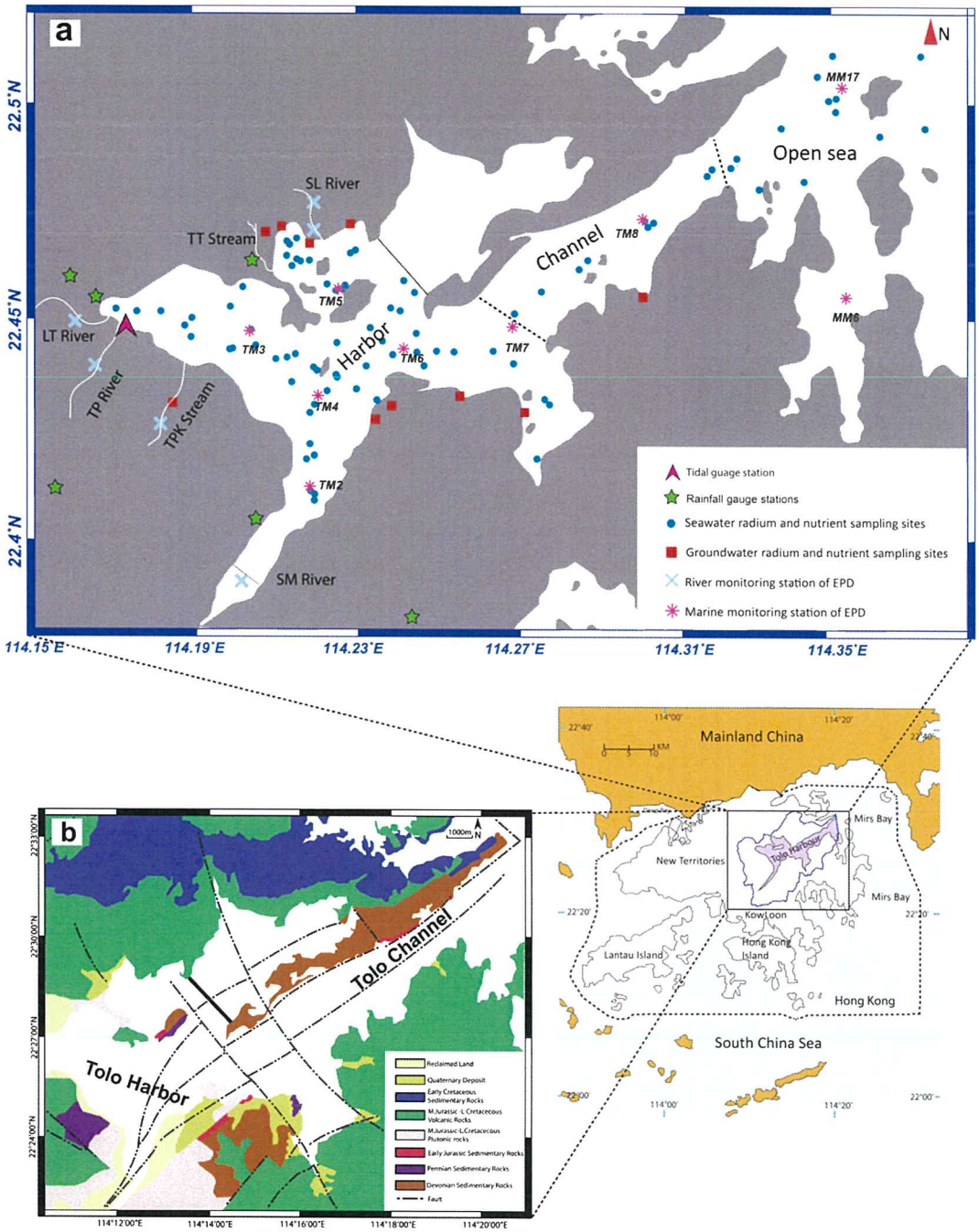

Fig. 1. Sampling sites of radionuclides and nutrients in 2005 and 2011 (a) and geological settings of Tolo Harbor (b). Locations of monitoring stations by are also illustrated in the

2. MATERIALS AND METHODS

2.1. Field works and analysis

Field works were mostly conducted in 2005 and 2011. For radium was extracted from 25-50 L of seawater, 10 L of river water and 2-5 L of well water within MnO_2 fibers (Moore 1976). Radium particulate desorption experiments were also done for river samples as described by Moore and Scott (1986). ^{222}Rn samples in seawater were measured by RAD7 Big Bottle System as described by Lee and Kim (2006), and in groundwater was measured with RAD H_2O (Durridge Co.). Nutrient samples were taken with 50 ml bottles (Nalgene, Co.) and stored in a freezer under - 4 °C till the measurements. Salinity and temperature were measured in situ with a TLC meter (Solinst, Co.)

^{223}Ra and ^{224}Ra were measured with Radium Delayed Coincidence Counting (RaDeCC) as

described by Moore and Arnold (1996). The detecting uncertainty is 7-15 % for ^{224}Ra and 12 – 20 % for ^{223}Ra (Garcia-Solsona et al. 2008, Luo et al. 2014, Moore 2008, Moore and Arnold 1996). ^{226}Ra were measured with RAD7 after the nuclide in secular equilibrium with ^{222}Rn (Kim et al. 2001, Lee et al. 2012). ^{228}Ra was measured with RaDeCC via measuring ^{228}Th ingrown from ^{228}Ra and calculating the initial ^{228}Ra (Charette et al. 2015, Kiro et al. 2013, Moore 2008). The detection uncertainty for ^{226}Ra and ^{228}Ra is 10-20 % and 7-15 %, respectively. Dissolved inorganic nitrogen (DIN, the sum of NO_3^-, NO_2^- and NH_4^+), dissolved inorganic phosphorous (DIP), and dissolved inorganic silicate as $Si(OH)_4$ were detected with flow injection analysis (FIA) equipped with auto-sampler (QuickChem® 3000) in the School of Biological Sciences of the University of Hong Kong (Kim et al. 2011, Luo et al. 2014).

2.2. Time series data

Various marine chemical, climatological and red tide outbreak record datasets from 2000-2013 are collected from several departments of the Hong Kong Government. The nutrient data were collected from 9 marine stations including TM2 to TM7 in the harbor and MM6 and MM17 in the open sea and 6 river stations from 2000-2013 established by Environmental Protection Department (EPD), Hong Kong. Surface runoff dataset were also collected from riverine monitoring stations by EPD. Climatological data including rainfall, evapotranspiration (ET), tidal range, mean sea level (MSL) were collected from Hong Kong Observatory (HKO). Generally, daily rainfall data are collected from 6 auto-recorded weather stations installed within the Tolo Harbor control zone catchment as shown in Fig. 1a. Daily ET data were collected from the station installed at King's Park (22°18'43", 114°10'22"), which is about 10 km from Tolo Harbor. Daily tidal range data and mean sea level (MSL) were collected from the tidal gauge station installed at Tai Po Kau (22°26'33", 114°11'2") by HKO as shown in Fig. 1a. All the daily data are yearly bin-averaged for the convenience of discussion. Red tide outbreak data were collected from Agriculture, Fisheries and Conservation Department (AFCD), Hong Kong. Red tide occurrences and types were yearly binned for discussion convenience.

2.3 Multiple isotope-based models

Generally, five isotopic based models are used in this study, which are (1) three endmember model based on the mass balance of salinity, water and ^{228}Ra, (2) mass balance model of ^{226}Ra, (3) mass balance model of ^{228}Ra, (4) ^{222}Rn steady mass model, and (5) silica budget model. The description of all the models and the input of all the parameters can be found in the author's previous studies (Luo and Jiao, 2016; Luo et al. 2014, Luo et al. 2016, Luo et al. 2017)

3. RESULTS

3.1 Radium quartet results

The results of radium quartet, in different water end members are shown in Figs. 1-3. The activities of radium quartet in the seawater of Tolo Harbor are within the range of radium activities in other studies (Charette and Buesseler 2004, Charette et al. 2001, Hwang et al. 2010, Krest et al. 2000, Moore et al. 2006, Peterson et al. 2008, Santos et al. 2010, Swarzenski et al. 2007). Spatial distribution of radium quartet, salinity and ^{222}Rn from samples collected in 2005 and 2011 are shown in Figs. 2 and 3, respectively. Salinity is lower in the harbor compared to those in the channel and open sea (Fig. 1a), suggesting runoff dilution and submarine groundwater discharge effects. The harbor water is comprised of much higher radium quartet and ^{222}Rn concentrations compared to those in the channel and open sea water. Concentrated radionuclides are possibly resulted from the SGD. The upper layer (depth: 0.5 m) of the harbor water has a relatively higher radionuclide concentration compared to that at the bottom layer (depth: 5 m), which reflects the large lateral groundwater discharge compared to the bottom

groundwater discharge and sedimentary fluxes (Luo et al. 2014, Santos et al. 2010). Radium excesses in the harbor water allow these nuclides to be ideal tracers in establishing the tidal mixing model (Charette et al. 2001, Moore et al. 2006). The distribution patterns of radium quartet are similar in the two sampling years, also higher in the harbor and relatively lower at the channels and the open sea. However, concentrations of radium quartets are higher in 2005 than 2011, which reflects the interannual variability of radium input derived from the SGD (Wilson 2005). Radium quartet concentrations differ greatly in different water end members. River water has relatively lower activities due to high radium adsorption rate to the particulate and short radionuclide-riverbed reaction time in freshwater environments (Luo et al. 2000). Saline groundwater has much higher radium activities, about 1–2 orders of magnitude larger than those of river water and sea water as shown in Fig. 4. Radium concentrations in saline groundwater are elevated due to the high desorption rate in saline environment and high production rate from radium in solid phase (Krishnaswami et al. 1982, Ku and Luo 1992, Luo et al. 2000). The large activities difference in water from different end members allows radium quartet to be effective tracers in quantifying SGD.

3.2. Radon-222 results

^{222}Rn concentrations for different water members are shown in Figs. 1-3. Radon activities in the seawater of two sampling years are significantly low compared to that of groundwater (n = 36, 10^3 - 10^5 Bq m^{-3}), but comparable to those of river water (n = 5, 10^2 – 10^3 Bq m^{-3}) as displayed in Fig. 4. High radon activities in groundwater are caused by continuous α-recoil supply from the parent isotope ^{226}Ra in the soils and rocks (Ku et al. 1992, Porcelli 2008). The spatial distributions of ^{222}Rn in the two sampling years are displayed in Figs 2 and 3. ^{222}Rn excess is observed in the channel water compared to the open sea water, indicating higher radon input from groundwater.

3.3. Nutrient results

The results of DIN, DIP and DSi are shown in Fig. 5. Much higher nutrient concentrations are observed in 2011 in harbor water, especially at the river plume zones,

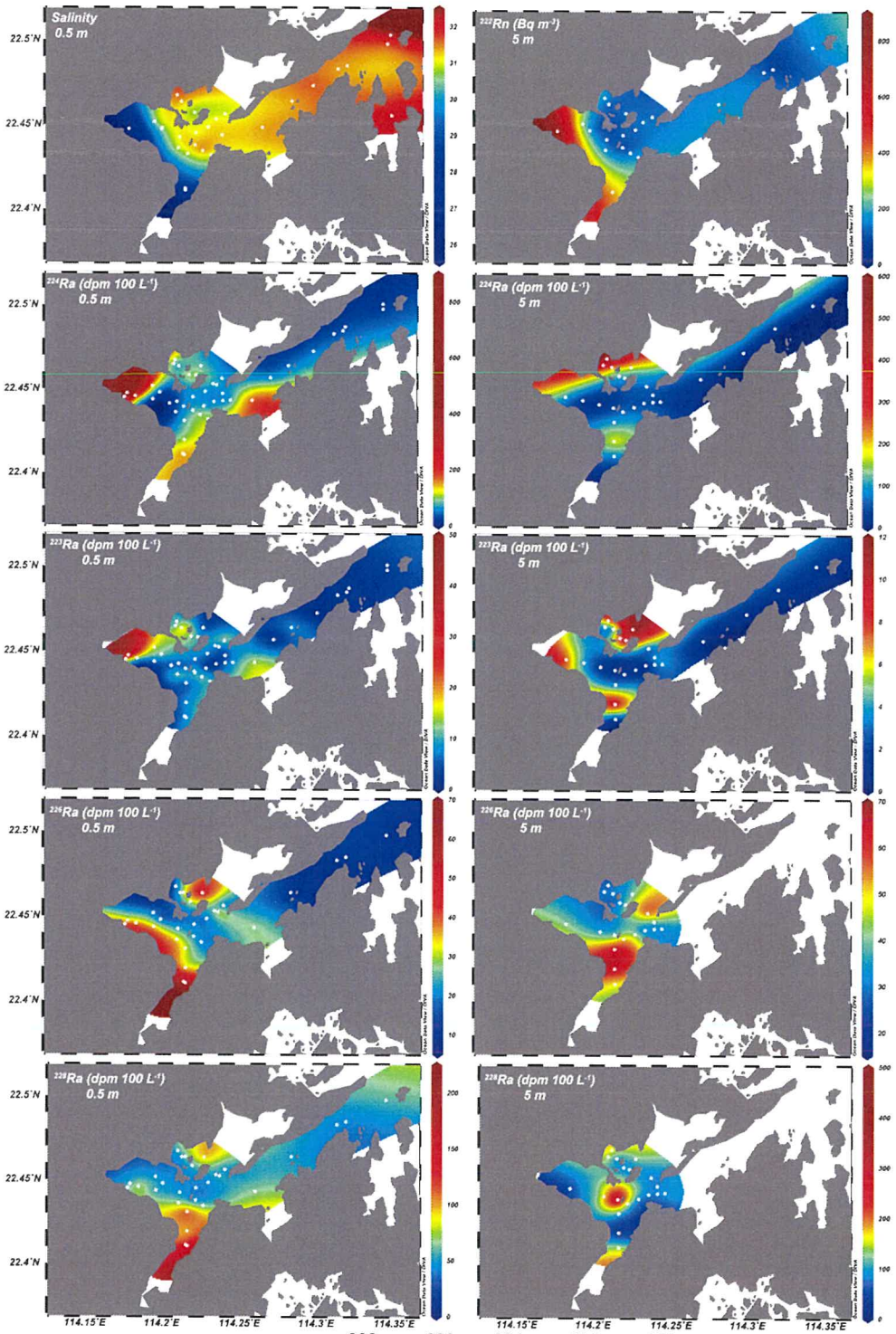

Fig. 2. Distributions of salinity, ^{222}Rn, ^{223}Ra,^{224}Ra, ^{226}Ra, ^{228}Ra in the upper water and bottom water of Tolo Harbor in 2005.

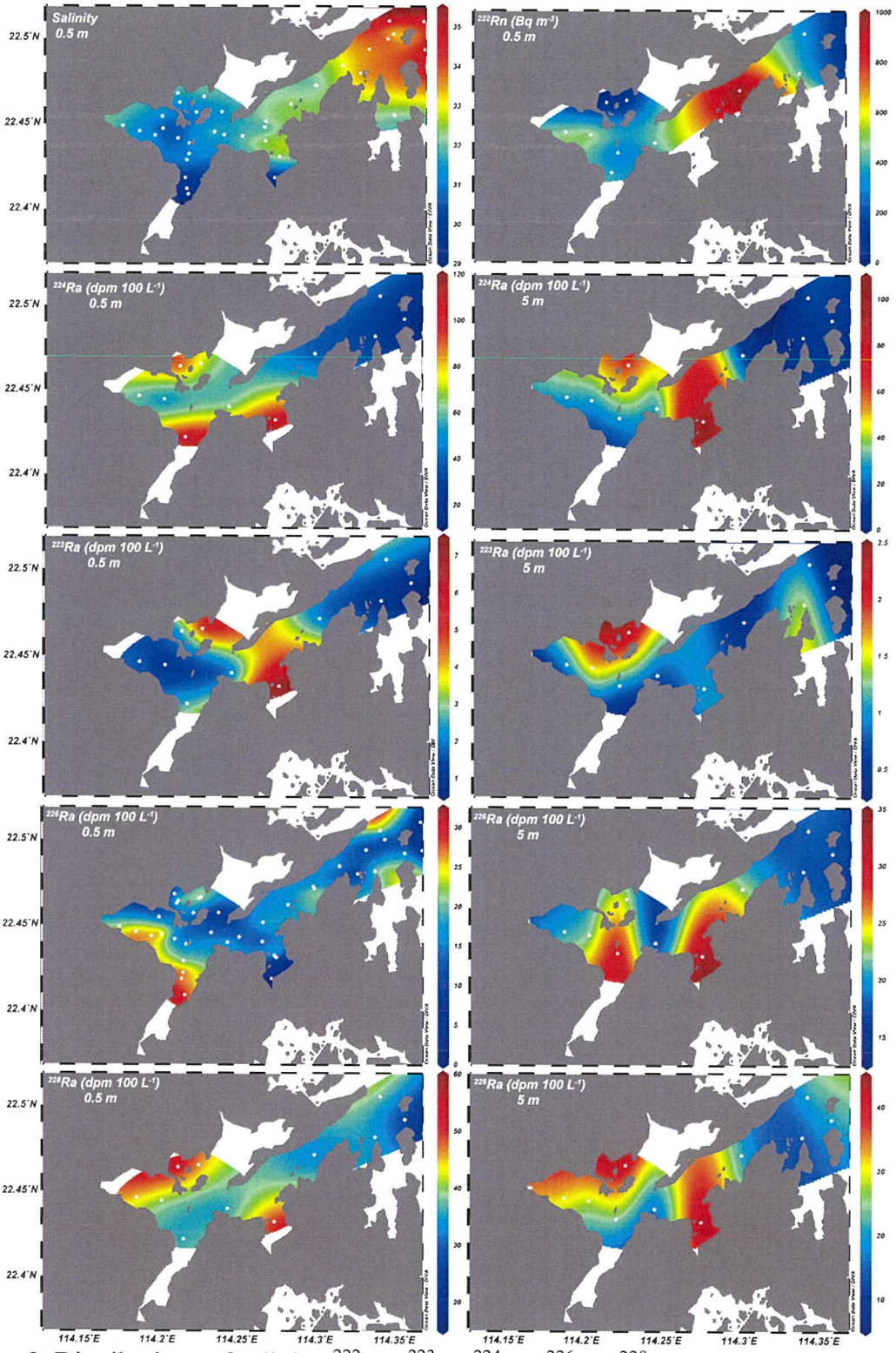

Fig. 3. Distributions of salinity, ^{222}Rn, ^{223}Ra,^{224}Ra, ^{226}Ra, ^{228}Ra in the upper water and bottom water of Tolo Harbor in 2011.

suggesting the terrestrial inputs. For the samples of 2005, DIN and DSi are much higher in the harbor water in related to the open seawater. However, the DIP concentrations are higher in the channel and open seawater compared to the harbor water. The averaged nutrient compositions

are higher in 2005 compared to those in 2011, indicating an interannual variability of nutrient inputs. Groundwater and river water contain significantly higher nutrient concentrations than those in seawater, suggesting groundwater and river water are important nutrient sources to the embayment (Fig. 5). After entering the embayment water, nutrients decline exponentially, which suggests that processes such as biological removal could be dominated compared to the linear tidal mixing loss (Kim et al. 2011, Moore et al. 2006).

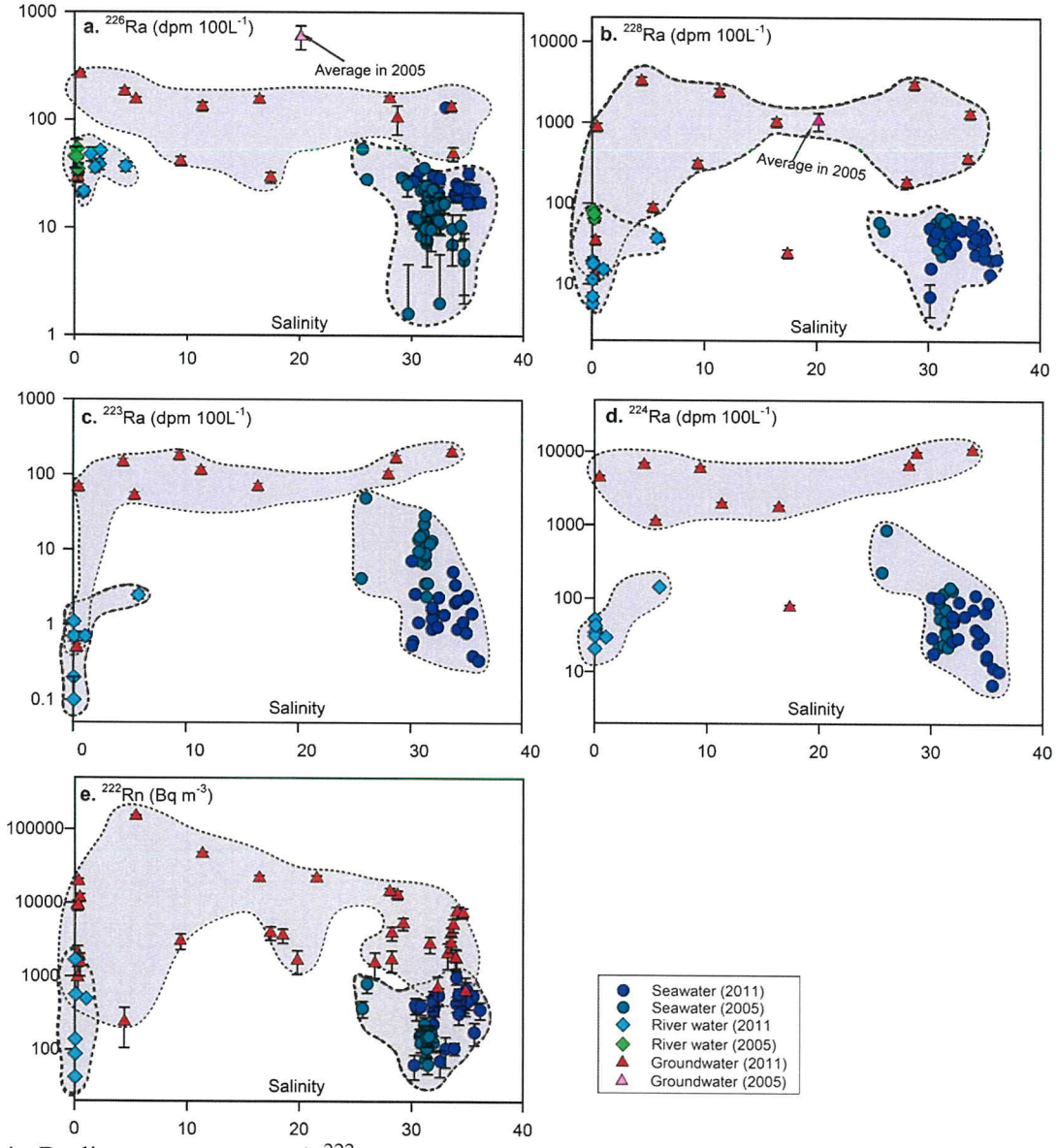

Fig. 4. Radium quartets and ^{222}Rn versus salinity, indicating the well clustered of radium quartets and ^{222}Rn.

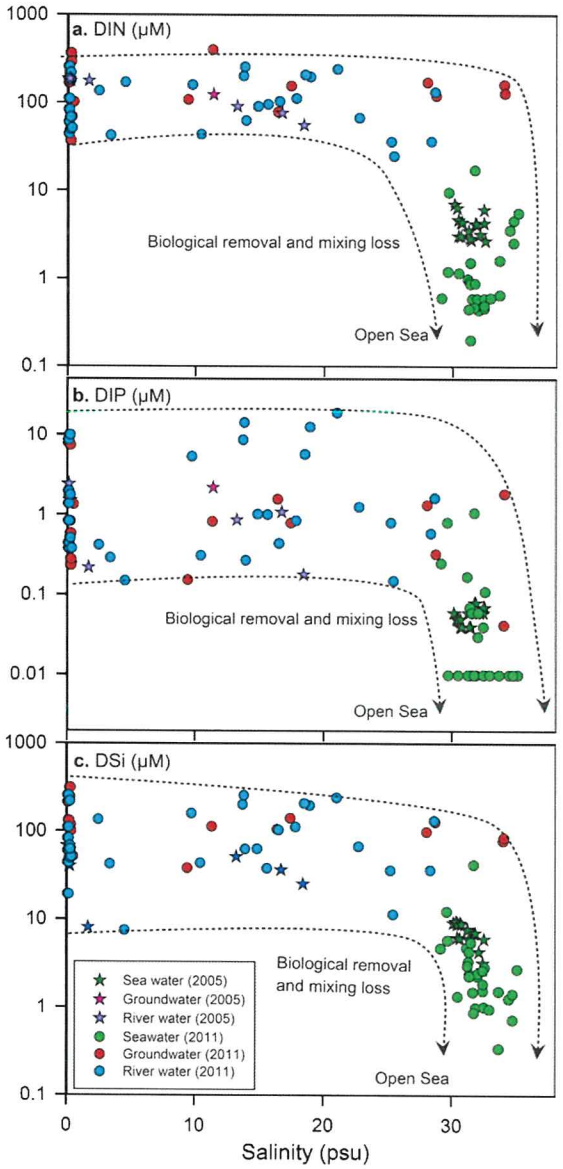

Fig. 5. DIN (a), DIP (b) and DSi (c) in relation with salinity in groundwater, river water and harbor water in 2005 and 2011.

4. DISCUSSION

4.1 Interannual variability of SGD

Overall five tracer-based mass models are used to quantify the SGD into Tolo Harbor. The SGD rates yielded from different models range from 0.02 to 11.8 cm d^{-1} in Tolo Harbor. The three-end-member model yields the lowest SGD rate and the ^{222}Rn model leads to the largest result for all the two sampling years. In general, there has been a good agreement among the radium, silica and radon mass balance models, with the main outlier being estimated with three endmember model. These differences have been attributed to the fact the three endmember model is mostly based on water mass balance and greatly relied on the river gauge data, while the other models include a component of recirculated seawater which could be the substantial component in Tolo Harbor (Lee et al. 2012, Luo et al. 2014). The radon based model leads to the highest SGD estimates among the five models. ^{222}Rn is a noble gas and groundwater salinity will not control its activity. Furthermore, because of its short half life, ^{222}Rn in groundwater will reach the secular equilibrium with the sediment derived ^{226}Ra sources within

3 weeks (Kim et al. 2001). Thus, ^{222}Rn is of advantage to estimate the total SGD, regardless of fluid origins and compositions (Burnett et al. 2003). The large uncertainties of the radon based models are ascribed to the relatively large uncertainties of ^{222}Rn measurements due to its low activities, none obvious inner harbor ^{222}Rn excess in related to the open sea, and the relatively long harbor water residence time in related to the half life of ^{222}Rn. The radium and silica models are usually more sensitive to brackish and saline discharge (Mulligan and Charette, 2006, Hwang et al. 2005a), and may reflect the dominant component of recirculated seawater and the associated nutrient loadings. The variable activities of ^{222}Rn and ^{226}Ra in the groundwater endmember would be the main causative factor of the uncertainties in the SGD estimate, and may induce the inappropriateness of using the average activities to estimate the SGD, as described elsewhere (Mulligan and Charette, 2008). To put this study in the context of existing studies elsewhere, the SGD in this study are compared to the geo-tracer based studies in the embayments, harbors and other coastal areas elsewhere (Table 2). The ^{222}Rn and radium model results in this study fall in the ranges of many other radium based SGD estimation, suggesting the tenability of the SGD in this study. The difference of SGD based on different geo-tracer based models may reflect the component differences in the fluids supplying geo-tracers into the harbor (Mulligan and Charette, 2006, Prieto and Destouni, 2011). The weighted average SGD rates of the five models may represent the full extent of the fluids discharging into the harbor, and the mean SGD rate of the five models is 5.42 cm d^{-1} and 2.66 cm d^{-1} in 2005 and 2011, respectively. All the five models leads much higher SGD rate in 2005 compared to that in 2011 (Fig. 6), indicating interannual variability of the SGD in Tolo Harbor.

The river discharge is 0.16 cm d^{-1} and 0.13 cm d^{-1} in 2005 and 2011 to the harbor. The estimated SGD rates in both years are about one order of magnitude larger than the river discharge rate. The driving force of the SGD includes hydraulic gradients, tidal pumping and density flow etc. (Li et al. 1999, Robinson et al. 2007, Santos et al. 2012). In an unconfined coastal aquifer, the hydraulic gradient variations mostly reply on climatological parameters of regional precipitation, ET and MSL variability (Asano et al. 2002, Gonneea et al. 2013, McDonnell 1990, Pearce et al. 1986). Thus, hydrological parameters within the catchment contribute to interannual variability of the SGD rates, especially fresh submarine groundwater discharge (FSGD) fluctuations (Anderson and Emanuel 2010, Destouni et al. 2008, Wilson 2005). Recirculated seawater, the dominant component of SGD, is mostly regulated by the tidal pumping, which is a function of mean tidal range (Li et al. 1999, Nielsen 1990, Wilson et al. 2015). Therefore, the synergistic impact of temporal variation of precipitation, ET, MSL and mean tidal range mostly likely leads to interannual variability of the SGD in Tolo Harbor. Higher SGD rate in 2005 are mainly due to the combination effect of higher precipitation, lower ET and lower MSL.

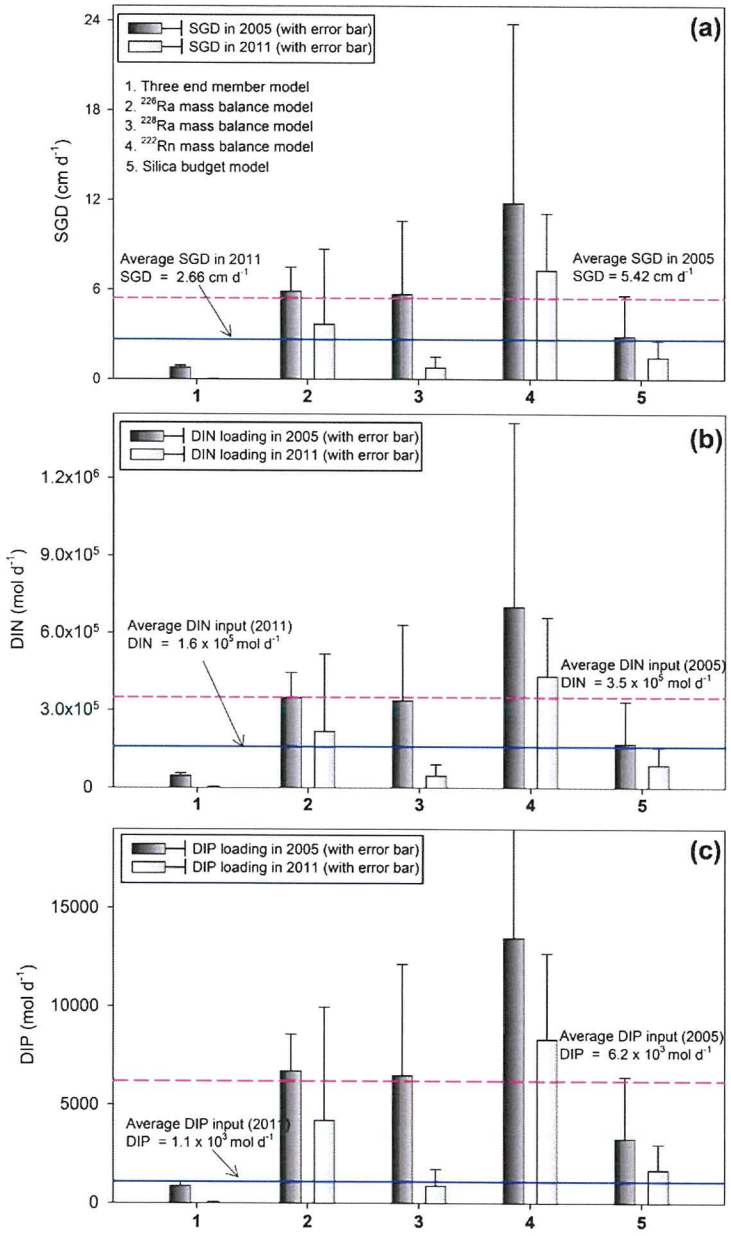

Fig. 6. SGD rates (a) and SGD derived DIN (b) and DIP (c) loadings based on different SGD models in 2005 and 2011.

4.2. SGD and red tide occurrence

Nutrient concentrations in the river water and groundwater are significantly higher than those in the embayment water (Fig. 5). N : P ratio and Si : P ratio in all types of waters are much larger than the Redfield ratio ([C]: [N]: [Si]: [P] = 106:16:15:1), indicating the phosphate limited environment. Mean DIN concentrations in the groundwater is 124.2 μM and 157.5 μM, and mean DIP concentrations in the groundwater is 2.2 μM and 0.78 μM, in 2005 and 2011, respectively. The total groundwater borne DIN is then calculated to be 3.5 x 10^5 mol d^{-1} and 1.6 x 10^5 mol d^{-1}, DIP to be 6.2 x 10^3 mol d^{-1} and 1.1 x 10^3 mol d^{-1}, in 2005 and 2011, respectively (Fig. 6). Using the river discharge rate and nutrient concentration in the river water, the riverine input of DIN is calculated to be 2.4 x 10^3 mol d^{-1} and 1.8 x 10^3 mol d^{-1} in 2005 and 2011, respectively, and that of DIP to be 96 mol d^{-1} and 65 mol d^{-1}, in 2005 and 2011, respectively. SGD derived nutrient loadings are 1-2 orders of magnitude larger than the riverine nutrient loadings in both sampling years. In addition to groundwater borne nutrients, there are other

nutrient sources such as atmospheric dry and wet deposits (Paerl and Fogel 1994, Paerl 1997, Wai et al. 2010, Wai et al. 2005, Wang et al. 2013), sedimentary release (Chau 2002, Hu et al. 2001) and point sources from sewages and waste water within a coastal embayment (Anderson et al. 2002, Lee and Arega 1999, Paerl 1997, Xu et al. 2004, Yung et al. 1997). Wai et al. (2005; 2010) estimated the atmospheric deposit of DIN into Tolo Harbor water bodies as 2.34 x 10^4 mol d^{-1}, suggesting that the atmospheric nutrient deposits into the harbor water are comparable to riverine flux and about one order of magnitude lower than the amount of groundwater borne nutrients. Yung et al. (1997) and Xu et al. (2004) summarized that the point sources and the sewage DIN input is within a range of 1.5 x 10^4 - 6.2 x 10^4 mol d^{-1}, which is times lower than the SGD derived nutrient loadings. Hu et al. (2001) and Chau (2002) estimated sedimentary DIN release to be about 1.8 x 10^5 mol d^{-1}, and sedimentary DIP release about 145 mol d^{-1}. The sediment releases DIN comparable to that derived from SGD, but DIP one order of magnitude lower than that from SGD. Thus, compared to other nutrient sources, groundwater borne nutrient is the dominant component and spatio-temporal distributions of nutrients in the harbor are most likely controlled by SGD derived nutrient loadings.

To explore the relation of red tide outbreaks and nutrient dynamics in harbor water, red tide outbreak frequency and types from 2000-2013 are collected from the AFCD, as shown in Fig. 7*I*. Quite high red tide occurrence was recorded in 2000, 2001, 2005, while there was much lower red tide occurrence during 2006 - 2013. The dominant specie of red tide outbreak is dinoflagellate. The riverine DIP input and runoff show quite weak correlations with the red tide outbreaks (Fig. 7*II* a and b), indicating the riverine nutrient loadings are probably not a key factor in controlling red tide outbreaks.

The spatio - temporal patterns and distributions of groundwater nutrient inputs are speculated to play a critical role in red tide outbreaks (Hu et al. 2006, Lee and Kim 2007, Lee et al. 2010). Hodgkiss and Ho (1997) investigated the N : P ratios in Tolo harbor during 1980s – 1990s and suggested that high N : P ratio limited the red tide outbreaks. However, red tide outbreak frequency shows weakly negative correlation (r = - 0.2, $0 < p < 0.05$) with the N : P ratios from 2000 – 2013 (Fig. 7*II* d). DIP concentrations show high positive correlation (r = 0.72, $0 < p < 0.05$) with red tide outbreak frequency (Fig. 7*II* c), which is reasonable under the high phosphate limited environments where the growth of red tide species is mainly regulated by the phosphate supply. Compared to other DIP sources, SGD derived DIP loading is predominant as discussed above. Therefore it is speculated that the SGD plays an important role in red tide occurrence in Tolo Harbor.

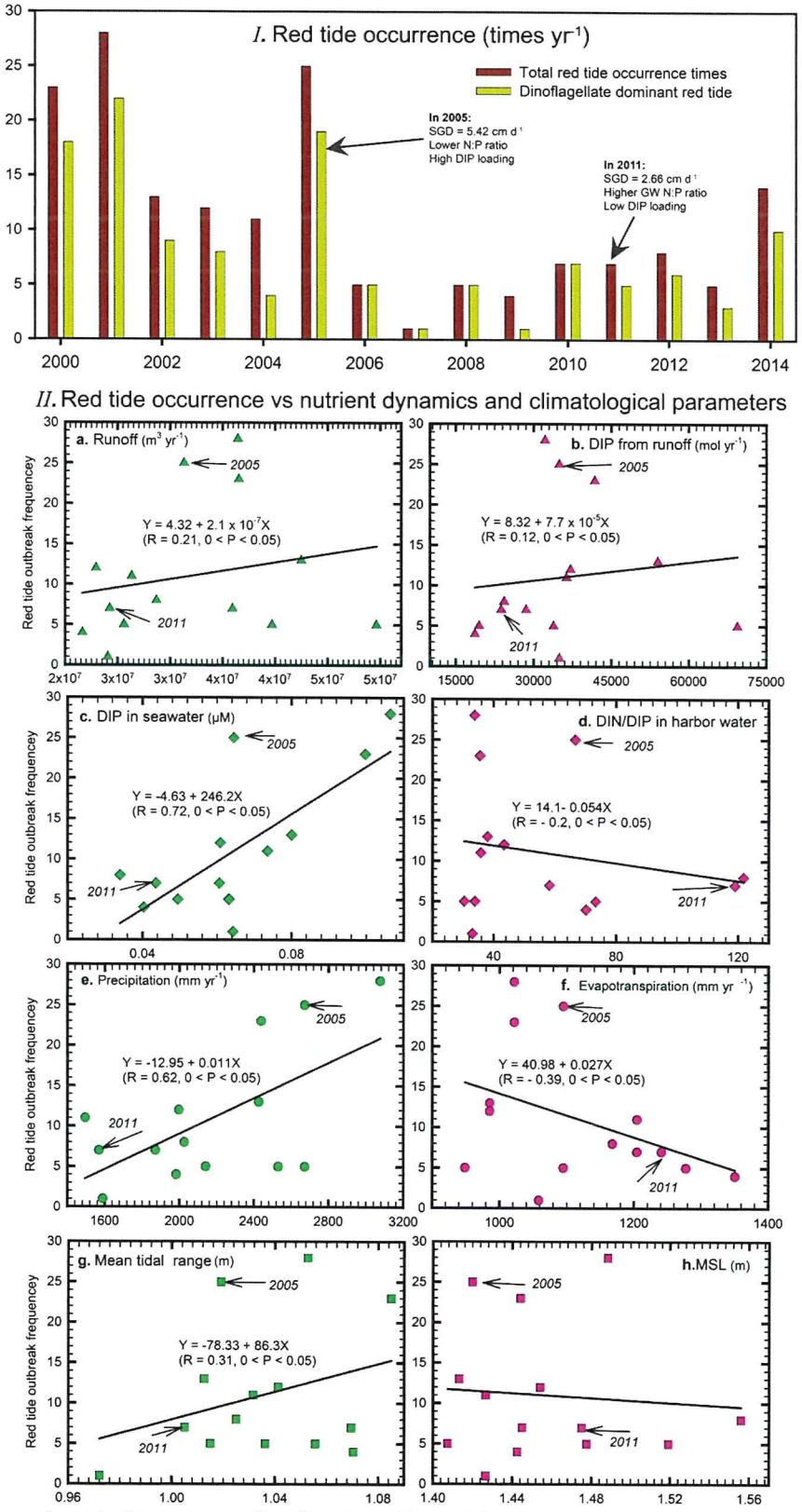

Fig. 7. Red tide outbreak frequency distribution (*I*) and its relation with nutrient dynamics and climatological parameters (*II*).

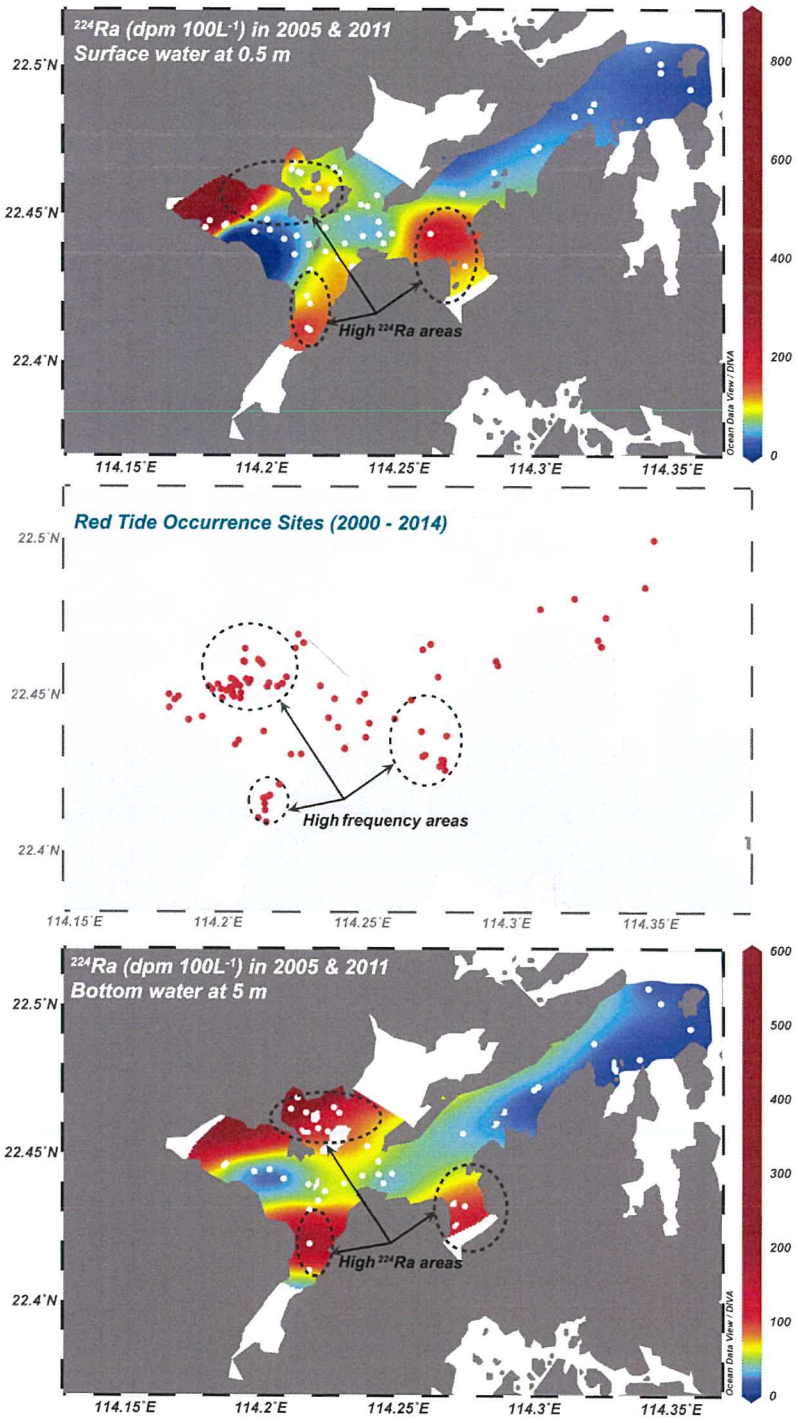

Fig. 8. Spatial distribution of ^{224}Ra in the harbor water in at upper and bottom layer, compared with the red tide occurrence distribution during 2000 – 2014. The unit of ^{224}Ra is dpm 100 L^{-1}.

Red tide outbreak frequency is compared with climatological parameters to investigate the relation between the climatologically influenced SGD and red tide outbreaks (Fig. 7 *II e-h*). Precipitation shows very positive correlation (r = 0.62, 0 < p < 0.05) with red tide outbreak frequency, and ET are negatively correlated with red tide outbreak frequency (r = - 0.39, 0 < p < 0.05) (Fig. 7 *II e-f*). The difference between precipitation and ET in the Tolo Harbor catchment reflects the total amount of groundwater available in the catchment, which largely flows directly to the sea in the form of the SGD, although a small part of which becomes runoff, which eventually also discharges to the sea. Thus, high precipitation and low ET lead to the high SGD rate and high DIP input, and enhance the red tide outbreaks. Mean tidal range shows

a positive correlation ($r = 0.31$, $0 < p < 0.05$) with red tide outbreaks (Fig. 7 *II g*). Large mean tidal range tends to intensify water mixing and seawater recirculation at the intertidal zones, and enhance the SGD derived DIP loadings in the harbor, leading to more red tide outbreaks. During the higher SGD rate year in 2005, there are 25 red tide outbreaks, compared to much less outbreaks in the lower SGD rate year in 2011. Much high SGD derived DIP loadings are likely the cause of more red tide outbreaks in 2005.

To examine the spatial relationship between SGD and red tide occurrence, ^{224}Ra spatial distribution versus red tide occurrence sites are compared and the results are shown in Fig. 8. ^{224}Ra can serves as a proxy of transient SGD magnitude since this nuclide distribution responses rapidly and sensitively to groundwater input (Lee and Kim 2007, Lee et al. 2010). Red tide occurred more frequently at three zones, where ^{224}Ra activities were also relatively higher (Fig. 8). This suggests that there is certain connection between high frequency of red tide outbreaks and SGD distribution.

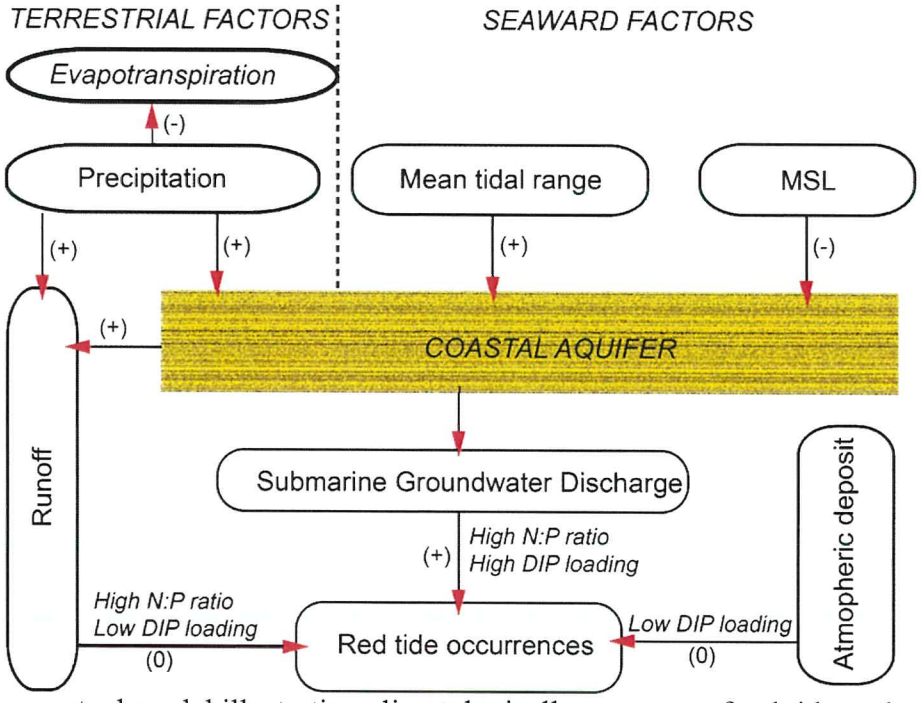

Fig. 9. A conceptual model illustrating climatologically response of red tide outbreaks via SGD. (+) indicates positive correlation, (-) indicates negative correlation and (0) indicates no significant correlation.

To this end, a conceptual model is proposed to characterize the response of red tide outbreak to climatological factors via SGD, as shown in Fig. 9. Generally, the variability of precipitation, ET, MSL and mean tidal range affects the SGD and then the nutrient loadings to the harbor, which finally alters the trophic states and triggers or dampens red tide outbreaks. Precipitation and mean tidal range exhibit positive correlation with red tide outbreaks, while ET is negatively correlated with red ride outbreaks. Interannual variability of groundwater borne DIP is possibly the determinant factor of red tide outbreak fluctuation within this highly phosphate limited embayment. Though the riverine fluxes and atmospheric deposit and point sources may induce a portion of DIP loadings into the harbor, their effect is seemly limited compared to the SGD derived DIP loadings.

5. CONCLUSION

To conclude, the SGD rate of Tolo harbor in 2005 and 2011 is estimated with five geotracer-based models, including three-end-member model based on ^{228}Ra and salinity, ^{226}Ra mass balance model, ^{228}Ra mass balance model, ^{222}Rn mass balance model, and silica budget model. The estimated SGD rates from these models are of the same order of magnitude. All the models lend to higher SGD rate in 2005 than that in 2011. SGD is estimated to be $\approx$5.42 cm d^{-1} and $\approx$ 2.66 cm d^{-1} in 2005 and 2011, respectively, confirming the interannual variability of the SGD. SGD derived DIN loadings are estimated to be 3.5 x 10^5 mol d^{-1} and 1.5 x 10^4 mol d^{-1} in 2005 and 2011, and DIP loadings 6.2 x 10^3 mol d^{-1} and 1.1 x 10^3 mol d^{-1} in 2005 and 2011. Groundwater borne nutrients are 1 - 2 orders of magnitude larger than other nutrient sources and the interannual variation of nutrient concentration in the embayment is more influenced by SGD derived loadings. Annual DIP concentrations in the harbor water are positively correlated with the precipitation and annual mean tidal range, and negatively correlated with ET. Climatologically driven SGD variability alters the SGD derived DIP loadings in this highly phosphate limited environment and is likely the causative factor of interannual variability of red tide out breaks. Finally, a conceptual model is proposed to explain the response of red tide outbreak to climatological factors via the SGD. This study sheds light on the prediction and managements of red tides in Tolo Harbor which suffers from highly frequent red tide outbreaks. But more endeavors integrating physical-chemical-biological cooperative studies are still in great need to further explore the red tide outbreak mechanisms and to prevent more red tide outbreaks.

ACKNOWLEDGEMENTS

This study was supported by a grant from the Research Grants Council of Hong Kong (HKU 7028/06P) and National Natural Science Foundation of China (No.41372261). Many thanks are given to Kiu-chung, Tse, Yi-kei Chan and Wai-yan Chu for their kind help in the field work and laboratory analysis. Appreciations are given to Environmental Protection Department, Hong Kong, Agriculture, Fisheries and Conservation Department, Hong Kong, Hong Kong Observatory for their help in accessing to the online dataset. The comments from the Organizing Committee of the Geological Society of Hong Kong -35th Anniversary Conference 2017 are gratefully acknowledged.

REFERENCES

Anderson, D.M., Glibert, P.M. and Burkholder, J.M. (2002) Harmful algal blooms and eutrophication: nutrient sources, composition, and consequences. Estuaries 25(4), 704-726.

Anderson, W.P. and Emanuel, R.E. (2010) Effect of interannual climate oscillations on rates of submarine groundwater discharge. Water Resources Research 46(5).

Asano, Y., Uchida, T. and Ohte, N. (2002) Residence times and flow paths of water in steep unchannelled catchments, Tanakami, Japan. Journal of Hydrology 261(1), 173-192.

Blanco, A.C., Watanabe, A., Nadaoka, K., Motooka, S., Herrera, E.C. and Yamamoto, T. (2011) Estimation of nearshore groundwater discharge and its potential effects on a fringing coral reef. Marine Pollution Bulletin 62(4), 770-785.

Burnett, W.C., Bokuniewicz, H., Huettel, M., Moore, W.S. and Taniguchi, M. (2003) Groundwater and pore water inputs to the coastal zone. Biogeochemistry 66(1-2), 3-33.

Burnett, W.C. and Dulaiova, H. (2006) Radon as a tracer of submarine groundwater discharge into a boat basin in Donnalucata, Sicily. Continental Shelf Research 26(7), 862-873.

Cable, J.E., Burnett, W.C., Chanton, J.P. and Weatherly, G.L. (1996) Estimating groundwater discharge into the northeastern Gulf of Mexico using radon-222. Earth and Planetary

Science Letters 144(3-4), 591-604.
Charette, M.A. (2007) Hydrologic Forcing of Submarine Groundwater Discharge: Insight from a Seasonal Study of Radium Isotopes in a Groundwater-dominated Salt Marsh Estuary. Limnology and Oceanography 52(1), 230-239.
Charette, M.A. and Buesseler, K.O. (2004) Submarine groundwater discharge of nutrients and copper to an urban subestuary of Chesapeake bay (Elizabeth River). Limnology and Oceanography 49(2), 376-385.
Charette, M.A., Buesseler, K.O. and Andrews, J.E. (2001) Utility of radium isotopes for evaluating the input and transport of groundwater-derived nitrogen to a Cape Cod estuary. Limnology and Oceanography 46(2), 465-470.
Charette, M.A., Morris, P.J., Henderson, P.B. and Moore, W.S. (2015) Radium Isotope Distributions during the US GEOTRACES North Atlantic Cruises. Marine Chemistry 177, 184-195.
Chau, K. (2002) Field measurements of SOD and sediment nutrient fluxes in a land-locked embayment in Hong Kong. Advances in Environmental Research 6(2), 135-142.
Choi, K.W. and Lee, J.H.W. (2004) Numerical determination of flushing time for stratified water bodies. Journal of Marine Systems 50(3-4), 263-281.
Cyronak, T., Santos, I. and Eyre, B. (2013) Permeable coral reef sediment dissolution driven by elevated pCO2 and pore water advection. Geophysical Research Letters.
Destouni, G., Shibuo, Y. and Jarsjo, J. (2008) Freshwater flows to the sea: Spatial variability, statistics and scale dependence along coastlines. Geophysical Research Letters 35(18).
Ganguli, P.M., Conaway, C.H., Swarzenski, P.W., Izbicki, J.A. and Flegal, A.R. (2012) Mercury Speciation and Transport via Submarine Groundwater Discharge at a Southern California Coastal Lagoon System. Environmental Science & Technology 46(3), 1480-1488.
Garcia-Solsona, E., Garcia-Orellana, J., Masque, P. and Dulaiova, H. (2008) Uncertainties associated with Ra-223 and Ra-224 measurements in water via a Delayed Coincidence Counter (RaDeCC). Marine Chemistry 109(3-4), 198-219.
Gleeson, J., Santos, I.R., Maher, D.T. and Golsby-Smith, L. (2013) Groundwater-surface water exchange in a mangrove tidal creek: Evidence from natural geochemical tracers and implications for nutrient budgets. Marine Chemistry.
Gobler, C.J. and Sanudo-Wilhelmy, S.A. (2001) Temporal variability of groundwater seepage and brown tide blooms in a Long Island embayment. Marine Ecology-Progress Series 217, 299-309.
Gonneea, M.E., Mulligan, A.E. and Charette, M.A. (2013) Climate-driven sea level anomalies modulate coastal groundwater dynamics and discharge. Geophysical Research Letters.
Hancock, G.J., Webster, I.T. and Stieglitz, T.C. (2006) Horizontal mixing of Great Barrier Reef waters: Offshore diffusivity determined from radium isotope distribution. Journal of Geophysical Research-Oceans 111(C12).
Hodgkiss, I. and Ho, K. (1997) Are changes in N: P ratios in coastal waters the key to increased red tide blooms?, pp. 141-147, Springer.
Hu, C.M., Muller-Karger, F.E. and Swarzenski, P.W. (2006) Hurricanes, submarine groundwater discharge, and Florida's red tides. Geophysical Research Letters 33(11).
Hu, W.F., Lo, W., Chua, H., Sin, S.N. and Yu, P.H.F. (2001) Nutrient release and sediment oxygen demand in a eutrophic land-locked embayment in Hong Kong. Environment International 26(5-6), 369-375.
Hwang, D.W., Kim, G., Lee, W.C. and Oh, H.T. (2010) The role of submarine groundwater discharge (SGD) in nutrient budgets of Gamak Bay, a shellfish farming bay, in Korea. Journal of Sea Research 64(3), 224-230.
Hwang, D.W., Kim, G.B., Lee, Y.W. and Yang, H.S. (2005) Estimating submarine inputs of

groundwater and nutrients to a coastal bay using radium isotopes. Marine Chemistry 96(1-2), 61-71.

Jiao, J.J., Ding, G. and Leung, C.-M. (2006) Confined groundwater near the rockhead in igneous rocks in the Mid-Levels area, Hong Kong, China. Engineering geology 84(3), 207-219.

Johannesson, K.H., Chevis, D.A., Burdige, D.J., Cable, J.E., Martin, J.B. and Roy, M. (2011) Submarine groundwater discharge is an important net source of light and middle REEs to coastal waters of the Indian River Lagoon, Florida, USA. Geochimica Et Cosmochimica Acta 75(3), 825-843.

Kawakami, H. and Kusakabe, M. (2008) Surface water mixing estimated from ^{228}Ra and ^{226}Ra in the northwestern North Pacific. Journal of Environmental Radioactivity 99(8), 1335-1340.

Kim, G., Burnett, W.C., Dulaiova, H., Swarzenski, P.W. and Moore, W.S. (2001) Measurement of Ra-224 and Ra-226 activities in natural waters using a radon-in-air monitor. Environmental Science & Technology 35(23), 4680-4683.

Kim, G., Kim, J.S. and Hwang, D.W. (2011) Submarine groundwater discharge from oceanic islands standing in oligotrophic oceans: Implications for global biological production and organic carbon fluxes. Limnology and Oceanography 56(2), 673-682.

Kim, G., Ryu, J.W., Yang, H.S. and Yun, S.T. (2005) Submarine groundwater discharge (SGD) into the Yellow Sea revealed by Ra-228 and Ra-226 isotopes: Implications for global silicate fluxes. Earth and Planetary Science Letters 237(1-2), 156-166.

Kim, I. and Kim, G. (2011) Large fluxes of rare earth elements through submarine groundwater discharge (SGD) from a volcanic island, Jeju, Korea. Marine Chemistry 127(1-4), 12-19.

Kiro, Y., Weinstein, Y., Starinsky, A. and Yechieli, Y. (2013) Groundwater ages and reaction rates during seawater circulation in the Dead Sea aquifer. Geochimica Et Cosmochimica Acta 122, 17-35.

Krest, J.M., Moore, W.S., Gardner, L.R. and Morris, J.T. (2000) Marsh nutrient export supplied by groundwater discharge: Evidence from radium measurements. Global Biogeochemical Cycles 14(1), 167-176.

Krishnaswami, S., Graustein, W.C., Turekian, K.K. and Dowd, J.F. (1982) Radium, Thorium and Radioactive Lead Isotopes in Groundwaters - Application to the Insitu Determination of Adsorption-Desorption Rate Constants and Retardation Factors. Water Resources Research 18(6), 1663-1675.

Ku, T.-L., Luo, S., Leslie, B. and Hammond, D. (1992) Uranium-series disequilibrium: applications to earth, marine, and environmental sciences. 2. ed.

Ku, T.L. and Luo, S. (1992) Uranium Series DisequilibriumApplications to Earth, Marine and Environmental Sciences. M. Ivanovich, R.S.H. (ed), pp. pp. 631-668, Clarendon Press, Oxford.

Lee, C.M., Jiao, J.J., Luo, X. and Moore, W.S. (2012) Estimation of submarine groundwater discharge and associated nutrient fluxes in Tolo Harbour, Hong Kong. Science of the Total Environment 433, 427-433.

Lee, J.H.W. and Arega, F. (1999) Eutrophication dynamics of Tolo Harbour, Hong Kong. Marine Pollution Bulletin 39(1-12), 187-192.

Lee, J. M. and G. Kim (2006). "A simple and rapid method for analyzing radon in coastal and ground waters using a radon-in-air monitor." Journal of Environmental Radioactivity 89(3): 219-228.

Lee, Y.W. and Kim, G. (2007) Linking groundwater-borne nutrients and dinoflagellate red-tide outbreaks in the southern sea of Korea using a Ra tracer. Estuarine Coastal and Shelf Science 71(1-2), 309-317.

Lee, Y.W., Kim, G., Lim, W.A. and Hwang, D.W. (2010) A relationship between submarine

groundwater-borne nutrients traced by Ra isotopes and the intensity of dinoflagellate red-tides occurring in the southern sea of Korea. Limnology and Oceanography 55(1), 1-10.

Li, L., Barry, D., Stagnitti, F. and Parlange, J.Y. (1999) Submarine groundwater discharge and associated chemical input to a coastal sea. Water Resources Research 35(11), 3253-3259.

Liu, Q., Dai, M., Chen, W., Huh, C. A., Wang, G., Li, Q., & Charette, M. A. (2012). How significant is submarine groundwater discharge and its associated dissolved inorganic carbon in a river-dominated shelf system?. Biogeosciences, 9(5), 1777.

Luo, S.D., Ku, T.L., Roback, R., Murrell, M. and McLing, T.L. (2000) In-situ radionuclide transport and preferential groundwater flows at INEEL (Idaho): Decay-series disequilibrium studies. Geochimica Et Cosmochimica Acta 64(5), 867-881.

Luo, X. and Jiao, J.J. (2016) Submarine groundwater discharge and nutrient loadings in Tolo Harbor, Hong Kong using multiple geotracer-based models, and their implications of red tide outbreaks. Water Research 102, 11-31.

Luo, X., Jiao, J.J., Moore, W. and Lee, C.M. (2014) Submarine groundwater discharge estimation in an urbanized embayment in Hong Kong via short-lived radium isotopes and its implication of nutrient loadings and primary production. Marine Pollution Bulletin 82(1), 144-154.

Luo, X., Jiao, J. J., Wang, X. S., & Liu, K. (2016). Temporal ^{222}Rn distributions to reveal groundwater discharge into desert lakes: Implication of water balance in the Badain Jaran Desert, China. Journal of Hydrology, 534, 87-103.

Luo, X., Jiao, J. J., Wang, X. S., Liu, K., Lian, E., & Yang, S. (2017). Groundwater discharge and hydrologic partition of the lakes in desert environment: Insights from stable $^{18}O/^{2}H$ and radium isotopes. Journal of Hydrology, 546, 189-203.

McDonnell, J.J. (1990) A rationale for old water discharge through macropores in a steep, humid catchment. Water Resour. Res 26(11), 2821-2832.

Moore, W.S. (1976) Sampling radium-228 in the deep ocean. Deep Sea Res. 23, 647-651.

Moore, W.S. (1996) Large groundwater inputs to coastal waters revealed by Ra-226 enrichments. Nature 380(6575), 612-614.

Moore, W.S. (1999) The subterranean estuary: a reaction zone of ground water and sea water. Marine Chemistry 65(1-2), 111-125.

Moore, W.S. (2000) Ages of continental shelf waters determined from Ra-223 and Ra-224. Journal of Geophysical Research-Oceans 105(C9), 22117-22122.

Moore, W.S. (2003) Sources and fluxes of submarine groundwater discharge delineated by radium isotopes. Biogeochemistry 66(1-2), 75-93.

Moore, W.S. (2008) Fifteen years experience in measuring Ra-224 and Ra-223 by delayed-coincidence counting. Marine Chemistry 109(3-4), 188-197.

Moore, W.S. (2010) The effect of submarine groundwater discharge on the ocean. Ann Rev Mar Sci 2, 59-88.

Moore, W.S. and Arnold, R. (1996) Measurement of Ra-223 and Ra-224 in coastal waters using a delayed coincidence counter. Journal of Geophysical Research-Oceans 101(C1), 1321-1329.

Moore, W.S., Blanton, J.O. and Joye, S.B. (2006) Estimates of flushing times, submarine groundwater discharge, and nutrient fluxes to Okatee Estuary, South Carolina. Journal of Geophysical Research-Oceans 111(C9).

Mulligan, A. E. and M. A. Charette (2006). "Intercomparison of submarine groundwater discharge estimates from a sandy unconfined aquifer." Journal of Hydrology 327(3): 411-425.

Moore, W.S., Sarmiento, J.L. and Key, R.M. (2008) Submarine groundwater discharge revealed by Ra-228 distribution in the upper Atlantic Ocean. Nature Geoscience 1(5), 309-311.

Moore, D. G. and M. R. Scott (1986). "Behavior of ^{226}Ra in the Mississippi River mixing zone." Journal of Geophysical Research: Oceans (1978–2012) 91(C12): 14317-14329.

Nielsen, P. (1990) Tidal dynamics of the water table in beaches. Water Resources Research 26(9), 2127-2134.

Paerl, H. and Fogel, M. (1994) Isotopic characterization of atmospheric nitrogen inputs as sources of enhanced primary production in coastal Atlantic Ocean waters. Marine Biology 119(4), 635-645.

Paerl, H.W. (1997) Coastal eutrophication and harmful algal blooms: Importance of atmospheric deposition and groundwater as" new" nitrogen and other nutrient sources. Limnology and Oceanography 42(5), 1154-1165.

Pearce, A., Stewart, M. and Sklash, M. (1986) Storm runoff generation in humid headwater catchments: 1. Where does the water come from? Water Resources Research 22(8), 1263-1272.

Peterson, R.N., Burnett, W.C., Taniguchi, M., Chen, J.Y., Santos, I.R. and Ishitobi, T. (2008) Radon and radium isotope assessment of submarine groundwater discharge in the Yellow River delta, China. Journal of Geophysical Research-Oceans 113(C9).

Porcelli, D. (2008) Investigating groundwater processes using U-and Th-series nuclides. Radioactivity in the Environment 13, 105-153.

Prieto, C. and G. Destouni (2011). "Is submarine groundwater discharge predictable?" Geophysical Research Letters 38.

Raanan, H., Vengosh, A., Paytan, A., Nishri, A. and Kabala, Z. (2009) Quantifying saline groundwater flow into a freshwater lake using the Ra isotope quartet: A case study from the Sea of Galilee (Lake Kinneret), Israel. Limnology and Oceanography 54(1), 119.

Robinson, C., Li, L. and Barry, D. (2007) Effect of tidal forcing on a subterranean estuary. Advances in Water Resources 30(4), 851-865.

Ruxton, B.P. (1957) Weathering of Granite and Associated Erosional Features in Hong Kong, New York.

Santos, I.R., Eyre, B.D. and Huettel, M. (2012) The driving forces of porewater and groundwater flow in permeable coastal sediments: A review. Estuarine, Coastal and Shelf Science 98(0), 1-15.

Santos, I.R., Lechuga-Deveze, C., Peterson, R.N. and Burnett, W.C. (2011) Tracing submarine hydrothermal inputs into a coastal bay in Baja California using radon. Chemical Geology 282(1-2), 1-10.

Santos, I.R., Peterson, R.N., Eyre, B.D. and Burnett, W.C. (2010) Significant lateral inputs of fresh groundwater into a stratified tropical estuary: Evidence from radon and radium isotopes. Marine Chemistry 121(1-4), 37-48.

Shaw, R. (1992) Seabed sediment distribution in hong kong waters. Civil Engineering Department, H.K. (ed), p. 12, Geological Report.

Slomp, C.P. and Van Cappellen, P. (2004) Nutrient inputs to the coastal ocean through submarine groundwater discharge: controls and potential impact. Journal of Hydrology 295(1), 64-86.

Su, N., Du, J., Li, Y. and Zhang, J. (2013a) Evaluation of surface water mixing and associated nutrient fluxes in the East China Sea using ^{226}Ra and ^{228}Ra. Marine Chemistry.

Su, N., Du, J., Liu, S. and Zhang, J. (2013b) Nutrient fluxes via radium isotopes from the coast to offshore and from the seafloor to upper waters after the 2009 Spring Bloom in the Yellow Sea. Deep Sea Research Part II: Topical Studies in Oceanography.

Swarzenski, P.W., Reich, C., Kroeger, K.D. and Baskaran, M. (2007) Ra and Rn isotopes as natural tracers of submarine groundwater discharge in Tampa Bay, Florida. Marine Chemistry 104(1-2), 69-84.

Tse, K.C. and Jiao, J.J. (2008) Estimation of submarine groundwater discharge in Plover Cove,

Tolo Harbour, Hong Kong by Rn-222. Marine Chemistry 111(3-4), 160-170.

Wai, K.-M., Leung, K.-Y. and Tanner, P.A. (2010) Observational and modeling study of dry deposition on surrogate surfaces in a South China city: implication of removal of atmospheric crustal particles. Environmental Monitoring and Assessment 164(1-4), 143-152.

Wai, K., Tanner, P. and Tam, C. (2005) 2-year study of chemical composition of bulk deposition in a South China coastal city: comparison with East Asian cities. Environmental Science & Technology 39(17), 6542-6547.

Wang, X., Li, H., Jiao, J.J., Barry, D.A., Li, L., Luo, X., Wang, C., Wan, L., Wang, X. and Jiang, X. (2015a) Submarine fresh groundwater discharge into Laizhou Bay comparable to the Yellow River flux. Scientific reports 5, 8814.

Wang, X., Li, H., Luo, X., Jiao, J., Qu, W. and Wang, C. (2015b) Using ^{224}Ra to estimate eddy diffusivity and submarine groundwater discharge in Laizhou Bay, China. Journal of Radioanalytical and Nuclear Chemistry, 1-9.

Wang, X., Wu, Z., Shao, M., Fang, Y., Zhang, L., Chen, F., Chan, P.-W., Fan, Q., Wang, Q. and Zhu, S. (2013) Atmospheric nitrogen deposition to forest and estuary environments in the Pearl River Delta region, southern China. Tellus Series B-Chemical and Physical Meteorology 65.

Wilson, A.M. (2005) Fresh and saline groundwater discharge to the ocean: a regional perspective. Water Resources Research 41(2).

Wilson, A.M., Evans, T., Moore, W., Schutte, C.A. and Joye, S.B. (2015) What time scales are important for monitoring tidally influenced submarine groundwater discharge? Insights from a salt marsh. Water Resources Research.

Xu, F.L., Lam, K.C., Zhao, Z.Y., Zhan, W., Chen, Y.D. and Tao, S. (2004) Marine coastal ecosystem health assessment: a case study of the Tolo Harbour, Hong Kong, China. Ecological Modelling 173(4), 355-370.

Yung, Y.-K., Wong, C., Broom, M., Ogden, J., Chan, S. and Leung, Y. (1997) Long-term changes in hydrography, nutrients and phytoplankton in Tolo Harbour, Hong Kong, pp. 107-115, Springer.

New Development in Statistical Landslide Hazard Analysis

Chyi-Tyi Lee
Graduate Institute of Applied Geology, National Central University

Abstract: A multi-temporal landslide inventory was commonly used in training a rain-induced landslide susceptibility/hazard model previously. However, there still are problems on incompleteness of the inventory, insufficient length of historical records, and a possible mixing of extreme storm events and/or earthquake disturbance in many countries. The present study introduces an event-based landslide susceptibility model proposed by Lee et al. (2008a) and a new probability of failure relationship to accommodate the spatial probability of landslide failure with rainfall variables and event-independent landslide susceptibility (basic susceptibility). This study selects a typhoon event landslide inventory in the Kaoping River basin in southern Taiwan as training data set to perform an event-based landslide susceptibility analysis. A probability of failure analysis is followed to establish a relationship among rainfall, probability of failure, and the basic susceptibility, so that probability of landslide failure at each point can be got, providing rainfall and susceptibility values are known. At the same time, a rainfall frequency analysis in the study area is done. At last, an integrated hazard analysis in which a certain return-period rainfall and the basic susceptibility are input into the model, and a certain return-period landslide hazard map is completed.

INTRODUCTION

In the previous studies, most landslide hazard maps are still of a qualitative nature and concentrate basically on determining the susceptibility (e.g., van Westen et al., 2006), and temporal probability is lacking. Guzzetti et al. (2005) attempt to solve the temporal probability problem and introduced a probabilistic model which predicts where landslides will occur, how frequently they will occur, and how large they will be. However, there still are problems on incompleteness of the multi-temporal landslide inventory, insufficient length of historical records, and a possible mixing of extreme events and/or earthquake disturbance.

Physical based method uses a hydrological model and an infinite slope model to form a landslide prediction model with parameters pre-calibrated by a set of landslide data (Montgomery and Dietrich, 1994; Iverson, 2000; Brenning, 2005; Claessenset al., 2007). It is perfect in theory, but has a difficulty in acquiring site specific data, like, failure depth, material strength, and hydrological data.

Landslide inventory from single period of aerial photos is not valid for training a landslide susceptibility model (e.g., Canuti and Focardi, 1986). Single-period landslide inventory for susceptibility analysis is biased. However, a new statistical approach called event-based landslide susceptibility analysis was introduced recently in Lee et al. (2008a). This new approach is different from the traditional susceptibility analyses in the emphasis of using an event landslide inventory and triggering factors. It is also different from the Guzzetti's probabilistic method in the usage of event landslide inventory and triggering factors vs. the usage of multi-temporal landslide inventory. The event-based landslide susceptibility analysis method also is applicable to model the earthquake-induced landslides (Lee et al., 2008b).

Although both using an event landslide inventory, the event-based landslide susceptibility

analysis is basically different from the physically based method. But they are similar in the multi-stage nature, with including a susceptibility stage for spatial probability of landslides and a rainfall frequency analysis stage for temporal probability of landslides, and both intend to construct a landslide spatial probability or safety factor map for a certain retain-period rainfalls. This means both methods adopt that recurrence of rainfall-induced landslide is controlled by the repetition of triggering events.

The present study upgrades the study of Lee et al. (2008a) by developing a probability of failure surface instead of a probability of failure curve. The new relationship should avoid mixing the contribution from causative factors (Lee, 2014a, 2014b). Using this new probability of failure surface and a 100-year return-period rainfall map, a new 100-year storm landslide hazard map for a major river basin in southern Taiwan is constructed. The rainfall landslide hazard map may reveal landslide spatial probability at each pixel given a certain rainfall return-period.

METHODOLOGY

Susceptibility Model

The method basically follows Lee et al. (2008a) which used an event landslide inventory and the triggering factors to build a susceptibility model. When event landslide inventory and triggering factors are used in building a susceptibility model, the susceptibility model is dependent on the event itself. However, if we extract the component of the triggering factors from the model, then the model becomes event independent, provided that the triggering variable is an independent factor having only small correlation coefficient with each causative factor.

An event-independent susceptibility model is a common model having similar susceptibility pattern at a region as discussed in Lee et al. (2004) and in a recent studies (Lee and Chung, 2017). Different event-independent susceptibility model for the same region are similar in pattern, and is similar also to a susceptibility model built by a multi-temporal landslide inventory at that region (Fig. 1). On this basis, we can use an event-independent susceptibility model to represent the susceptibility of the region with confidence. Here, we regard the event-independent susceptibility of a region as "basic susceptibility" of that region.

Probability of Failure Surface

The construction of a probability of failure curve in the previous studies is simple, that simply plots the mean probability of failure value (percentage of failure grids to total grids) at each susceptibility bin and fit a curve. A landslide spatial probability map may be produced by transferring the susceptibility values to the probability of landslide failure at each grid-cell by using a probability of failure curve.

A probability of failure surface is intended to show a relationship between the probability of failure and rainfall parameters at each susceptibility bin, and to obtain the fit to the surface using the rainfall parameters and basic susceptibility as independent variables. Using this relationship, landslide probability map may be produced, if a scenario rainfall event or return-period rainfalls is given.

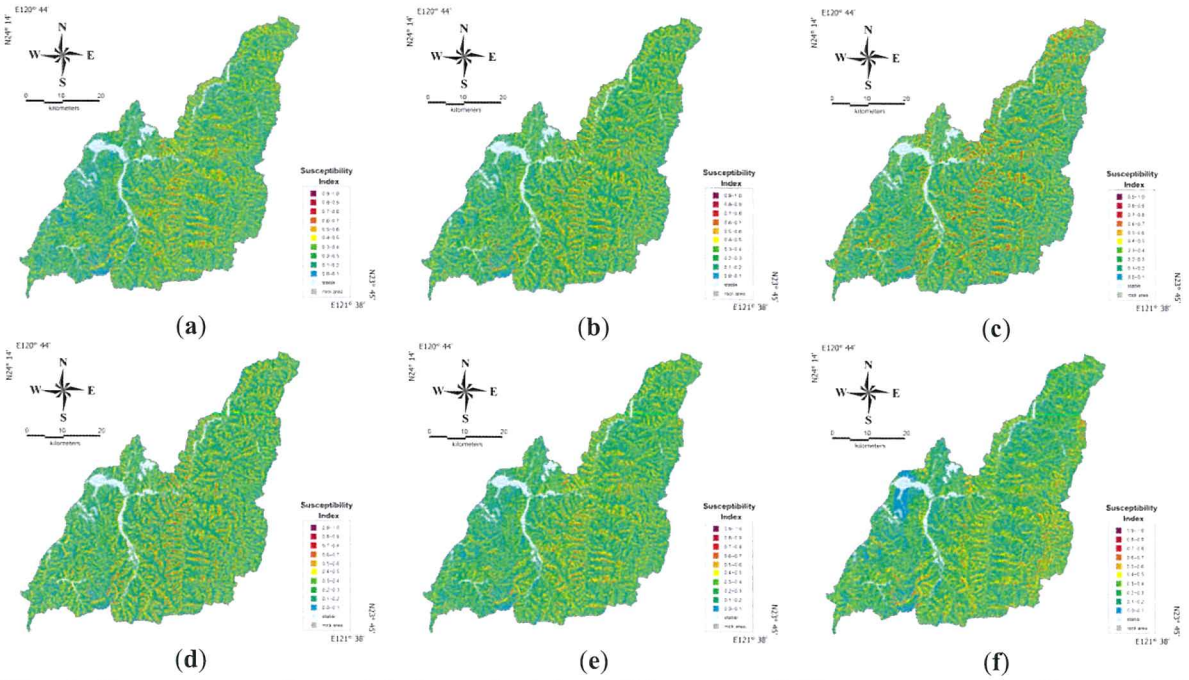

Fig. 1 Comparison of event-independent landslide susceptibility maps at the Choswei River catchment in Central Taiwan, (a) trained from typhoon Toraji data, (b) trained from typhoon Mindulle data, (c) trained from typhoon Shinlaku data, (d) trained from typhoon Morakot data, (e) trained from combined typhoon Toraji and Midulle data, (f) trained from a multi-temporal landslide inventory.

Temporal Probability of Landslides

Since rainfall landslides are induced features from the heavy rainfall, their recurrence is controlled by the repetition of the rainfall event. Therefore, we must know the likelihood of a rainfall recurrence or the rainfall values at a certain return-period. This may be obtained through a regular hydrological frequency analysis (e.g., Chow, 1953, Fowler and Kilsby, 2003) with a set of rainfall data from different rain gauge stations.

A certain return-period rainfall intensity map, 1-hour rainfall map, and 3-day rainfall map for the study region is the objective of the frequency analysis, and is the input data for the rainfall landslide hazard mapping. This is commonly a 100-year return period rainfall. However, it may be other choices of return period, like a 50-year return period. If rainfalls of a 100-year return-period are used, the hazard map reflects the 100-year rainfall, and may be called a 100-year rainfall landslide hazard map.

APPLICATION

An example of event-based statistical landslide hazard analysis is selected at the Kaoping River basin, southern Taiwan, for demonstration.

Regional Setting

The Kaoping River basin is the largest drainage basin in southern Taiwan (Fig. 2). It has a catchment area of 3,333 km^2. Elevations in the watershed range from 135 m in the south to the submit of Yushan mountain of 3,952 m in the north, with generally rugged topography. Slopes with gradient greater than 55% covers 61% of the catchment area, slopes gradient of 30~55% occupies 29% area, only 10% is gentle slopes with gradient less than 30%. Rocks are composed of folded and faulted Miocene sandstone and mudrocks at the west, and Paleogene

argillite and slate at the east. Terrace deposits on the river sides are composed of sandy gravels. Slopes are commonly mantled by shallow slope washes or colluvium. Nearly 90% of the study area is forested. The climate is influenced by typhoons in summer and is dry in winter. The mean annual temperature is 20°C, with a mean monthly temperature of 27.5 °C in July and 14.2 °C in January. The annual precipitation averages 2,370 mm. Because of the visiting of typhoons, large rainfall events usually happen from May to September.

From July 16 to 20, 2005, typhoon Haitang crossed the southern part of Taiwan. The passage of typhoon Haitang brought a maximum recorded rainfall of 2,000 mm and a maximum rainfall intensity of 106 mm/hr in the study area. During the typhoon, it triggered 15,864 landslides with a total area of 42.8 Km^2, which occupied 1.28% area of the river basin, or 1.75% of the slope terrain in the river basin.

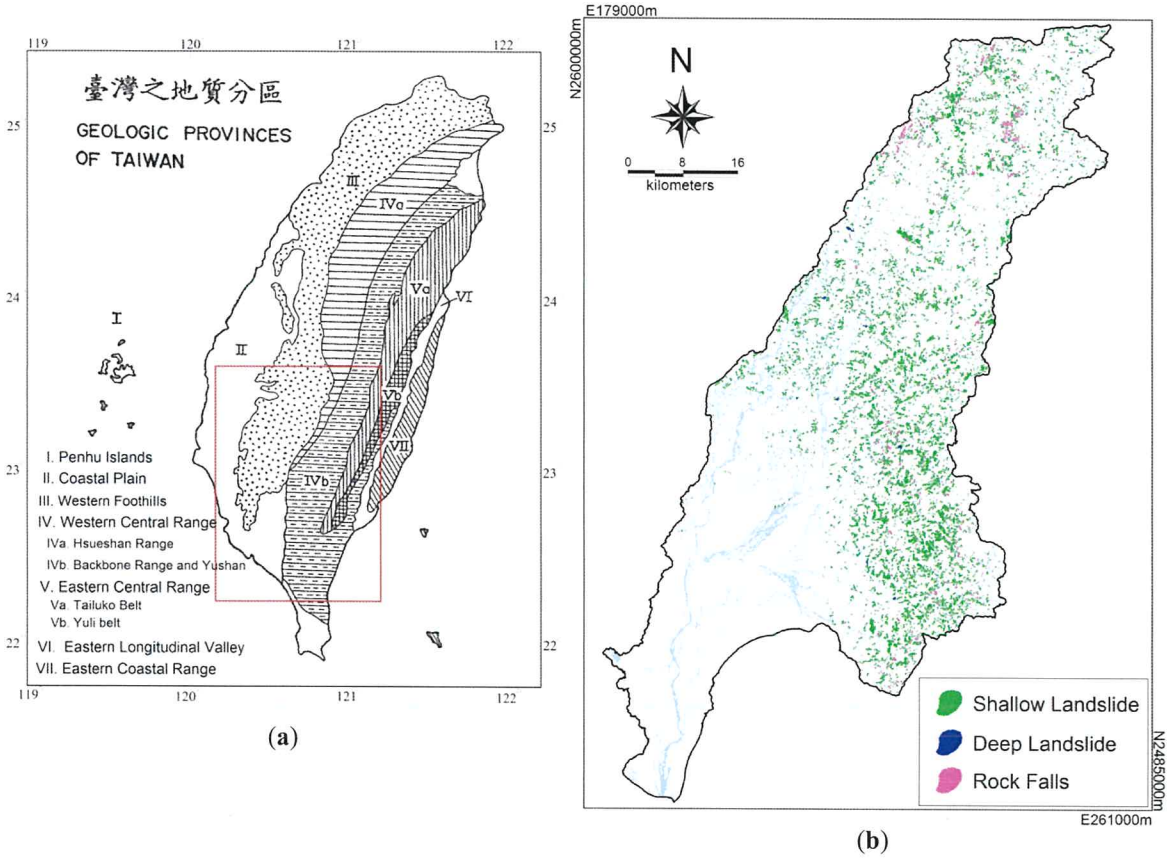

Fig. 2 Geology and landslides in the study area, (a) geology of Taiwan and index map, (b) landslides triggered by the typhoon Haitang in the Kaoping River basin.

Data Acquisition

The basic data used in the present study include: 2.5m high resolution SPOT5 images, a 5-m grid digital elevation model (DEM), 1/5,000 photo-based contour maps, 1:50,000 geologic maps, and hourly rainfall records. Digital geological maps (1:50,000) were obtained from the Central Geological Survey (CGS), Taiwan. All the vector layers were converted into raster cells of 10m x 10m in size and this resolution was used for all subsequent processing and analysis for each landslide factor and the hazard model.

Event Landslide Inventory

False-color SPOT5 images were used for landslide recognition. Landslides were recognized and digitized in GIS and attributes assigned to establish a landslide map table. Each landslide table was then checked in the field and also in the laboratory against 1/5,000 photo-based

contour maps, and modifications were made. An event-triggered landslide was identified by comparing the pre-event and post-event landslide inventories, to produce an event landslide inventory. The typhoon Haitang event landslide inventory is shown in Fig. 2b. The event landslide inventory for the 2009 typhoon Morakot was prepared in a similar way and will be used for validation.

Causative Factors

In the present study, we first selected more than sixteen of the most frequently used ones, based on data abundance and availability. These factors were further tested, including the normality of each factor, standardized differences (Davis, 2002) between the landslide group and non-landslide group for each factor, probability of failure curve, success rate curve (Fig. 3), and the correlation coefficient between any two factors. A final selection of effective factors was decided based upon the evaluation and test results. In this study, six causative factors: lithology, slope gradient, slope aspect, slope roughness, tangential curvature, relative slope height, and a triggering factor - maximum rainfall intensity, were selected for building the susceptibility model.

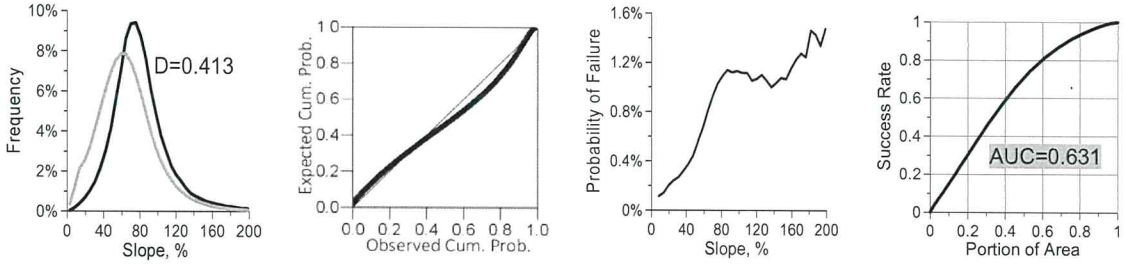

Fig. 3 Selection of an effective factor using slope gradient as example. (a) Frequency distribution curves and standardized difference between landslide group (dark line) and non-landslide group (gray line), (b) P-P plot for testing of normal distribution, (c) Probability of failure curve showing larger slope correlating to higher probability of landslide failure, (d) Success rate curve showing the factor could successfully interpret landslides.

The 9 selected factors are described as follows:

(1) Lithology: Lithologic units were reduced from the 1 to 50,000 scale geological sheet map of CGS. These include 11 different units denoted as L_1~L_{11} in the model: sand and gravel deposits (L_1), Linko Conglomerate (L_2), Liukui Formation (L_3), Gutingkeng Formation (L_4), Nanshihlun Sandstone (L_5), Kaitzuliao Shale (L_6), Lushan Formation (L_7), Sanmin Shale (L_8), Giayang Formation (L_9), Dachian Sandstone (L_{10}), and metamorphic complex (L_{11}), Alluvium and diluvium are present at flat area and were classified into stable area, which was not included in the analysis.

(2) Slope gradient: Slope is the first derivative of topographic surface. Following Wilson & Gallant (2000), we used 3×3 subgrid to calculate slope gradient from grid DEM in Erdas Imagine system.

(3) Slope aspect: on the way of slope gradient calculation, slope aspect of each 3×3 subgrid was done. The slope aspects were further divided into 8 groups from A_1 ro A_8, representing N, NE, E, SE, S, SW, W, and NW.

(4) Slope roughness: Referring to Wilson & Gallant (2000), we used 13×13 subgrid to calculate the standard deviation of slope gradient and used this standard deviation as slope roughness.

(5) Tangential curvature: Curvature is the second derivative of topographic surface. It may be classified as profile curvature, plane curvature, tangential curvature, and total curvature. We

used 3×3 subgrid to calculate tangential curvature from a 13×13 subgrid smoothed DEM in Erdas Imagine system. Using a smoothed DEM is to reduce local topographic effect.

(6) Relative slope height: Height difference from point of interest to toe is defined as "slope height". Slope height divided by total slope height is defined as "relative slope height".

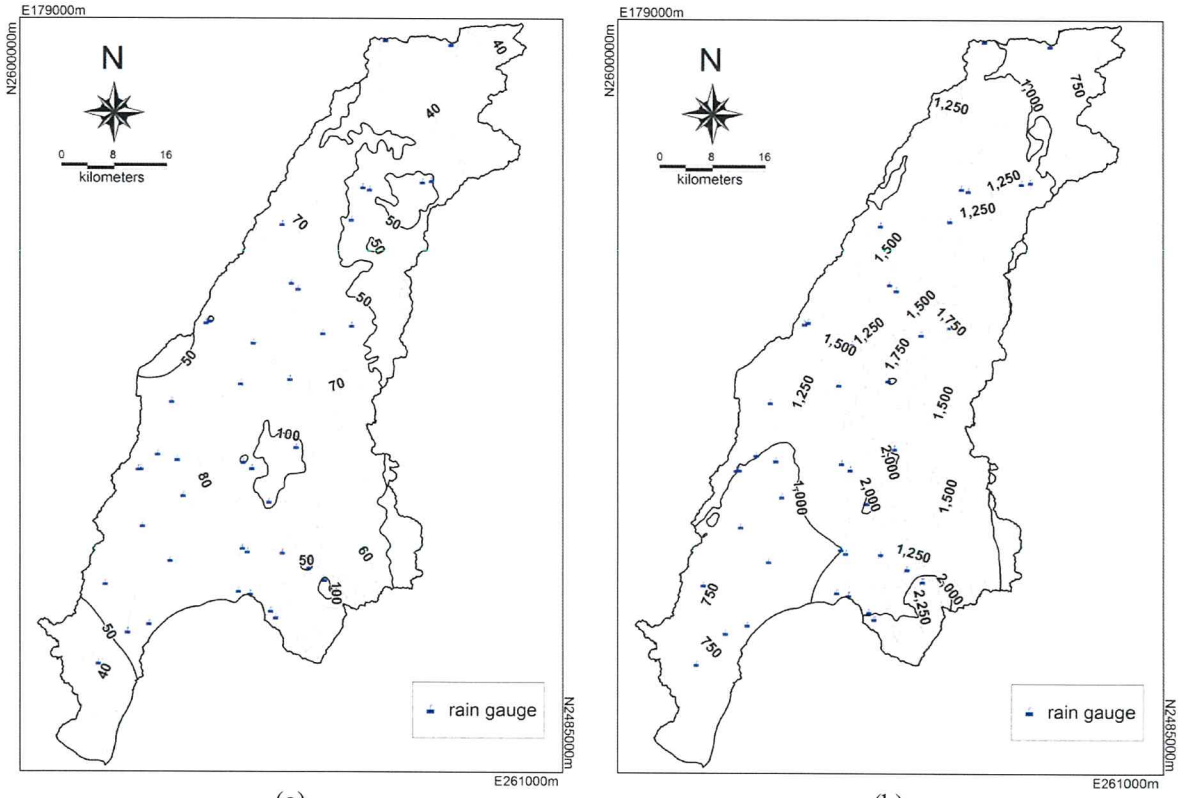

Fig. 4 Rainfall map for the typhoon Haitang, (a) rainfall intensity in mm/hr, (b) event total rainfall.

Triggering Factors

Maximum rainfall intensity: There are 44 rain gauge stations in the catchment area. We first processed these 44 stations and more stations around the catchment area to obtain the maximum rainfall intensity and total rainfalls for each station. Then we used these parameters and incorporate topographic heights as auxiliary variables to perform spatial interpolation at each grid-cell using kriging with varying local means. Results are shown in Fig. 4. Maximum rainfall intensity was finally selected as an effective triggering factor for building the susceptibility model.

Event-based Susceptibility Model

The typhoon Haitang induced shallow landslides (Fig. 2b) and rainfall data (Fig. 4) are actually used in the susceptibility analysis. Causative factors used in the susceptibility model include the following: lithologic units (L_1-L_{11}), slope aspects (A_1-A_8), slope gradient (F_1), slope roughness (F_2), tangential curvature (F_3), and relative slope height (F_4). Triggering factor used in the susceptibility model is event total rainfall (F_5). All the factor scores are normalized before regression.

Logistic regression is used in the susceptibility analysis and the results of this analysis include a logistical function and the coefficients,

$$\ln\left[\frac{p}{1-p}\right] = \begin{aligned} &0.726L_1 + 0.175L_2 + 1.072L_3 + 3.673L_4 + 2.520L_5 + 2.575L_6 + \\ &2.856\,L_7 + 2.205L_8 + 3.044L_9 + 3.053L_{10} + 2.940\,L_{11} + 2.812A_1 + \\ &3.595A_2 + 4.146A_3 + 4.333A_4 + 4.240A_5 + 3.987A_6 + 3.297A_7 + \\ &2.790A_8 + 1.182F_1 + 0.061F_2 + 0.299F_3 - 0.761F_4 + 0.446F_5 - 7.317. \end{aligned} \quad [1]$$

where p is the occurrence probability. During the establishment of the logistic equations, the input p is 1 for a landslide grid and 0 for a non-landslide grid. After the regression, when the set of factor scores is given at a grid point, the occurrence probability p at that point is derived. It will be in the range of 0 to 1. This occurrence probability is taken as a susceptibility index λ in this study. Larger values of an index indicate a higher susceptibility to landslides.

The event-based susceptibility model (Fig. 5a) goes a good way to explaining the event-induced landslide distribution. The area under the curve (AUC) of the success rate curve is 0.776. The model is further validated utilizing the typhoon Morakot rainfalls and its event landslide inventory; the AUC of the prediction rate curve is 0.728 for the model.

Event Independent Susceptibility Model

The event-based susceptibility model is dependent on the event itself. However, if we extract the triggering factor from the model, then the model becomes event independent, provided that the triggering factor is an independent factor having only small correlation coefficient with any causative factors. This option must be carefully examined before a causative factor is selected.

In this case, the event-based susceptibility model is reduced to an event-independent model by removing the component of the triggering factor from the original model. Here, we call this reduced model an event-independent susceptibility model for the region. The event-independent susceptibility model for the study area is given in Fig. 5b. We use this as basic susceptibility of the study area for further analysis.

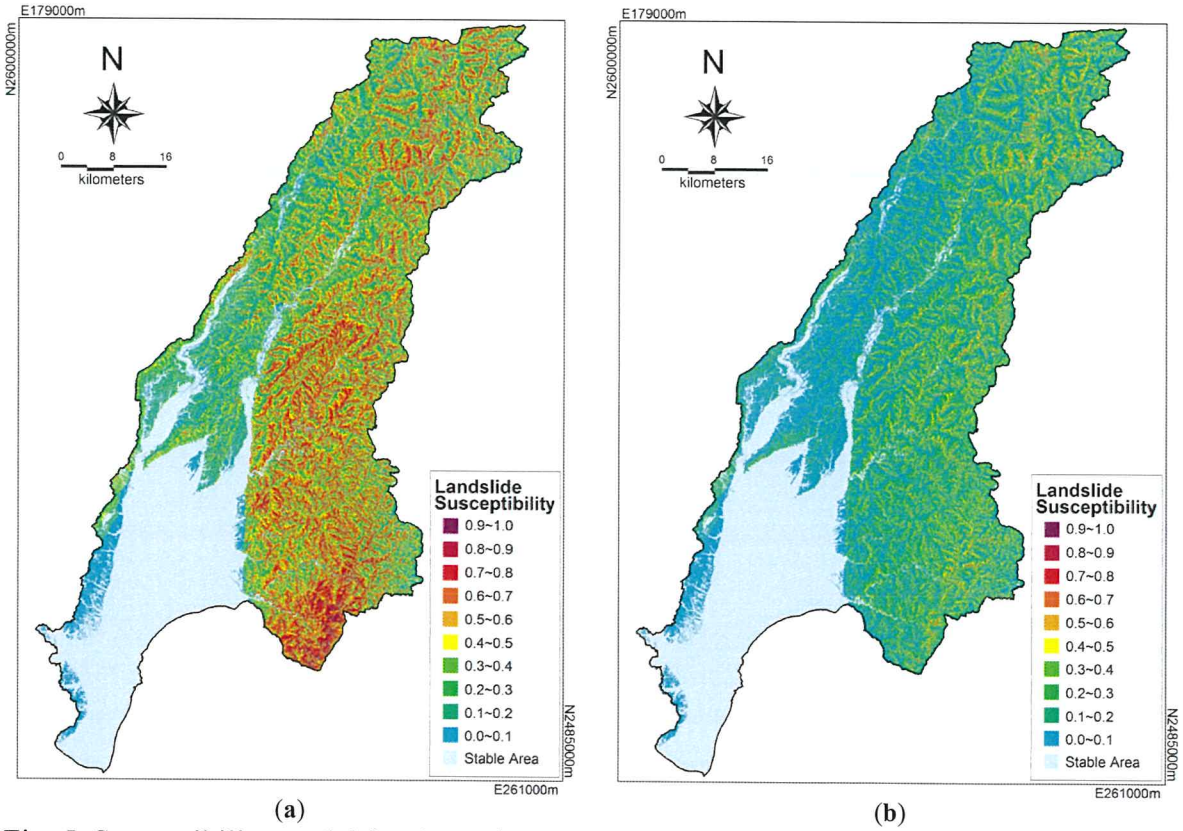

Fig. 5 Susceptibility model for the Haitang event landslides, (a) event-dependent landslide susceptibility map, (b) event-independent landslide susceptibility map.

Probability of Failure Surface

We established the relationship between probability of failure and rainfall intensity, as well as total rainfall at each basic bin at the first step. it was found that the relation is good; the probability of failure increases with an increase in the rainfalls and also with an increase in the susceptibility. After this finding, it was necessary to find a global fitting surface using a rainfall parameter and basic susceptibility as two independent variables. The result is shown in Fig. 6 and equations 2 and 3 as follows:

$$y = 26.849\lambda(1-e^{-3.740\lambda^{0.759}})(1-e^{-0.0324(\frac{x}{10})^{1.784}}) \quad [2]$$

$$y = 30.481\lambda(1-e^{-3.536\lambda^{0.734}})(1-e^{-0.0014(\frac{x}{100})^{2.411}}) \quad [3]$$

where x is the rainfall intensity (eq. 2) or event total rainfall (eq. 3); y is the probability of failure, and λ is the basic susceptibility.

A global probability of failure surface for two rainfall variables may be built by combining equations 2 and 3. If the two rainfall variables are totally independent, then the square of global probability of failure is the sum of the square of eq. 2 and the square of eq. 3. If the two rainfall variables are totally dependent, then the square of global probability of failure is the product of the eq. 2 and the eq. 3. In actual cases, the two rainfall variables are commonly in between dependent and independent, but have a correlation coefficient between 0 and 1. In the present study, we propose,

$$y = ((1-r)(y_1^{\,2} + y_2^{\,2}) + r(y_1 y_2))^{0.5}, \quad [4]$$

where y_1 is y of eq. 2, y_2 is y of eq. 3, and r is the correlation coefficient between rainfall intensity and total rainfall.

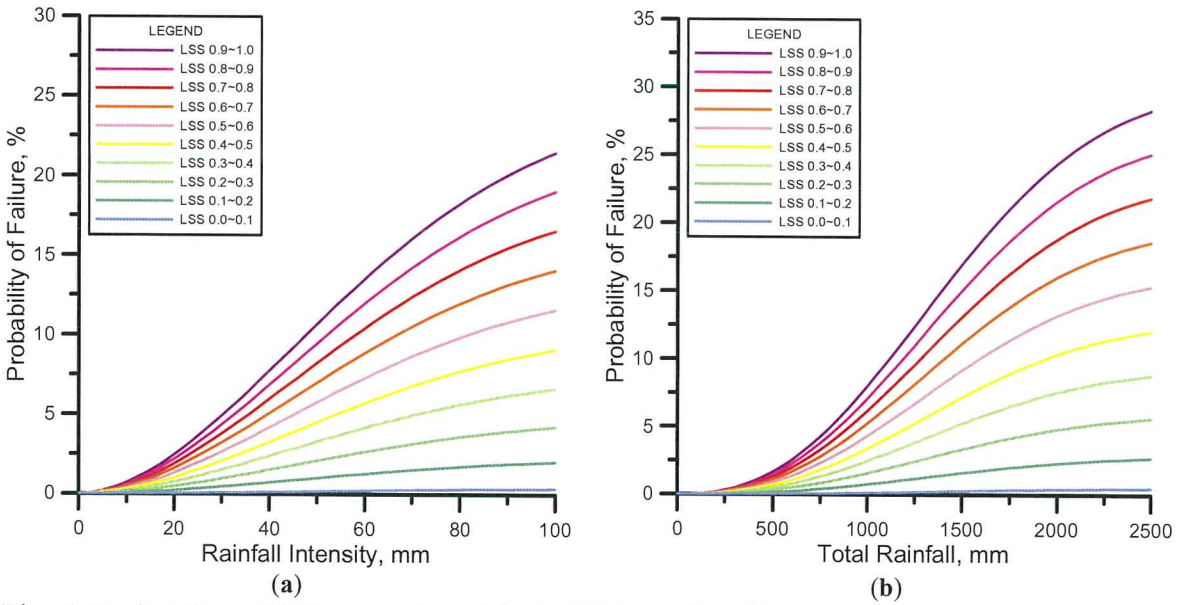

Fig. 6 Probability of failure surface, (a) rainfall intensity, (b) event total rainfall, equations are shown in the text.

Rainfall Frequency Analysis

The temporal probability of a rainfall landslide hazard model may be accounted for by the recurrence of the rainfall events. Rainfall values at different return-period may be obtained through a conventional rainfall frequency analysis.

A hydrological team in the CGS landslide project was responsible for rainfall frequency analysis and different return-period rainfall values are available at each rain gauge station. The present study selects 1-hour rainfalls and 3-day rainfalls of 100-year return-period for final mapping of the rainfall landslide hazard. 3-day rainfalls are evaluated as proper to represent the total rainfall of a Typhoon storm event in Taiwan.

Rainfall Landslide Hazard Map

An event-dependent susceptibility model is good only for interpretation of the event landslide distribution. With the addition of the probability failure surface, this model is capable of landslide prediction during a scenario event. However, for hazard mapping, a certain temporal probability or return period for rainfall values should be adopted. This is commonly a 100-year return period. Other choices of return period, like a 10-year, 20-year, 50-year return-period may also be used.

The 1-hour rainfall map and 3-day rainfall map of 100-year return-period (Fig. 7), and the basic susceptibility model (Fig. 5b) are then applied to the probability of failure model (eqs. 2, 3, and 4) to construct a 100-year rainfall landslide hazard map for the Kaoping River basin (Fig. 8).

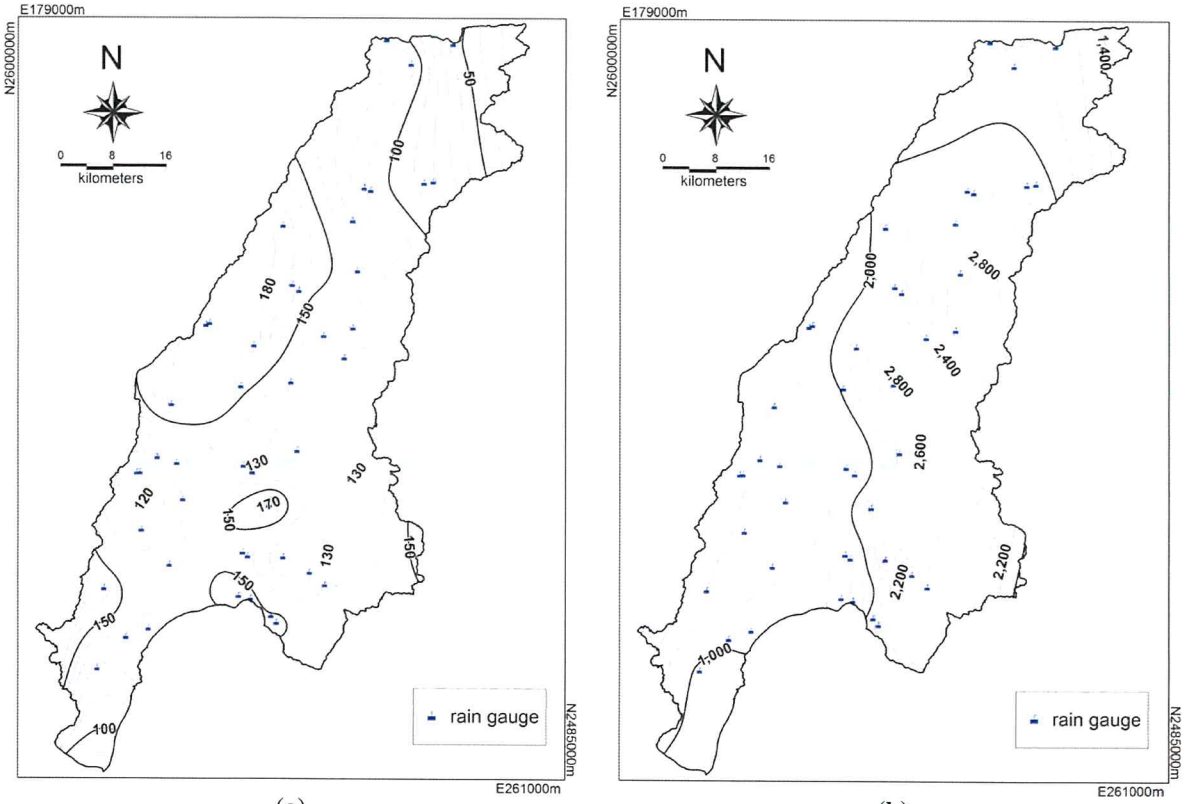

Fig. 7 100-year rainfall map for Taiwan, (a) rainfall intensity in mm/hr, (b) 3-day rainfall in mm.

CONCLUSIONS

A multivariate statistical approach with logistic regression has been used to analyse the typhoon Haitang induced shallow landslides and their controlling factors, and to build an event-dependent susceptibility model. The event-independent model (without a triggering factor), rainfall intensity map, total rainfall map, and the actual landslides from the Haitang event, are used to construct a relationship, using the event-independent susceptibility and

rainfall parameters as independent variables, and it is fitted with a probability of failure surface. Then, the 100-year rainfall maps together with the event-independent susceptibility model are input into the probability of failure relationship to complete a 100-year rainfall landslide hazard map for the Kaoping River basin. The results of the analysis are good, provided that careful validation of the typhoon Morakot induced landslides is made. We conclude that this statistical approach is feasible for rainfall landslide hazard analysis, and that the hazard model can be used to predict landslides after a rainfall event and can be used to produce a rainfall landslide hazard map of a wider region.

The statistical approach to rainfall landslide hazard has advantages over deterministic methods in that it does not require failure depth, material strength, or groundwater data, and may have a better prediction rate. On the other hand, a deterministic model can be used anywhere once the parameters required by the model are available. The statistical approach, in contrast, may be applicable only in the vicinity of the study region where the model was trained, and may be limited to within or near to the rainfall intensity range for which they were trained.

The present proposed hazard model is good for the prediction of landslide spatial probability during a rainfall event, the mapping of the rainfall landslide hazard probability for a certain return-period rainfall, decision making for regional planning, site selection, hazard mitigation, and the estimation of sediment products for a river basin after an extreme event. However there is still a lack of output in regards to the landslide magnitude which is very important in risk assessment. This problem needs further study.

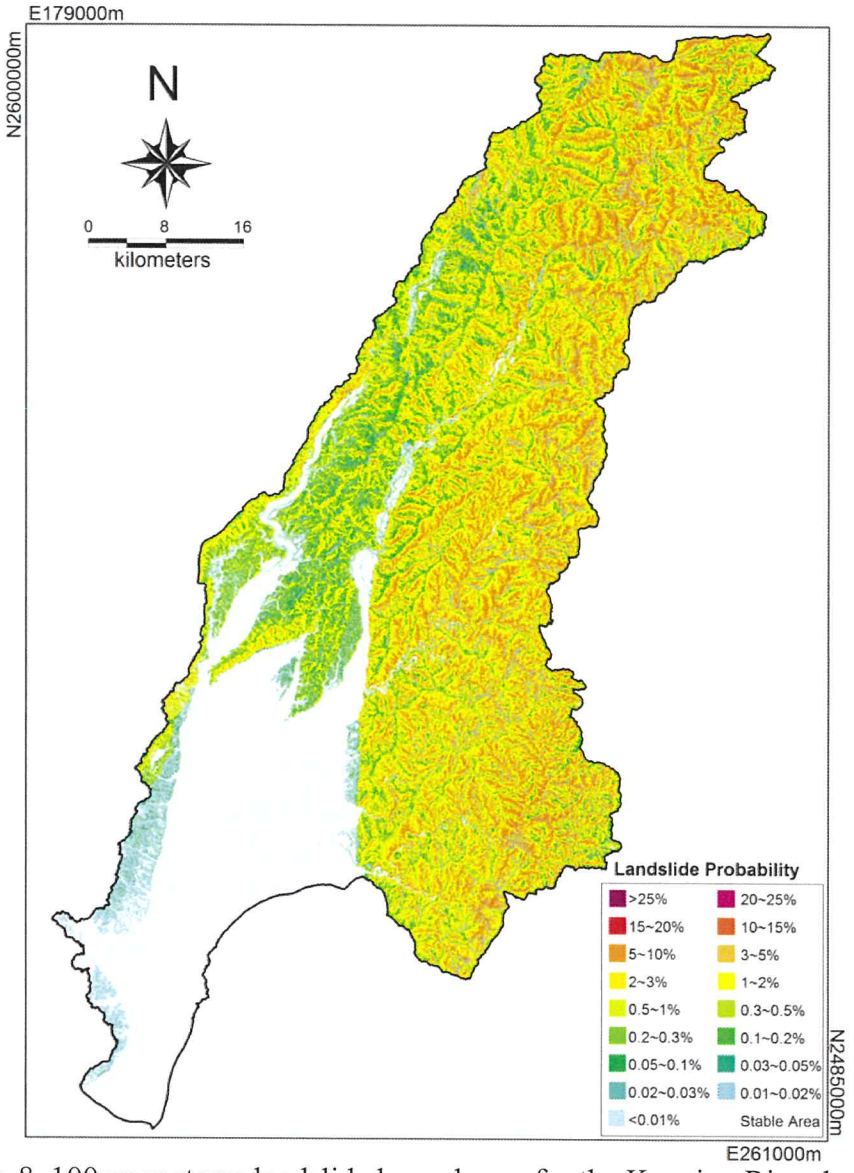

Fig. 8 100-year storm landslide hazard map for the Kaoping River basin

REFERENCES

Brenning, A (2005) Spatial prediction models for landslide hazards: review, comparison and evaluation. Natural Hazard and Earth System Sciences. 5(6): 853-862.

Canuti, P and Focardi, P (1986) Slope stability and landslides investigation in Tuscany. Mem. Geol. Soc. Italy, 31, 307-315.

Chow, V T (1953) Frequency analysis of hydrologic data with special application to rainfall intensities. University of Illinois Engineering Experiment Station, Bulletin Series, 414, 81p.

Claessens L, Schoorl J M, Veldkamp A (2007) Modelling the location of shallow landslides and their effects on landscape dynamics in large watersheds: an application for Northern New Zealand. Geomorphology. 87: 16-27.

Fowler H J, Kilsby C G (2003) A regional frequency analysis of United Kingdom extreme rainfall from 1961 to 2000. International Journal of Climatology. 23(11): 1313-1334.

Guzzetti F, Reichenbach P, Cardinali M, Galli M, Ardizzone F (2005) Probabilistic landslide hazard assessment at the basin scale. Geomorphology. 72: 272-299.

Iverson R M (2000) Landslide triggering by rain infiltration. Water Resources Research. 36:

1897-1910.
Lee, C.T. (2014a) Multi-stage statistical landslide hazard analysis: earthquake-induced landslides. In: Landslide Science for a Safer Geoenvironment, Sassa, K., Canuti, P., Yin, Y.Y., Ugai, K., Yagi, H., Wakai, A. (eds.), Springer International Publishing, 3, 205-211.
Lee, C.T. (2014b) Multi-stage statistical landslide hazard analysis: rain-induced landslides. In: Landslide Science for a Safer Geoenvironment, Sassa, K., Canuti, P., Yin, Y.Y., Ugai, K., Yagi, H., Wakai, A. (eds.), Springer International Publishing, 3, 291-298.
Lee, C.T., and Chung, C.C. (2017) Common patterns among different landslide susceptibility models of the same region. In: Advancing Culture of Living with Landslides, Mikos, M., Tiwari, B., Yin, Y.P., Sassa, K. (eds.), Springer International Publishing, 2, 937-942.
Lee C T, Huang C C, Lee J F, Pan K L, Lin M L, Dong J J (2008a) Statistical approach to storm event-induced landslide susceptibility. Natural Hazard and Earth System Sciences. 8: 941-960.
Lee C T, Huang C C, Lee J F, Pan K L, Lin M L, Dong J J (2008b) Statistical approach to earthquake-induced landslide susceptibility. Engineering Geology. 100: 43-58.
Lee C T, Huang C C, Lee J F, Pan K L, Lin M L., Liao C W, Lin P S, Lin Y S, Chang C W (2004) Landslide susceptibility analyses based on three different triggering events and result comparison, Proceeding of International Symposium on Landslide and Debris Flow Hazard Assessment, Taipei, pp. 6-1~6-18.
Montgomery D R, Dietrich W E (1994) A physical-based model for the topographic control on shallow landsliding. Water Resources Research. 30(4): 1153-1171.
Van Westen C J, van Asch T W J, Soeters R (2006) Landslide hazard and risk zonation - why is it still so difficult? Bulletin of Engineering Geology and Environment. 65: 167-184.

ACKNOWLEDGEMENTS

The comments from the Organizing Committee of the Geological Society of Hong Kong -35th Anniversary Conference 2017 are gratefully acknowledged.

Field Trip Information

Field trip on 18 November 2017 (Saturday)

Route A: High Island (Hong Kong Geopark) and Sai Wan Road (Natural Terrain Landslide Site)

Meeting point: **Front door of the City View, 23 Waterloo Road, Yau Ma Tei, Kowloon**

Gathering Time: **9:00 am**

Trip Leader: **Mr. Steven J Williamson (AECOM Asia Co. Ltd.)**

This trip will visit two locations, the East Dam of High Island Reservoir and a natural terrain landslide site at Sai Wan Road. Lunch is not included, so participants are recommended to bring their own pack lunch and sufficient amount of water. The group will dismiss at around 4:15pm.

The Hong Kong Geopark was first established as one of the National Geoparks of China in 2009 and renamed as the Hong Kong UNESCO Global Geopark in 2015, with the hexagonal rock columns at High Island being the most fascinating and iconic feature. It was believed that the spectacular looking rock at High Island was form around 140 million years ago associated with the eruption of a super-volcano.

A landslide occurred on 21 May 2016 above Sai Wan Road, a country park road and popular hiking trail, and the debris severely damaged the road resulting in closure for more than three months. The nature of the landslide was unusual in that it was a structurally controlled rock slide, with a basal failure surface formed from a persistent, planar sheeting joint within tuff rock with a maximum depth of about 12 m, while the other landslides that occurred in the country park during the same rainstorm involved only shallow failures within soil regolith.

Steven J Williamson is a Technical Director of AECOM Asia Co. Ltd. with over 25 years' experience in the fields of engineering geology and geotechnical engineering. He is a Chartered Engineer and Chartered Geologist and leads a team of professional and technical staff in undertaking a variety of geotechnical works including geohazard and risk assessment both in Hong Kong and overseas.

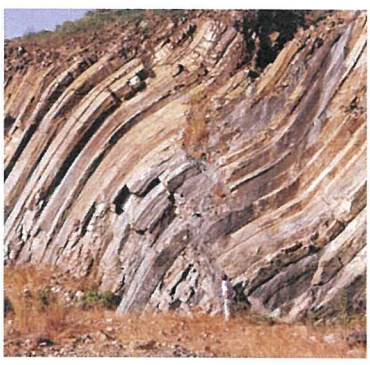

Field trip on 18 November 2017 (Saturday)

Route B: Ling Tao Monastery, Ha Tsuen (Peperite Textures in the Tuen Mun Formation)

Meeting point: **Roadside of Sai Lau Kok Street next to Luk Yeung Galleria and opposite to Tsuen Wan Multi-storey Building (near Tsuen Wan MTR Station Exit B3)**

Gathering Time: **9:30 am**

Trip Leader: **Prof. R J Sewell (Hong Kong Geological Survey)**

This is a half-day trip. Lunch is not included and the group will dismiss at around 12:30pm.

Over the past decades, there have been many debates among geologists in Hong Kong on the occurrence of heterogenetic clasts in the Tuen Mun Formation. There have been controversial ideas put up by different groups of people in the naming and classification of the rocks.

The boulders exposed near Ling Tao Monastery display an interesting geological feature called peperite, formed by the mixing of andesite lava with sediments, including marble clasts and other rock fragments. The contact relationship can be clearly observed, which helps to understand the origin of the Tuen Mun Formation.

Prof. R J Sewell is the Head of the Hong Kong Geological Survey of the Geotechnical Engineering Office of Hong Kong SAR Government. He is an honorary professor of the University of Hong Kong and currently leads a group of professional geologists in updating the geological maps of Hong Kong.

Past Activities

Executive Committee of GSHK (2014-2016)

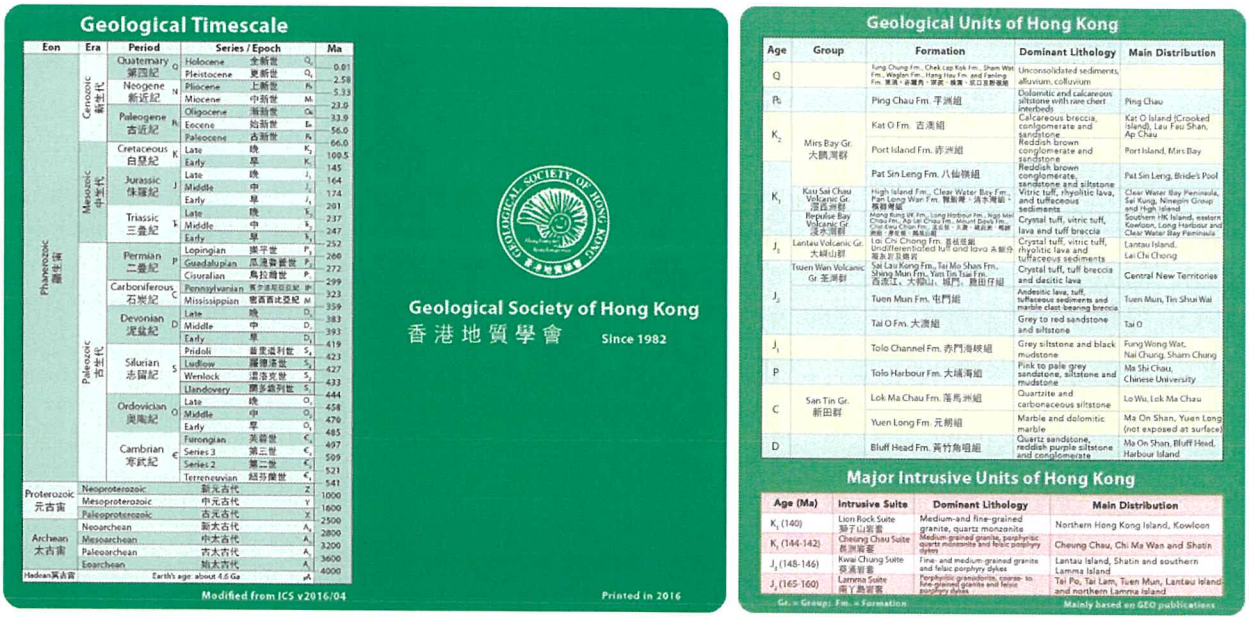

Geological Timescale

Eon	Era	Period	Series / Epoch	Ma
Phanerozoic 顯生宙	Cenozoic 新生代	Quaternary Q 第四紀	Holocene 全新世 Q_1	0.01
			Pleistocene 更新世 Q_2	2.58
		Neogene N 新近紀	Pliocene 上新世 N_2	5.33
			Miocene 中新世 N_1	23.0
		Paleogene Pg 古近紀	Oligocene 漸新世 Pg_3	33.9
			Eocene 始新世 Pg_2	56.0
			Paleocene 古新世 Pg_1	66.0
	Mesozoic 中生代	Cretaceous K 白堊紀	Late 晚 K_2	100.5
			Early 早 K_1	145
		Jurassic J 侏羅紀	Late 晚 J_3	164
			Middle 中 J_2	174
			Early 早 J_1	201
		Triassic Tr 三疊紀	Late 晚 Tr_3	237
			Middle 中 Tr_2	247
			Early 早 Tr_1	252
	Paleozoic 古生代	Permian P 二疊紀	Lopingian 樂平世 P_3	260
			Guadalupian 瓜德魯普世 P_2	272
			Cisuralian 烏拉爾世 P_1	299
		Carboniferous C 石炭紀	Pennsylvanian 賓夕法尼亞紀	323
			Mississippian 密西西比亞紀 M	359
		Devonian D 泥盆紀	Late 晚 D_3	383
			Middle 中 D_2	393
			Early 早 D_1	419
		Silurian S 志留紀	Pridoli 普里道利世 S_4	423
			Ludlow 拉德洛世 S_3	427
			Wenlock 溫洛克世 S_2	433
			Llandovery 蘭多維利世 S_1	444
		Ordovician O 奧陶紀	Late 晚 O_3	458
			Middle 中 O_2	470
			Early 早 O_1	485
		Cambrian € 寒武紀	Furongian 芙蓉世 $€_3$	497
			Series 3 第三世 $€_2$	509
			Series 2 第二世 $€_1$	521
			Terreneuvian 纽芬蘭世 $€_1$	541
Proterozoic 元古宙	Neoproterozoic 新元古代			Z 1000
	Mesoproterozoic 中元古代			Y 1600
	Paleoproterozoic 古元古代			X 2500
Archean 太古宙	Neoarchean 新太古代			A_4 2800
	Mesoarchean 中太古代			A_3 3200
	Paleoarchean 古太古代			A_2 3600
	Eoarchean 始太古代			A_1 4000
Hadean 冥古宙	Earth's age: about 4.6 Ga			A_0

Modified from ICS v2016/04

Geological Society of Hong Kong
香港地質學會 Since 1982

Printed in 2016

Geological Units of Hong Kong

Age	Group	Formation	Dominant Lithology	Main Distribution
Q		Tung Chung Fm., Chek Lap Kok Fm., Sham Wat Fm., Wanglan Fm., Hang Hau Fm. and Fanling Fm. 東涌、赤鱲角、深浮、橫瀾、坑口及粉嶺組	Unconsolidated sediments, alluvium, colluvium	
P_t		Ping Chau Fm. 平洲組	Dolomitic and calcareous siltstone with rare chert interbeds	Ping Chau
K_2	Mirs Bay Gr. 大鵬灣群	Kat O Fm. 吉澳組	Calcareous breccia, conglomerate and sandstone	Kat O Island (Crooked Island), Lau Fau Shan, Ap Chau
		Port Island Fm. 赤洲組	Reddish brown conglomerate and sandstone	Port Island, Mirs Bay
		Pat Sin Leng Fm. 八仙嶺組	Reddish brown conglomerate, sandstone and siltstone	Pat Sin Leng, Bride's Pool
K_1	Kau Sai Chau Volcanic Gr. 滘西洲群	High Island Fm., Clear Water Bay Fm., Pan Long Wan Fm. 赤柱牌、清水灣組、鴛鴦灣組	Vitric tuff, rhyolitic lava, and tuffaceous sediments	Clear Water Bay Peninsula, Sai Kung, Ninepin Group and High Island
	Repulse Bay Volcanic Gr. 淺水灣群	Mang Kung Uk Fm., Long Harbour Fm., Ngau Mei Chau Fm., Kau Lau Chau Fm., Mount Davis Fm., Chai Wan Chau Fm. 蒙公屋、大灣、牛尾洲、摩星嶺、柴灣、赤柱角、鴨脷洲組	Crystal tuff, vitric tuff, lava and tuff breccia	Southern HK Island, eastern Kowloon, Long Harbour and Clear Water Bay Peninsula
J_3	Lantau Volcanic Gr. 大嶼山群	Lai Chi Chong Fm. 荔枝莊組 Undifferentiated tuff and lava 未細分凝灰岩及熔岩	Crystal tuff, vitric tuff, rhyolitic lava and tuffaceous sediments	Lantau Island, Lai Chi Chong
J_2	Tuen Wan Volcanic Gr. 荃灣群	Sai Lau Kong Fm., Tai Mo Shan Fm., Shing Mun Fm., Yan Tin Tsai Fm. 西貢江、大帽山、城門、鹽田仔組	Crystal tuff, tuff breccia and dacitic lava	Central New Territories
		Tuen Mun Fm. 屯門組	Andesitic lava, tuff, tuffaceous sediments and marble clast-bearing breccia	Tuen Mun, Tin Shui Wai
		Tai O Fm. 大澳組	Grey to red sandstone and siltstone	Tai O
J_1		Tolo Channel Fm. 赤門海峽組	Grey siltstone and black mudstone	Fung Wong Wat, Nai Chung, Sham Chung
P		Tolo Harbour Fm. 大埔海組	Pink to pale grey sandstone, siltstone and mudstone	Ma Shi Chau, Chinese University
C	San Tin Gr. 新田群	Lok Ma Chau Fm. 落馬洲組	Quartzite and carbonaceous siltstone	Lo Wu, Lok Ma Chau
		Yuen Long Fm. 元朗組	Marble and dolomitic marble	Ma On Shan, Yuen Long (not exposed at surface)
D		Bluff Head Fm. 黃竹角咀組	Quartz sandstone, reddish purple siltstone and conglomerate	Ma On Shan, Bluff Head, Harbour Island

Major Intrusive Units of Hong Kong

Age (Ma)	Intrusive Suite	Dominant Lithology	Main Distribution
K_2 (140)	Lion Rock Suite 獅子山岩套	Medium- and fine-grained granite, quartz monzonite	Northern Hong Kong Island, Kowloon
K_2 (144-142)	Cheung Chau Suite 長洲岩套	Medium-grained granite, porphyritic quartz monzonite and felsic porphyry dykes	Cheung Chau, Chi Ma Wan and Shatin
J_3 (148-146)	Kwai Chung Suite 葵涌岩套	Fine- and medium-grained granite and felsic porphyry dykes	Lantau Island, Shatin and southern Lamma Island
J_3 (165-160)	Lamma Suite 南丫島岩套	Porphyritic granodiorite, coarse- to fine-grained granite and felsic porphyry dykes	Tai Po, Tai Lam, Tuen Mun, Lantau Island and northern Lamma Island

Gr. = Group; Fm. = Formation

Mainly based on GEO publications

The Updated Geological Timescale Card (2016)

Past Activities

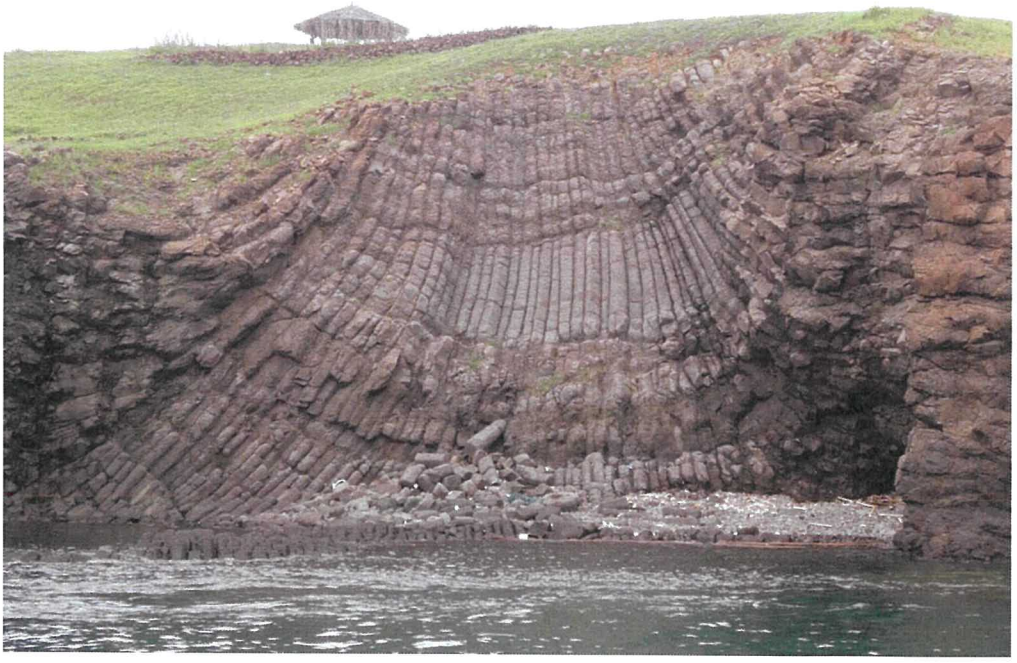

Field Trip to Penghu, Taiwan (2014)

Past Activities

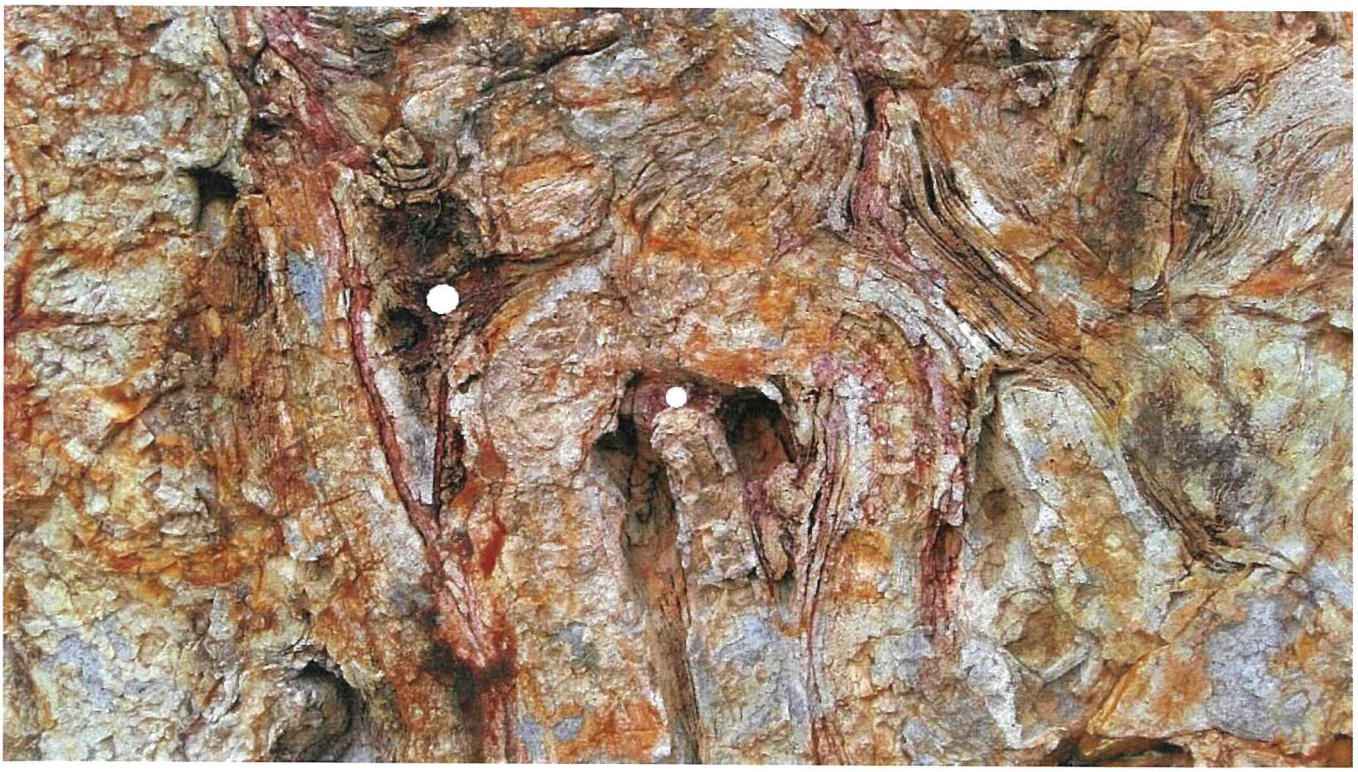

Field Trip to Tai Long Sai Wan (2015)

Past Activities

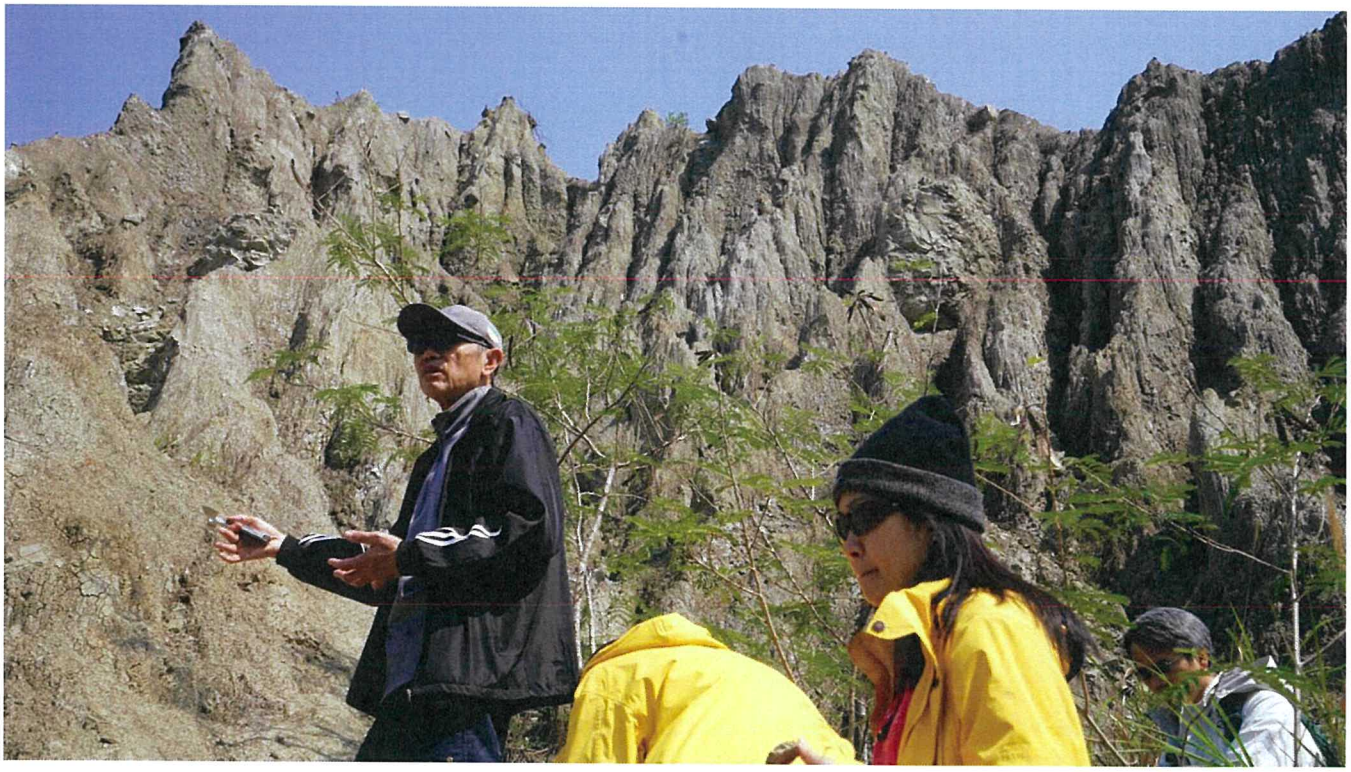

Field Trip to Southern and Eastern Taiwan (2016)

Past Activities

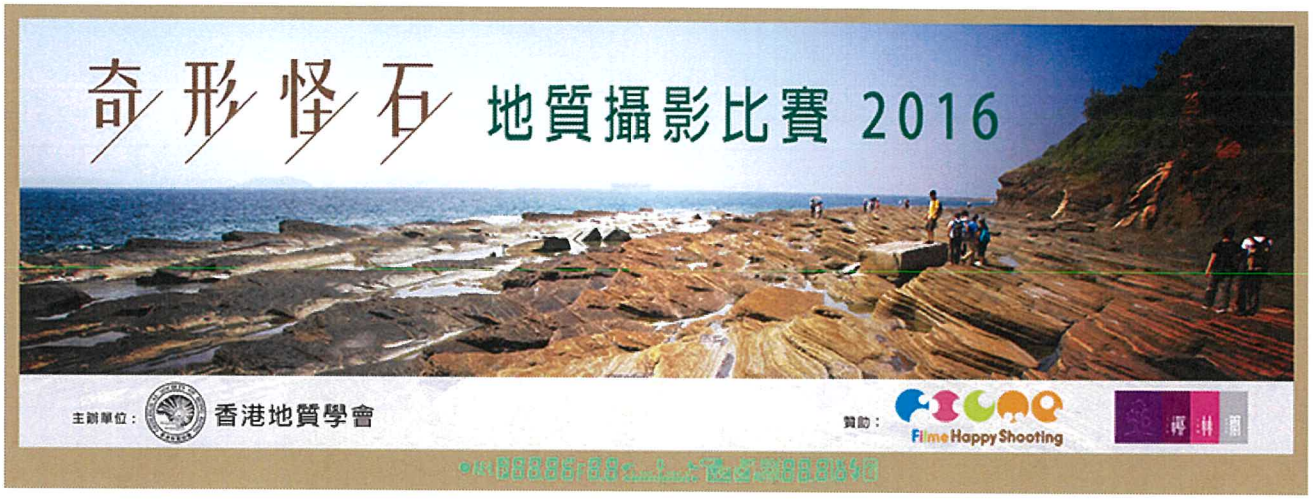

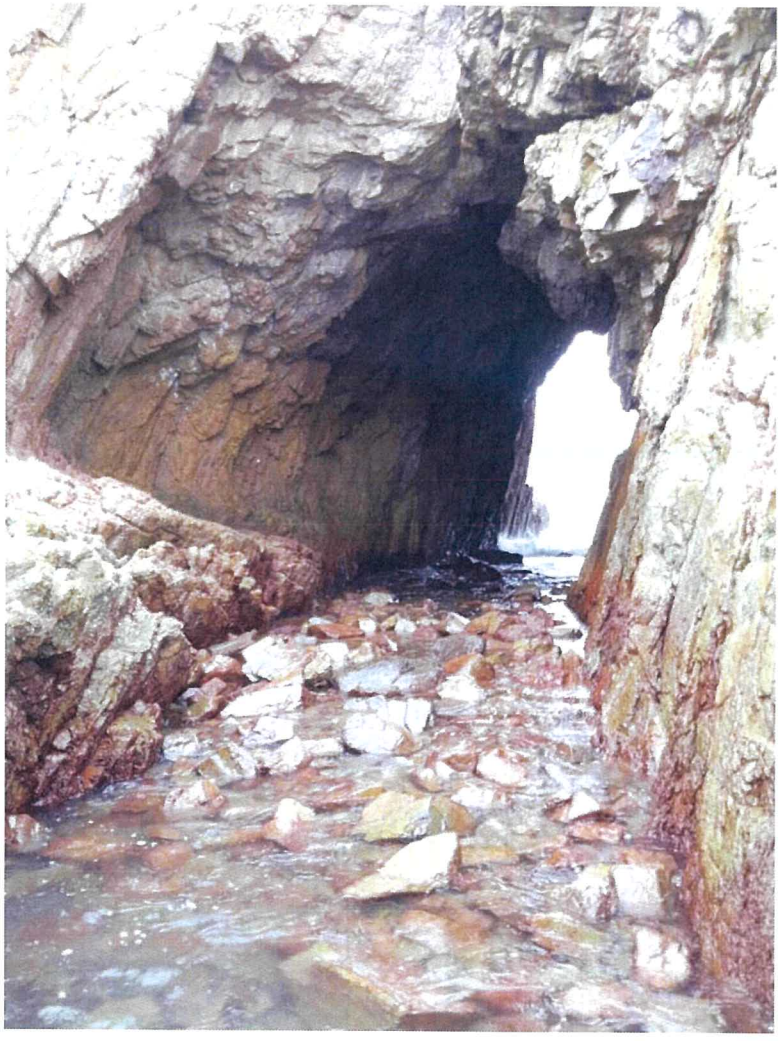

Photo Competition (2016)

Past Activities

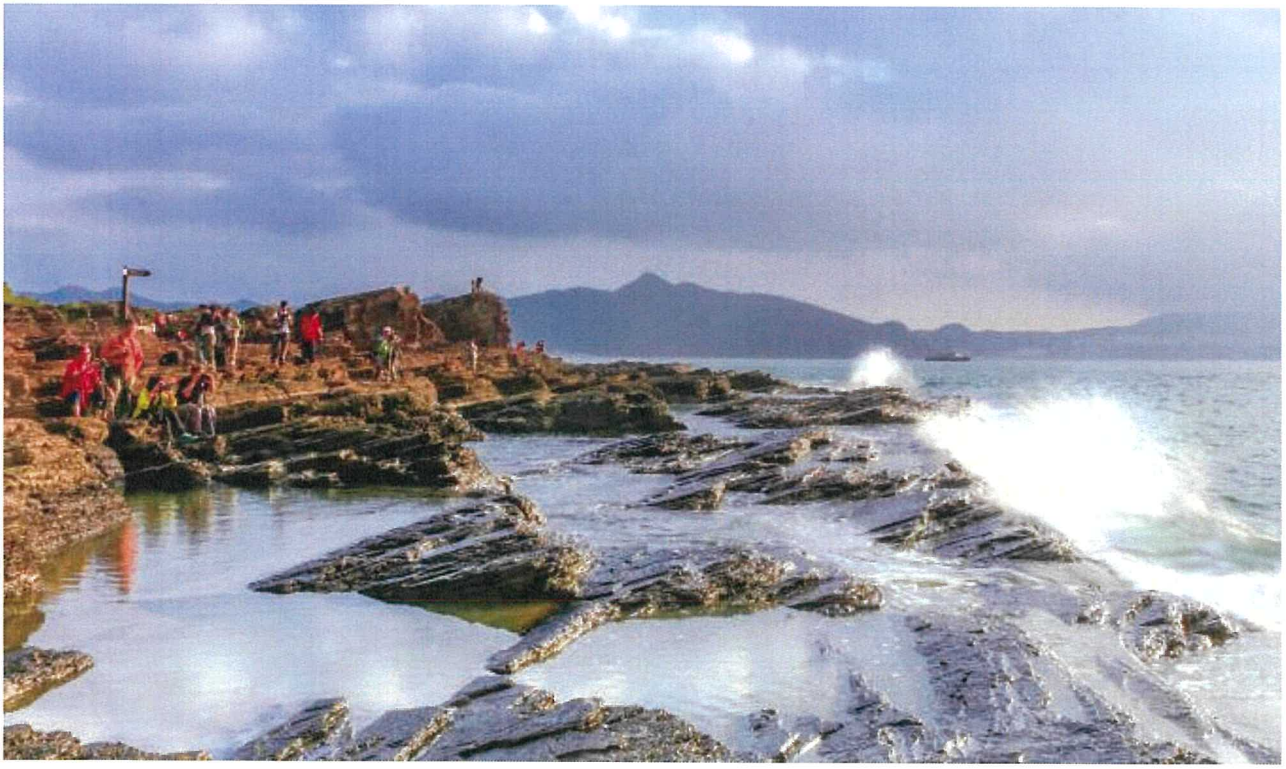

Photo Competition (2016)

Past Activities

School Talk (2016)

Booth Promotion at Ma On Shan Colour Mart (2016)

Past Activities

Site Visit to Tuen Mun - Chek Lap Kok Link (2017)

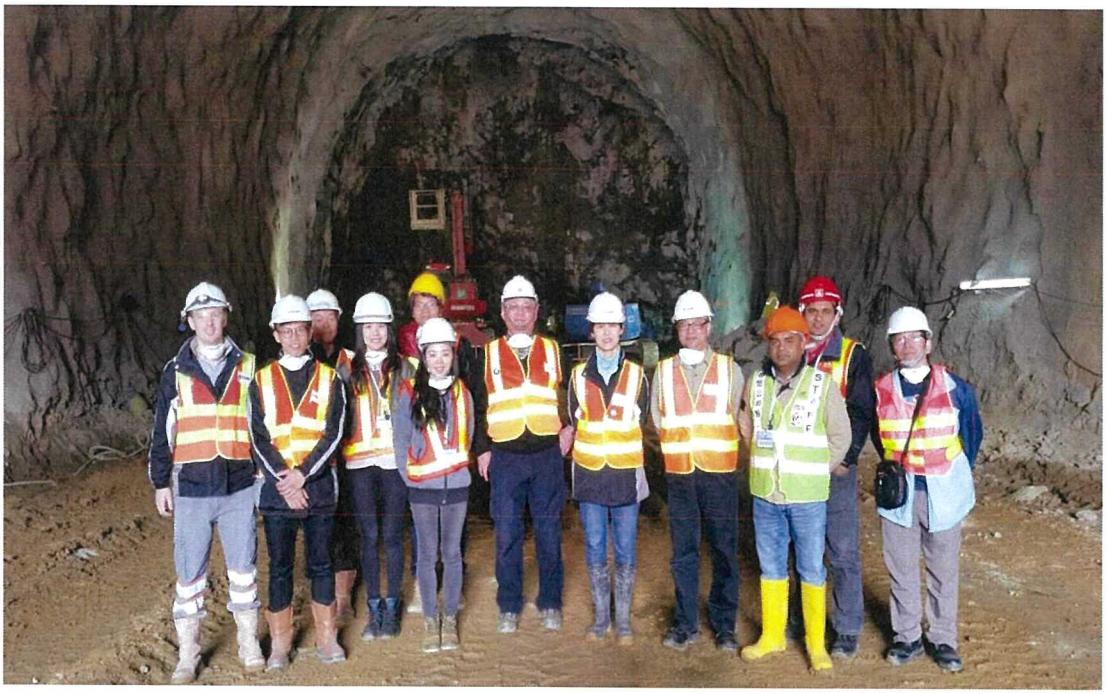

Site Visit to Liang Tong (2017)

Past Activities

Talk on Paleotonology (2017)

Field Trip to Po Toi Island (2017)

Past Activities

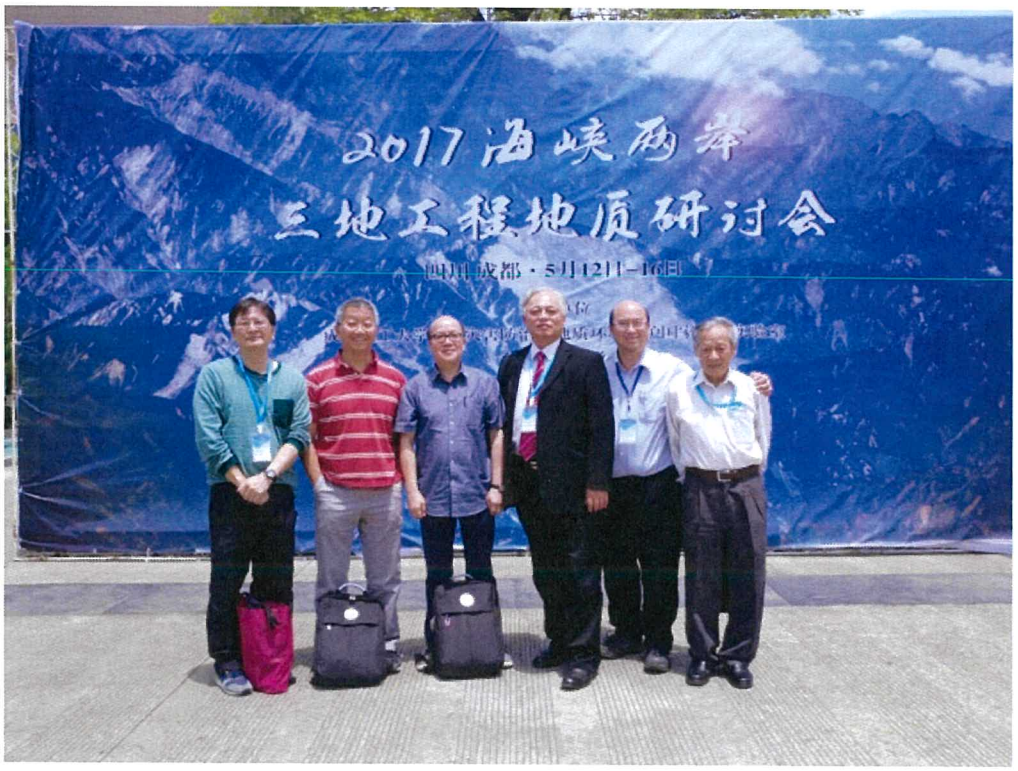

Engineering Geology Conference at Chengdu (2017)

Sponsor (Platinum)

Concentric
協力建業

Concentric Construction Company Limited

Sponsor (Gold)

香 港 建 造 商 會
Hong Kong Construction Association

Site Investigation Contractors Committee

Hong Kong Construction Association
Site Investigation Contractors Committee

Sponsor (Gold)

AECOM Asia Limited

CM Wong & Associated Limited

Sponsor (Gold)

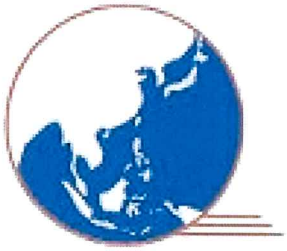

歐美大地
EARTH PRODUCTS CHINA LTD

Earth Products China Limited

兆基鑽探工程有限公司
SK Drilling & Engineering Co., Ltd.

SK Drilling & Engineering Company Limited

Sponsor (Gold)

Fugro Geotechnical Services Limited

Pinnacle Capital Limited

Sponsor (Gold)

BLISSFUL
Global Investment Limited
We invest in Health & Wealth

Blissful Global Investment Limited

KEG

Kaisun Energy Group

Sponsor (Silver)

Yee Hop Engineering Company Limited

Datgel Asia Pte Ltd (Reseller of gINT)

義合工程有限公司
YEE HOP ENGINEERING CO., LTD.

Buildings Department:-

**Registered General Building Contractor*

**Registered Specialist Contractor (Foundation)*

Development Bureau:-

**Specialist Contractor – Land Piling (Group II)*

**Roads & Drainage (Group CP)*

**Port Works (Group B)*

**Waterworks (Group BP)*

**Site Formation (Group BP)*

AECOM Imagine it. Delivered.

Reducing Geotechnical Risk

Through insightful geological analysis

AECOM has the largest geotechnical consulting practice in Asia and in Hong Kong alone has a team of over 300 dedicated engineers and geoscience professionals with specialization in tunnels, caverns, highways, bridges, slope engineering and geo-hazard assessment. In addition to this we are able to draw on a talent pool of over 90,000 professionals worldwide in all major areas of the built and natural environment. With this breadth and depth of experience, we are able to synthesize data, construct robust geological models and derive insightful solutions to complex ground problems, reducing uncertainty and risk in some of Asia's most challenging infrastructure projects.

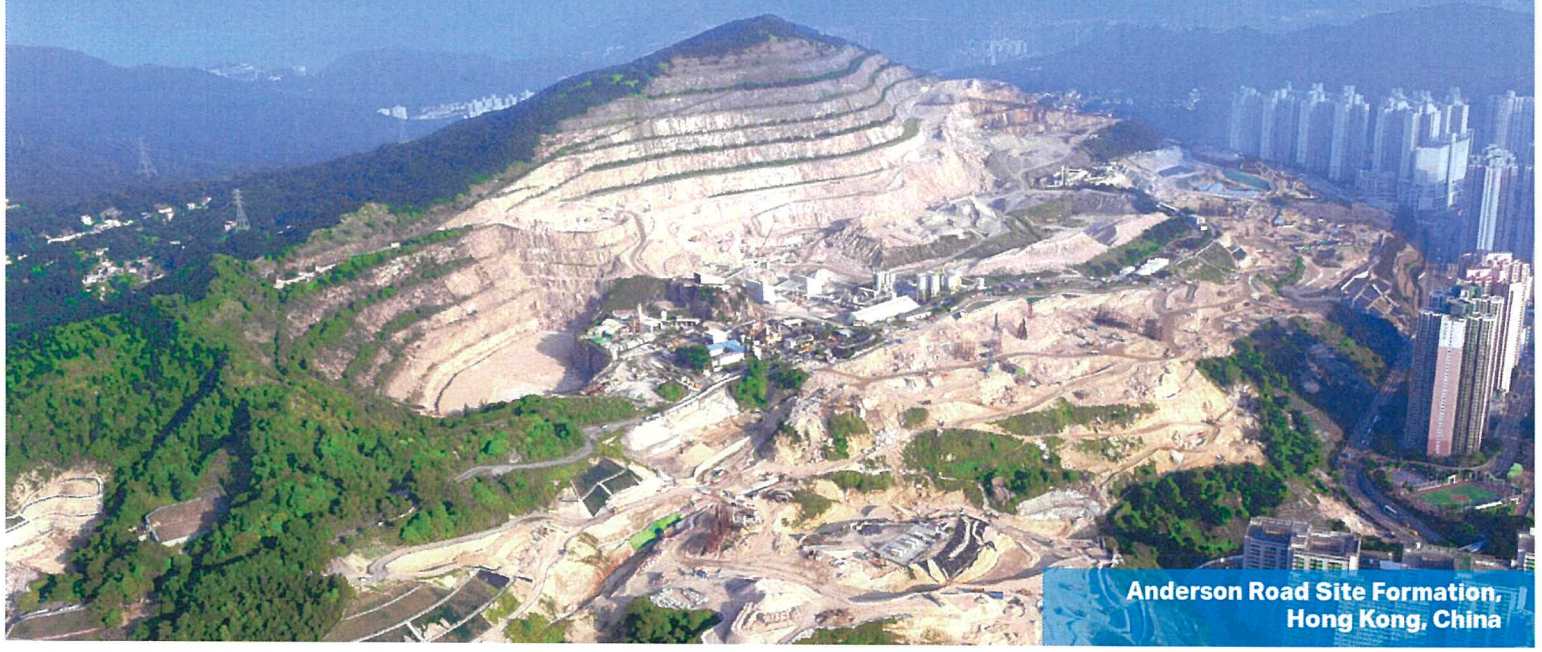

Anderson Road Site Formation, Hong Kong, China

SCL1128, Hong Kong, China

XRL822, Hong Kong, China

Mid-Level, Hong Kong, China

Shatin Pass Road, Hong Kong, China

Sai Wan Road, Hong Kong, China

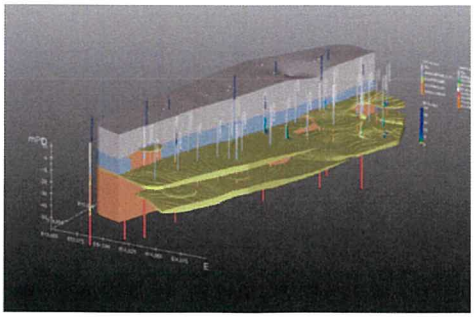

3D Geological Models